

**Stable Hydrogenated Amorphous Silicon  
Germanium for Photovoltaic Applications.  
Experimental and Computational Studies.**



# **Stable Hydrogenated Amorphous Silicon Germanium for Photovoltaic Applications. Experimental and Computational Studies.**

**Stabiel gehydrogeneerd amorf silicium-germanium voor  
fotovoltaïsche toepassingen. Experimenteel en computationeel  
onderzoek.**

(met een samenvatting in het Nederlands)

## **PROEFSCHRIFT**

TER VERKRIJGING VAN DE GRAAD VAN DOCTOR  
AAN DE UNIVERSITEIT UTRECHT OP GEZAG VAN  
DE RECTOR MAGNIFICUS, PROF. DR. W. H. GISPEN,  
INGEVOLGE HET BESLUIT VAN HET COLLEGE VOOR  
PROMOTIES IN HET OPENBAAR TE VERDEDIGEN OP  
WOENSDAG 8 OCTOBER 2003 DES MIDDAGS TE 12.45 UUR

door

**Raúl Jiménez Zambrano**

geboren op 25 april 1973, te Madrid (Spanje)

PROMOTOR: PROF. DR. R. E. I. SCHROPP

Faculteit Natuur - en Sterrenkunde  
Universiteit Utrecht

CO - PROMOTOR: DR. J. K. RATH

Faculteit Natuur - en Sterrenkunde  
Universiteit Utrecht

The work described in this thesis was made possible by financial support from the  
"Netherlands Agency for Energy and the Environment" (NOVEM).

Druk: Printpartners Ipskamp, Enschede

ISBN 90-393-3481-1

# Contents

---

<b>1</b>	<b>Introduction</b>	<b>9</b>
1.1	Renewable energies. Solar energy . . . . .	9
1.2	Hydrogenated amorphous silicon . . . . .	10
1.2.1	Material properties . . . . .	10
1.2.2	Alloys . . . . .	12
1.3	Solar cells . . . . .	12
1.4	Aim and outline of this thesis . . . . .	13
<b>2</b>	<b>Experimental techniques</b>	<b>15</b>
2.1	Plasma enhanced chemical vapour deposition (PECVD) . . . . .	15
2.2	Characterization techniques . . . . .	16
2.2.1	Material characterization . . . . .	16
2.2.2	Solar cell characterization . . . . .	21
2.3	Degradation . . . . .	24
<b>3</b>	<b>Deposition of <i>a</i>-SiGe:H at low temperatures and high deposition rate</b>	<b>27</b>
3.1	Introduction . . . . .	27
3.2	Growth of <i>a</i> -Si:H by PECVD . . . . .	28
3.3	Growth of <i>a</i> -SiGe:H by PECVD . . . . .	31
3.3.1	Hydrogen dilution of <i>a</i> -SiGe:H . . . . .	34
3.3.2	Low substrate temperature deposition of <i>a</i> -SiGe:H . . . . .	36
3.3.3	Deposition of <i>a</i> -SiGe:H with Si <sub>2</sub> H <sub>6</sub> +GeH <sub>4</sub> . . . . .	37
3.4	Results in deposition of <i>a</i> -SiGe:H at low temperature . . . . .	38
3.4.1	Material properties . . . . .	38
3.4.2	Discussion . . . . .	50
3.5	Results in deposition of <i>a</i> -SiGe:H at high deposition rates . . . . .	56
3.6	Conclusions . . . . .	58
<b>4</b>	<b>Computer-aided solar cell improvement</b>	<b>61</b>
4.1	Introduction . . . . .	61
4.2	Modelling. D-AMPS computer simulation program . . . . .	61
4.2.1	AMPS computer code . . . . .	61
4.2.2	Set of device models implemented in D-AMPS . . . . .	62

4.2.3	Sensitivity study of solar cells parameters for D-AMPS simulation program . . . . .	64
4.3	Results . . . . .	66
4.3.1	Defect Pool Model versus Uniform Defect Model for fitting purposes . . . . .	68
4.3.2	Computer Predictions using the UDM and the DPM models	73
4.3.3	Influence of the band gap profile studied by computer simulation . . . . .	77
4.3.4	From computer prediction to experimental observations .	85
4.4	Conclusions . . . . .	91
<b>5</b>	<b>Stability of <i>a</i>-SiGe:H as material, single junction and tandem solar cells</b>	<b>95</b>
5.1	Introduction . . . . .	95
5.2	Microscopic origin of the Staebler-Wronski effect . . . . .	95
5.3	Photodegradation techniques . . . . .	99
5.3.1	Samples . . . . .	99
5.3.2	Light soaking conditions . . . . .	100
5.4	Stability of <i>a</i> -SiGe:H as material . . . . .	100
5.4.1	Introduction . . . . .	100
5.4.2	Experimental details . . . . .	103
5.4.3	Results and discussion . . . . .	103
5.5	Stability of <i>a</i> -SiGe:H in single junction solar cell structure . . . .	106
5.5.1	Introduction . . . . .	106
5.5.2	Experimental details . . . . .	108
5.5.3	Results and discussion . . . . .	108
5.6	Stability of <i>a</i> -SiGe:H in a tandem solar cell structure . . . . .	117
5.6.1	Introduction . . . . .	117
5.6.2	Experimental details . . . . .	117
5.6.3	Results and discussion . . . . .	118
5.7	Conclusions . . . . .	119
	<b>References</b>	<b>123</b>
	<b>Summary</b>	<b>133</b>
	<b>Samenvatting</b>	<b>137</b>
	<b>List of publications</b>	<b>141</b>
	<b>Acknowledgements</b>	<b>143</b>

*Contents* 7

---

**Curriculum vitae** **145**



# 1 Introduction

---

## 1.1 Renewable energies. Solar energy

In the last 5 years the energy consumption has increased by more than 15% in the European Community, most of which is generated from coal and natural gas. In Asia is expected an annual increase in 4 % until 2020. Meanwhile, more than 20 of the conflicts in the world today are directly related with areas containing oil and/or natural gas (all in "developing" countries). In "developed" countries the tangle of laws entails privileged position misuse with negative results over the citizens (an extra  $7 \times 10^4$  millions of dollars fallen on the taxpayer during the "10 days energetic crisis" in California in 2001). Renewable energies together with appropriate energy politics are the alternative to conventional energy resources and the solution to many of the previous issues and environmental concerns.

Among the renewable energies, the photovoltaic solar energy is the less used. Several reasons can be found in the cost (production, installation and storing system), the limited energy conversion efficiency and the operating life time. At present, silicon technology dominates the market with crystalline silicon solar cells, technology on which we will concentrate. Though they are more expensive and they absorb light less efficiently than amorphous silicon solar cells, they currently have the advantage of higher energy conversion efficiencies and they are not sensitive to degradation due to light exposure. Nevertheless, amorphous silicon has natural characteristics to be an attractive material to coexist with or to replace crystalline silicon. Among others, the high absorption coefficient, low process temperature, easy doping and alloying or abundance of silicon and hydrogen can be pointed out.

The main problem of amorphous silicon is the degradation when exposed to light. This is known as the Staebler-Wronski effect. The physical characteristics of the material deteriorate 10 to 20 % with respect to the initial values. The major developments against degradation have been the multijunction solar cells and the use of hydrogen dilution during the growth of the amorphous silicon. Multijunction structures are formed by several solar cells stacked one over the other. Each of them absorbing a broad band of the solar spectrum, which is achieved by alloying the amorphous silicon. The study of amorphous silicon alloys contribute to higher efficiency solar cells as well as to a better understanding of the material with no alloying.

## 1.2 Hydrogenated amorphous silicon

The following brief sections give a survey of the properties of hydrogenated amorphous silicon, *a*-Si:H, material. For a more detail review, see Ref. [1,2].

### 1.2.1 Material properties

#### Atomic structure

The atomic structure of *a*-Si:H materials can be described as a continuous random network where most of the atoms are fourfold-coordinated. This network exhibits short-range order, i.e. the structural order of the network is not maintained further than the second-nearest-neighbour distance. By comparison, in crystalline silicon, the atoms are arranged into a regular, periodic structure. The disorder in *a*-Si:H introduces a high amount of defects in the network, such as bond length and angle deviation, non-coordinated bonds or voids. Although hydrogen dilution of the feed gasses during the deposition of *a*-Si:H reduces the defect density by several orders of magnitude, the presence of imperfections can not be avoided completely. Additional H-related imperfections are formed (isolated Si-H bonds, interstitial H<sub>2</sub> or microvoids), which may determine the structural and electrical properties of the *a*-Si:H material. However, the hydrogen plays a role in the modification of band gap, decreasing the structural disorder and promoting the formation of crystals within the amorphous network (microcrystalline silicon, *μc*-Si:H). It is also believed that H acts as a precursor for the degradation process in *a*-Si:H (Staebler-Wronski effect [3]).

#### Electronic properties

Crystalline silicon and *a*-Si:H have a similar short-range order electronic density of state (DOS). The long-range disorder causes the localization of states at the valence and the conduction band edge (see Fig. 1.1). The states with an exponential decay from the valence (conduction) band towards the band gap are known as band tail states. The transport properties are controlled by the DOS distribution in the band gap and by the carrier mobility. For example, when the density of defect states in the middle of the band gap is very high ( $> 10^{18} \text{cm}^{-3}$ ), the conduction process is dominated by tunneling at the states near the Fermi level (middle of the band gap). Due to the low defect density in device-quality *a*-Si:H, the contribution of this kind of transport is not significant (except at very low temperatures). Instead, the transport takes place predominately in the extended states of the valence (for holes) and of the conduction band (for electrons). The transition energy

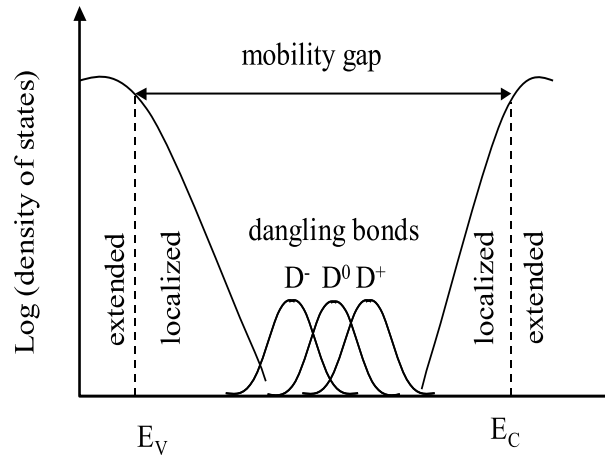


**Figure 1.1:** Schematic diagram of the density of states distribution in intrinsic *a*-Si:H.  $E_V$  and  $E_C$  denotes the valence and conduction band edge, respectively.

between the localised and the delocalised states defines the mobility gap.

A third kind of defects is found deeper in the band gap. They are non-coordinated bonds, also called dangling bonds. The dangling bonds can be neutral ( $D^0$ ) or positively ( $D^+$ ) or negatively charged ( $D^-$ ). The state  $D^-$  is doubly occupied by electrons while the state  $D^+$  is an empty state. The position of these defect states in the band gap depends on their energy,  $D^+$  being close to the conduction band,  $D^0$  being near the mid gap and  $D^-$  being close to the valence band.

### Optical properties

Two kinds of optical transitions can be defined during the absorption process, namely a "direct" and an "indirect" transition. The direct transition is a first order process involving only the absorbed photon. In this case the energy is conserved and the wave number does not change. The indirect transition is a second order process simultaneously involving the absorbed photon and a phonon. The energy and wave number are conserved. Crystalline silicon is an example of material with absorption through indirect transitions.

The *a*-Si:H disorder network leads to a non-periodic lattice potential. As a result, the inelastic scattering of electrons occurs after a mean free path of 10-15 Å, strongly decreasing the carrier mobility. Under these circumstances the

wave number is not conserved and the optical transitions in *a*-Si:H can be considered as direct.

The combination of occupied states in the valence band and empty states in the conduction band determines the dependence of the absorption coefficient,  $\alpha$ , on the photon energy. The photon energies in the visible range of the spectrum are then absorbed by direct transition, resulting in a higher absorption of *a*-Si:H over crystalline Si. As a direct consequence, *a*-Si:H films with thicknesses one order of magnitude lower than crystalline material absorb the same amount of light.

An important parameter in relation to the absorption is the optical band gap,  $E_g$ . Different methods have been proposed to describe this parameter. The most widely used definition of optical gap is as proposed by Tauc [4]. Tauc proposed a quadratic energy relation between the optical band gap and the absorption coefficient. Although its relation with the mobility gap has not yet been established, the optical gap is often referred as a measure of the band gap.

The excitation of carriers from the valence band tail states to the conduction band states determines an exponential dependence of  $\alpha$  on the photon energy ( $\alpha \propto \exp[-h\nu/E_U]$ ), clearly observable for energies below  $E_g$ . This exponential region, known as Urbach tail, is characterised by the Urbach energy,  $E_U$ . The characteristic energy of the conduction band tail ( $\leq 30$  meV) is normally much smaller than that of the valence band tail (45-55 meV). Therefore the Urbach energy reflects the valence band tail.

### 1.2.2 Alloys

Amorphous silicon is easy to alloy, which gives a direct control over the band gap. For instance, adding Ge or C during the deposition of *a*-Si:H allows one to tune the band gap between 1 eV and 2.5 eV. Although they do not currently show as high quality properties as the pure *a*-Si:H, the *a*-Si:H alloys are widely used for industrial applications. The lower alloy properties are caused by an increase in deep defects, which acts as recombination centers. At the same time, the order in the network is negatively affected, creating additional carrier scattering (reducing the carrier mobility). The characteristics of Ge alloying will be the aim of this study.

## 1.3 Solar cells

The use of *a*-Si:H material for applications in solar cells presents several advantages with respect to other semiconductors. Some of these advantages have been mentioned before: the high optical absorption coefficient in the visible spectra

range or the easy alloying. On the other hand, the high defect density in doped  $a$ -Si:H prevents the creation of solar cells with thick doped layers in a p-n structure, as it is typical in crystalline solar cells where the carriers are photogenerated in the doped layers and diffuse to the contacts. In  $a$ -Si:H solar cells the light is absorbed in an intrinsic layer (undoped), with better carrier mobilities than the doped  $a$ -Si:H material, but not high enough to extract the carriers by diffusion. The carriers recombine before they can diffuse to the contacts. They must be extracted by creating an electric field inside the intrinsic layer. This is achieved with two thin doped  $a$ -Si:H layers each one on one side of the intrinsic layer. The doped layers are thin enough to prevent undesired absorption and recombination losses. The difference of potential created by the doped layers in the intrinsic layer inversely depends on the defect density and the thickness of the intrinsic layer. On the other hand, the absorption of light and carrier generation increases with the thickness of the intrinsic layer. From these competing factors the optical intrinsic layer thickness is obtained between 200-800 nm.

The most severe limitation of  $a$ -Si:H single junction solar cells is the degradation during light exposure (Staebler-Wronski effect [3]). On the other hand, the main losses in a single junctions are by thermalization of photogenerated carriers with photon energies higher than  $E_g$  and from transparenting of solar cells to photons with energies lower than  $E_g$ . By stacking several cells one over the other the absorption of the total structure increases. This permits one to reduce the thickness of each of them, limiting the light-induced degradation. The resulting stacked structure is known as a multijunction structure. If the band gap of the intrinsic layer of each component cell of the multijunction cell is also varied to match several broad bands of the solar spectrum, the losses previously described are reduced. Thus, multijunction solar cells can show higher stability and efficiency than single junctions.

In  $a$ -SiGe:H materials the defect density is higher than in unalloyed  $a$ -Si:H, while the absorption increases with the Ge content. Although the necessity of a thinner layer would be deduced from the previous argument, this is not enough to collect the photogenerated carriers. The offset in band gaps between the intrinsic layer ( $\sim 1.5$  eV) and the doped layers ( $\sim 1.8$  eV) acts as a barrier against back-diffusion but at the same time hinders the collection of the photogenerated carriers. The offset limitations can be overcome with a correct design of the band gap.

## 1.4 Aim and outline of this thesis

The research was aimed at the study of low band gap  $a$ -SiGe:H material with special emphasis in developing a material with high stability against light-induced

degradation. Of particular interest is the growth of protocrystalline *a*-SiGe:H which is obtained by depositing near the threshold of microcrystalline formation. This kind of material contributes to the improvement of the medium range order. Technologically friendly deposition conditions for stable *a*-SiGe:H material were investigated. The scope of the research encompasses the experimental application of the *a*-SiGe:H material in single and tandem solar cells to numerical simulations of these structures. The detailed understanding of the single junction *a*-SiGe:H solar cell behaviour under dark and illumination conditions by computer modelling in this research opened new chances for enhancing *a*-SiGe:H solar cells output. Endeavours to understand the conduct of *a*-SiGe:H solar cells during degradation experiments were carried out by computer simulation.

The thesis is composed of six chapters.

- Chapter 2 provides a general description of the deposition technique and conditions. The setups used for material and solar cell characterization are described.
- Chapter 3 gives a detail description of the deposition processes by rf PECVD. Different deposition conditions to grow *a*-SiGe:H are described and experimentally carried out. The experimental results are given and discussed.
- Chapter 4 presents a computer-aided study of *a*-SiGe:H single junction solar cells. A study of the influence of the band gap grading on the solar cell performance is given. Predictions for the improvement of the solar cell output are presented.
- Chapter 5 deals with the light-induced degradation experiments carried out on materials, single and tandem solar cells. The high stability against light soaking of *a*-SiGe:H is compared with different *a*-Si:H solar cell structures.

## 2 Experimental techniques

---

### 2.1 Plasma enhanced chemical vapour deposition (PECVD)

One of the widely used technique to deposit  $a$ -Si:H is by plasma decomposition of silane. Other gasses can be added to dope or to alloy the material or to dilute the plasma species. A field in the plasma can be created by direct current (DC), radio frequency (rf) or microwave frequency. The electrons gain their energy from this electric field. Dissociation of the gas molecules takes place through inelastic collision processes with energetic electrons. Thus, the plasma favours the gas phase dissociation reactions. The substrate temperature can be controlled independently from the plasma parameters. This enables one to reach lower substrate temperatures than with other techniques (thermal CVD), which is suitable for retaining hydrogen in the material.

The samples described along this study were deposited by rf-PECVD in the multi-chamber high vacuum deposition system PASTA (Process equipment for Amorphous Silicon Thin-film Application) [5,6]. The system consists of five independent deposition chambers interconnected through a load lock and by a transport system. In chambers 1 to 3, p-type, intrinsic and n-type PECVD layers are deposited, respectively. In chambers 4 and 5 the hot-wire CVD technique for deposition of intrinsic material is used. The maximum substrate side is 4"×4". The background pressure in all the chambers is  $\sim 10^{-8}$  mbar.

Typical deposition conditions used for  $a$ -SiGe:H material are listed in Table 2.1. For material characterization Corning glass and polished p-type crystalline wafer ( $\langle 100 \rangle$  orientation) were used as substrates. The solar cells were deposited on transparent conducting oxide (TCO) coated glass (Asahi U-type SnO<sub>2</sub>:F).

**Table 2.1:** Typical deposition conditions for *a*-SiGe:H.

Deposition parameter	Source gasses	
	SiH <sub>4</sub> +GeH <sub>4</sub>	Si <sub>2</sub> H <sub>6</sub> +GeH <sub>4</sub>
Substrate temperature (°C)	170-200	170-220
Hydrogen dilution ratio ( <i>f</i> ) (H <sub>2</sub> /Source gasses)	60-80	80-150
rf power density (mW/cm <sup>2</sup> )	40	40
Deposition pressure (mbar)	2.2	2.2

## 2.2 Characterization techniques

### 2.2.1 Material characterization

#### Reflection-Transmission (RT)

The analysis of the spectral reflectance and transmittance in the wavelength range 420-1035 nm (3-1.2 eV) determines the optical parameters and the thickness of the film. The light beam enters the film side of the glass/film structure. The solution of the Fresnel equations for the reflectance and the transmittance of the light beam in this structure as a function of the photon energy,  $h\nu$ , defines the refractive index,  $n(h\nu)$ , and the extinction coefficient,  $k(h\nu)$ . The absorption coefficient,  $\alpha$ , is determined from  $k$  as  $4\pi h\nu k/hc$ , where  $h$  is the Planck constant and  $c$  is the speed of light. Another interesting parameter is the value of  $n$  at low energies,  $n_0$ , which can be related to the density of the material. The value of  $n_0$  is determined by extrapolating  $1/(n(h\nu)^2-1)$  to  $h\nu=0$  [7].

The optical band gap,  $E_g$ , can be found from the dependence of  $\alpha$  on  $h\nu$  for the photon energy region where the density of states distribution is significant. Equation 2.1 holds in this region.

$$\alpha n h\nu = a(h\nu - E_g)^{p+q+1} \quad (2.1)$$

In this equation  $a$  is a constant and the parameters  $p$  and  $q$  are related with the shape of the band edges. Since Tauc [4] reported a linear relation between  $(\alpha n E)^{1/2}$  and the photon energy, the most usual value for  $p$  and  $q$  is 1/2, corresponding to a parabolic shape of the band edges. The band gap obtained solving Equation 2.1 with these values is called the Tauc's band gap,  $E_{Tauc}$ . Several authors [8,9] have reported that a linear shape of the band edges has better linearity than a parabolic shape of the band edges. The value for  $p$  and  $q$  would be then equal to 1 and in this case the band gap obtained solving Equation 2.1 is called the

cubic band gap. An alternative method to define the optical band gap is the energy ( $E_x$ ) at which  $\alpha(E_x)$  reaches a certain value,  $10^x$ . The band gap  $E_{3.5}$  and  $E_{0.4}$  are normally given for  $\alpha=10^{3.5} \text{ cm}^{-1}$  and  $\alpha=10^4 \text{ cm}^{-1}$ , respectively. The band gap  $E_{0.4}$  shows values  $\sim 0.2$  eV higher than the Tauc band gap. This last convention has the advantage of being independent of the shape of the band edges. But for thick layers with pronounced fringes, the last method reduces its accuracy [10].

In this study, the band gap of the thin films ( $\sim 100$  nm) is defined as  $E_{3.5}$  for accuracy reasons, while for thick films ( $\sim 500$  nm) the band gap is determined through  $E_{3.5}$  and the Tauc band gap.

### Electrical conductivity and activation energy

The photo- ( $\sigma_p$ ) and dark- ( $\sigma_d$ ) conductivity as well as the activation energy ( $E_A$ ) of the dark-conductivity are measured on thick films deposited onto Corning glass. Aluminium coplanar contacts are evaporated on the film.

The  $\sigma_d$  is measured in the vacuum after annealing the samples at  $160^\circ\text{C}$  for 90 minutes. A voltage of 100V is applied during the measurement. The  $E_A$  is determined from the slope of the  $\ln(\sigma_d)$  against the inverse of the temperature during the controlled cooling process.

The  $\sigma_p$  is determined from the current measured under AM1.5 condition generated by a WACOM dual source solar simulator. Measuring the photocurrent, the  $\sigma_p$  is obtained through the relation

$$\sigma_p = \frac{I}{Vwd} \quad (2.2)$$

where  $I$  is the photocurrent,  $l$  is the length of the contacts,  $V$  is the applied voltage,  $w$  is the distance between the contacts and  $d$  is the thickness of the film.

### Constant photocurrent method (CPM)

Due to the absorption of  $a\text{-Si:H}$ , the small thickness of the film ( $\leq 1 \mu\text{m}$ ) does not permit one to measure  $\alpha$  for energies below 1.2 eV by R-T techniques. The sub-band gap absorption spectrum (where the  $\alpha$  is below  $10^3 \text{ cm}^{-1}$ ) is then measured by other techniques as photothermal deflection spectroscopy (PDS) and constant photocurrent method (CPM). For CPM, the intensity of a monochromatic light is adjusted in order to keep a constant photocurrent, while the photon energy of the monochromatic light is varied between 0.8 and 2.2 eV. The  $\alpha$  is measured in a relative scale from the relation  $\alpha(E) \propto 1/F(E)$ , where  $F(E)$  is the photon flux. This provides a relative value for  $\alpha$  that must be adjusted with the absolute  $\alpha$  obtained

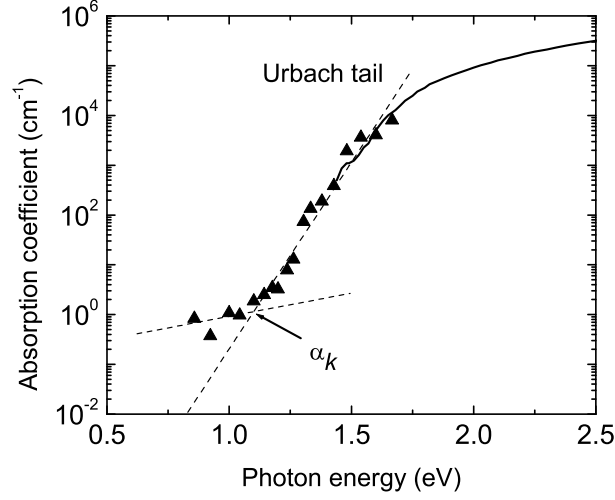


**Figure 2.1:** Absorption coefficient spectra of *a*-SiGe:H measured by RT (black line) and by CPM ( $\triangle$ ).  $\alpha_k$  represents the cross point where a deviation from the pure exponential trend of the Urbach tail is found.

by RT measurements at the photon energy region. The region where both the  $\alpha$ s overlap depends on the alloy composition. For the material presented in this study, this region is between  $1 \times 10^3$  and  $8 \times 10^3 \text{ cm}^{-1}$ .

Two important parameters can be deduced from the analysis of  $\alpha$ :

- the Urbach energy,  $E_U$ , which characterised the disorder and can be related to the number of weak Si-Si bonds [11];
- the midgap defect density,  $N_D$ , which can be estimated from the crossover point,  $\alpha_k$ , where a deviation from the pure exponential trend of the Urbach tail occurs (see Fig. 2.1). The defect density is determined by

$$N_D = 10^{16} \alpha_k \quad (2.3)$$

where the calibration constant is from [12].

### Steady-state photocarrier grating technique (SSPG)

The photocarrier grating technique is based on the creation of a small-amplitude photocarrier grating on a uniform photocarrier background. The electronic transport of the photogenerated carriers is dominated by the less mobile carrier, normally the minority carrier (holes). The ambipolar diffusion length can be measured reliably with an accuracy better than 10% for diffusion lengths between 50-200 nm [13]. In addition to the ambipolar diffusion length, the value of  $\gamma$  is also obtained. The photo-conductivity in amorphous alloys follows a power law relation with the generation rate,  $G$  ( $\sigma_p \propto G^\gamma$ ). The exponent  $\gamma$  is related to the slope of the conduction band tail of the density of states (DOS) [14].

The SSPG experimental setup used in this study is explained in reference [15]. We only mention here the intensity of the HeNe laser (5 mW) and the DC voltage applied to the sample (10 V).

### Fourier-transform infrared spectroscopy (FTIR)

The Fourier-transform infrared spectroscopy (FTIR) determines the content of bonded H and the silicon-hydrogen and germanium-hydrogen bonding configurations. A Digilab FTS-40 spectrometer equipped with a liquid-nitrogen cooled HgCdTe detector is used to perform FTIR measurements. The samples are deposited on polished highly resistive *c*-Si wafer, which is suitable due to its low oxygen content. The measurements were corrected for both incoherent and coherent multiple reflections in the films [16,17]. The infrared transmission is measured in the wave number range of 400-4000  $\text{cm}^{-1}$  with a resolution of 2  $\text{cm}^{-1}$ . This region contains all the relevant  $\text{SiH}_x$ ,  $\text{GeH}_x$  and silicon-oxide bonding configurations.

The FTIR spectrum was deconvoluted with Gaussian absorption profiles for the desired vibrational modes. The number of one kind of bond  $N$  at a discrete frequency  $\omega$  is calculated from the absorption spectra following the equation

$$N = A_k I_k = A_k \int \frac{\alpha(\omega)}{\omega} d\omega \quad (2.4)$$

where  $A_k$  is a proportionality constant for the vibrational mode  $k$  and  $I_k$  is the integrated absorption of a peak corresponding with the vibrational mode  $k$ .

The bonding configurations surveyed in this study together with their proportionality constants are displayed in Table 2.2.

The vibrational mode at 2080-2090  $\text{cm}^{-1}$  is cause of debate [19]. Clustered H atoms or hydrogen at internal surfaces of the voids are more tightly bounded

**Table 2.2:** Characteristic vibrational modes and proportional constants for *a*-SiGe:H used in this study.

Bond	Wavenumber (cm <sup>-1</sup> )	Assignment	A <sub>k</sub> (10 <sup>20</sup> cm <sup>-2</sup> )	Ref.
SiH	2000	Stretching	1.2	[17]
SiH <sub>2</sub>	2080-2090	Stretching	1.7	[17]
GeH	1880	Stretching	0.6	[18]
GeH <sub>2</sub>	1980	Stretching	0.6	[18]

to the Si, shifting their stretching mode to higher frequencies ( $\sim 2080 \text{ cm}^{-1}$ ). Therefore it is not possible to distinguish between SiH on voids and SiH<sub>2</sub>. The hydrogen-bonding configuration is characterized by the microstructure parameter  $R^*$ , defined as

$$R^* = \frac{I_{2080}}{I_{2000} + I_{2080}}. \quad (2.5)$$

A high microstructure parameter is often a sign of high void density material.

### Raman spectroscopy

The Raman effect consists of an inelastic scattering of a photon by a solid material with the creation or annihilation of one or two phonons. The local environments in the material influence the scattering processes. Thus, in the *a*-SiGe:H material case, the phonon peak frequency is affected by the composition of the alloy as well as by structural strain. This permits one to correlate the amount of Ge in the material with the position of the vibrational mode for Si-Si bonds, the most sensitive to the alloying process [20].

The Raman spectra were decomposed into the characteristic amorphous or crystalline transverse optical modes (TO) for Si-Si, Si-Ge and Ge-Ge bonding. Together with these modes, three extra modes were necessary to fit the Raman spectra. The new modes are the following: a mode at 200-230 cm<sup>-1</sup> associated with a resonant mode or to an extent to induced disorder associated with the Ge LA band [21]; two weak modes at 430 cm<sup>-1</sup> and 450 cm<sup>-1</sup> related to the Si-Ge and Si-Si phonon bands, respectively [20]. The fitting of one of the spectrum is shown in Figure 2.2. By comparing the ratio Ge-Ge/Si-Ge of the measured material with a theoretical random distribution, the degree of Ge clustered in the material can be evaluated [22].

Raman spectra were measured using the 514.5 nm line of a Spectra-Physics Ar<sup>+</sup> laser, a Spex triple-grating monochromator, and a liquid-nitrogen cooled

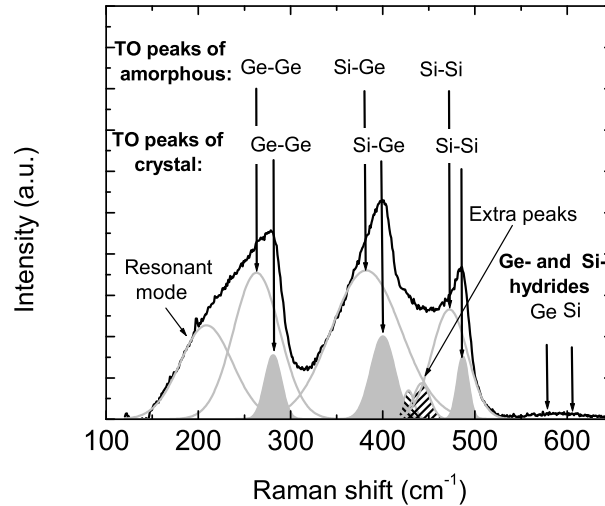


**Figure 2.2:** Decomposition of the Raman scattering spectrum for  $a$ -SiGe:H. Three amorphous peaks and three crystal peaks (filled in grey) are shown. The two extra peaks around  $450 \text{ cm}^{-1}$  are filled with lines.

CCD detector (Roper Scientific). The probing depth with this wavelength is  $\sim 60 \text{ nm}$  for amorphous material.

## 2.2.2 Solar cell characterization

### Current-voltage characterization (J-V)

Solar cell characterization is usually done studying the dependence of the output current on an applied voltage, known as J-V characteristic. The measurement can be carried out in the dark or under light conditions. The most important parameters obtained from the J-V characteristic under illumination conditions are the following (see Fig. 2.3):

- the short circuit current ( $J_{sc}$ ), is the current of the solar cell in short circuit conditions. The  $J_{sc}$  is equal to the photogenerated current ( $J_{ph}$ ) in an optimal solar cell,
- the open circuit voltage ( $V_{oc}$ ), is the applied voltage for which the current is zero,

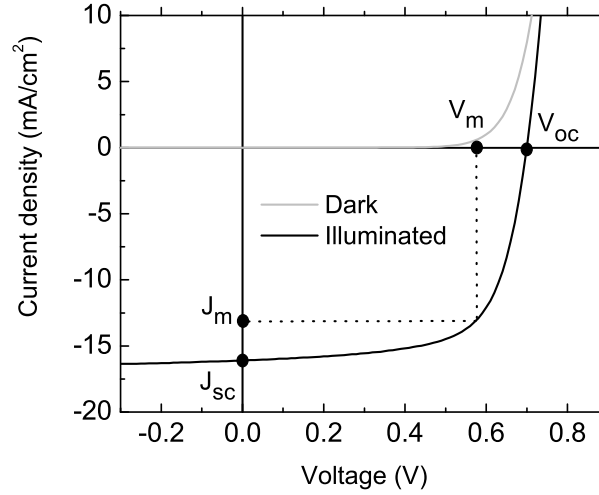


**Figure 2.3:** The J-V characteristics of an *a*-SiGe:H solar cell under AM 1.5 and dark conditions.

- the fill factor (FF), is a measurement of the "squareness" of the J-V characteristic, being defined as

$$FF = \frac{J_m V_m}{J_{sc} V_{sc}} \quad (2.6)$$

where  $J_m$  and  $V_m$  are the current and voltage at the maximum power point ( $P_{MAX} = J_m V_m$ ),

- the energy conversion efficiency ( $\eta$ ), is defined as

$$\eta = \frac{P_{MAX}}{P_{in}} \quad (2.7)$$

where  $P_{in}$  is the power of the incident radiation.

An electrical approach to describe the J-V characteristic of an ideal solar cell is reached applying the superposition principle. In accordance with this principle the light J-V characteristic is the result of translating downward the dark J-V

characteristic by the magnitude of the light generated current. In real solar cells there are power losses due to the resistance at the interfaces between the different layers that form the solar cell or current leakage paths. The superposition principle is then corrected with the incorporation of series ( $R_s$ ) and parallel ( $R_p$ ) resistance. The solution of this electric circuit gives the total current density through the solar cell as

$$J = J_0(\exp[e(V - JR_s)/nk_B T] - 1) + \frac{V - JR_s}{R_p} - J_{ph} \quad (2.8)$$

where  $J_0$  is the reverse-bias saturation current density,  $n$  is the diode quality factor,  $k_B$  is Boltzmann's constant,  $T$  the absolute temperature and  $e$  the elementary charge. The diode quality factor takes a value close to 1 in the case of diffusion-drive current or to 2 in the case of pure recombination-drive current. The value of  $J_0$  and  $n$  is determined by the dark J-V characteristic. A detail description of the origin of these parameters can be found in reference [2].

The dark and light J-V characteristics can be numerically obtained by solving the basic semiconductor transport equations, i.e. the hole and electron continuity equations and the Poisson's equation. This approach permits one to obtain an estimation of other solar cell characteristics not easily measured by existing methods.

The illumination condition for measuring the J-V characteristic under illumination were created with a WACOM dual source solar simulator, in which illumination from a halogen lamp and a xenon lamp are mixed. The simulator provides illumination with an AM 1.5 spectrum at an intensity of 100 mW/cm<sup>2</sup>.

### Spectral response (SR) characterization

When a monochromatic light at a wavelength  $\lambda$  probes the solar cell, biased at a voltage  $V$ , the number of carriers collected per incident photon at  $\lambda$  can be derived from

$$\eta_{col}(\lambda, V) = \frac{J_{ph}(\lambda, V)}{e\phi_0} \quad (2.9)$$

where  $\phi_0$  is the number of photons per unit area per second and  $e$  is the elementary charge. The parameter  $\eta_{col}$  is known as external collection efficiency or spectral response. The generation rate ( $G$ ) of electron-hole pairs in the solar cell has an inverse exponential dependence on  $\lambda$  and on the distance inside the solar cell

from the surface on which the light enters the solar cell ( $G \sim e^{-\alpha x}$ ). This property allows the spectral response technique to distinguish the contribution to the photocarrier collection from different regions of the solar cell. The short wavelengths are absorbed more strongly than the long wavelengths, generating carriers in the front and the bulk of the solar cell, respectively.

The measurement of tandem solar cells was done following the work of Burdick et al. [23]. A 1000 W xenon lamp was filtered to obtain bias light in the desired spectrum range. The blue bias light was obtained with a BG25 filter, while the red bias light was obtained with a OG570 filter. With the suitable spectrum range in the bias light, one of the cells that forms the tandem is saturated, generating a current close to the  $J_{sc}$  of the individual cell. The SR is measured under short circuit conditions, which creates a negative voltage on the limiting cell in opposition to the voltage created due to the bias light in the saturated cell. Applying to the tandem cell a positive voltage close to the  $V_{oc}$  of the saturated cell, the SR will measure the spectral dependence of the limiting cell.

The investigation of the SR for high energy photons, which do not reach the back surface, provides information about the effective diffusion length,  $L_{eff}$ . To study this internal process, SR must be corrected from the external optical effects (the total reflectance of the cell), leading to the fraction of photons absorbed in the solar cell that are collected under short circuit conditions. The corrected SR is known as internal quantum efficiency (IQE). The inverse of the IQE shows a linear relation with the inverse of  $\alpha$ , which slope is proportional to  $L_{eff}$  (Eq. 2.10) [24]. The proportionality constant depends on the surface roughness defined as the average path angle of the photons with respect to the cell's normal vector,  $\theta$ .

$$IQE^{-1} = 1 + \alpha^{-1} \frac{\cos(\theta)}{L_{eff}} \quad (2.10)$$

### 2.3 Degradation

The light induced degradation facility used in this study consists of a large box with dimensions of  $1 \times 1 \times 1.35 \text{ m}^3$ . A fixed glass platform serves as a holder for the samples. The samples are illuminated from underneath the platform by a series of lamps and a mirror system in a housing. The housing is box type with the horizontal size of  $30 \times 40 \text{ cm}$  and a height of 60 cm, and it is located 5 cm below the platform. It is made from four vertically and one horizontally (at the bottom) placed mirrors.

The housing encloses a system of Osram halogen lamps with a power of 150 W each and two Philips MHN-TD 250 W metal halide lamps aligned sym-

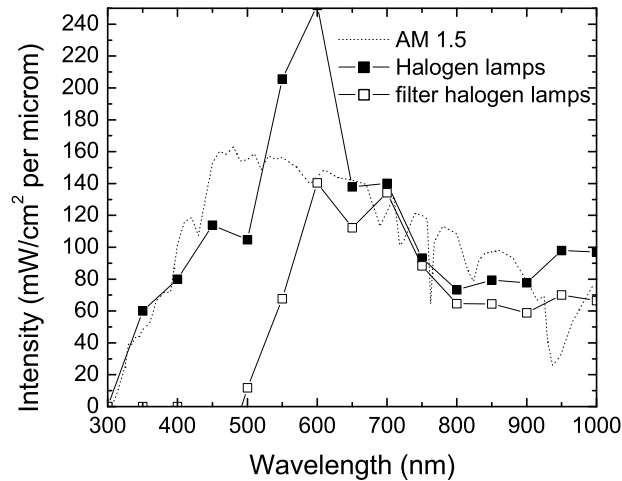


**Figure 2.4:** Comparison of the standard solar spectrum (AM 1.5) with the spectrum generated by the lamps of the light soaking facility with and without the filter used with the *a*-SiGe:H solar cells

metrically with respect to the mirrors. These lamps are located at the bottom of the housing a few centimeters above the horizontal mirror. The lamps are easily accessible and replaceable. Within the spectral sensitivity of amorphous silicon solar cells, the light provided by these lamps approximates the standard spectrum of AM1.5. Figure 2.4 shows the comparison of the standard solar spectrum (AM1.5) with the spectrum generated by the lamps of the light soaking facility. The spectrum is measured using a Hamamatsu reference detector with and without the filter used for the *a*-SiGe:H solar cells [25].

The light intensity at the sample platform is around  $90 \text{ mW/cm}^2$  over an area of  $\pm 0.1 \text{ m}^2$ . To determine the uniformity of illumination, the light intensity was measured over the entire area of the sample platform using the Hamamatsu reference detector and an amorphous silicon solar cell. The uniformity is achieved by multiple reflections provided by the mirror arrangement. A mechanism that ensured stable temperature of the samples within the range of  $50 \pm 2 \text{ }^\circ\text{C}$  was designed. The mechanism consists of heat sinks directly attached to the mirror housing and supported by blowers. The cell temperature was continuously monitored through thermocouples attached to a reference cell on the sample platform.



## 3 Deposition of *a*-SiGe:H at low temperatures and high deposition rate

---

### 3.1 Introduction

Since the discovery of the light-induced degradation in *a*-Si:H, the Staebler-Wronski effect has been the subject of intensive studies. Understanding the process, improving the stability of the material under light exposure and developing solar cells with higher stable efficiencies have been the steps followed in order to overcome the principal obstacle of thin film solar cells. The models proposed to explain the Staebler-Wronski effect are reviewed in Chapter 5. Improved light-stability in *a*-Si:H has been observed for depositions under very high H<sub>2</sub> dilution conditions. It is suggested that these conditions promote the formation of microcrystals, improving the medium range order in the material [26]. In solar cells, reduction of the degradation can be achieved by using tandem structures where thinner solar cells are less sensitive to light-induced degradation. The top junction consist of *a*-Si:H. For the bottom junction, *μc*-Si:H as well as *a*-SiGe:H is being used. The state of the art for *a*-SiGe:H has not reached, until now, the levels for *a*-Si:H. There is no report about *a*-SiGe:H where the medium range order has been improved.

Furthermore, the development of more stable materials must be achieved within technically friendly conditions. Lower substrate temperatures permit cheaper substrates and no material damage to previously deposited layer. At the same time, higher deposition rates reduce the time of production and the final cost of the solar cell.

In this chapter, processes leading to *a*-SiGe:H with high stability are studied for the low deposition temperature regime. Deposition conditions under the onset of crystalline formation are used to obtain a material with improved medium range order. This material will be addressed as protocrystalline material. The chapter presents results on higher deposition rates by employing Si<sub>2</sub>H<sub>6</sub> as feed gas instead of SiH<sub>4</sub>.

### 3.2 Growth of *a*-Si:H by PECVD

The growth processes of *a*-Si:H determine to a large extent the optical, structural and electrical properties of the *a*-Si:H material and the performance of the *a*-Si:H devices. The understanding of these processes as well as the correlation between the deposition conditions and the final properties of the material, points to the optimization of the deposition conditions.

The deposition by an rf PECVD discharge can be divided into four steps:

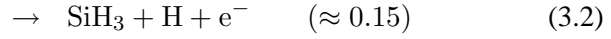
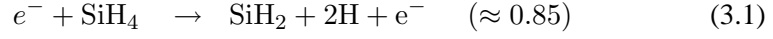
1. Initially, electron-impact excitation, dissociation and ionization of the precursor gasses generate the primary constituents of the plasma, in which they react through gas phase reactions.
2. The gas phase reactions are determined by the plasma physics and chemistry. They can be divided into:
  - primary reactions, leading to neutral radicals together with ions
  - secondary reactions, leading to higher radicals (species with higher mass than the species of the feed gasses, formed by successive reactions) and nanoclusters.

These conditions define the flux and nature of the reactive species diffusing from the plasma to the substrate.

3. Plasma-surface interactions, such as physisorption and chemisorption, diffusion, etching and abstraction by reactive species, define the conditions on the growing surface that result in the film formation. Modification of the growth surface by atomic hydrogen is also part of this process.
4. The final step is the series of reactions taking place in the growing zone. Cross-linking reactions result in the formation of the film and relaxation of the matrix.

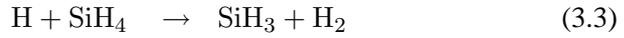
As a first step in understanding the growth process, it is necessary to define the growth chemistry that can lead to a predictable growth from only one kind of species. For a silane plasma at low pressures, low silane dissociation and at temperatures above 200 °C, primary reactions alone are sufficient to describe *a*-Si:H deposition. Ignoring the contribution of positive and negative ions, which is much smaller than the neutral radical contribution for pressures above  $10^{-2}$  mbar [27], the primary  $\text{SiH}_4$  dissociation involves energetic electron ( $\geq 8$  eV) impact disso-

ciation into SiH<sub>m</sub> (m ≤ 3) radicals and H atoms. The dominant processes are [28]:



where the numbers in brackets represent the branching fractions. Both H and SiH<sub>2</sub> react with SiH<sub>4</sub>, leading to

- the H abstraction reaction, which increases the overall amount of SiH<sub>3</sub>



- and SiH<sub>2</sub> elimination, promoting higher radicals.



The species SiH<sub>3</sub> does not react with SiH<sub>4</sub>, and thus it becomes the dominant species in the growth process. Secondary reactions are significant for higher pressures, which promote chain reactions resulting in polymerization, or higher rf power, which promote reactions between SiH<sub>3</sub> with other SiH<sub>3</sub>, limiting the flux of SiH<sub>3</sub> towards the growing surface.

Even in the simplified settings of only one species contributing to the deposition, the growth process is still controversial. Several models have emerged to explain the optimum deposition condition for *a*-Si:H at ~250 °C. They attribute the growth to only SiH<sub>3</sub> species and usually emphasize the importance of the mobility of the radicals and H at the growing surface, but they differ in the physical and chemical details.

Matsuda et al. [29,30] proposed that the growth is controlled by a process at the surface. Once the precursor is physisorbed at the surface, the growth is limited by the diffusion of the precursor on the growing surface. The diffusion length of the precursor is defined by the activation energy of the surface reactions that the precursor undergoes. These reactions are the following:

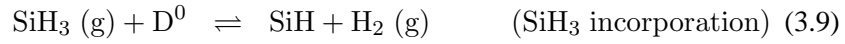


where D<sup>0</sup> represents a dangling bond. The diffusion length is then defined as:

$$l = [2D_s\tau_s]^{1/2} \quad (3.8)$$

where  $D_s \propto e^{-E_s/kT}$  is the diffusion coefficient with  $E_s \sim 0.2-0.3$  eV and  $\tau_s$  is the residence time on the surface before the precursor reacts. Recently Vigneron et al. have proposed a higher value for  $E_s$  ( $\sim 0.7$  eV) [31]. For low temperatures (below 250 °C)  $D_s$  decreases and therefore the diffusion length decreases. On the other hand, at high temperatures (above 300 °C) the surface H desorbs, creating dangling bonds which reduce  $\tau_s$  and therefore the diffusion length decreases. As a result, the optimum  $T_s$  is  $\sim 250$  °C. In accordance with this model, enhancing the material properties would consist in finding new ways of improving the diffusion length of the precursor.

Winer [32] assumed that the quality of the material is determined by the thermodynamics of the following chemical reactions in equilibrium, taking place *at* or *below* the growth surface rather than in the plasma. These reactions are mediated through thermal diffusion of H.



The plasma is seen as a source of reactive species. The optimal growth is obtained when the average rate of H diffusion ( $\nu_H$ ), defined in the time interval  $\Delta t$ , approximately matches the deposition rate ( $R_d$ )

$$\nu_H \equiv \left(4 \frac{D_H}{\Delta t}\right)^{1/2} \approx R_d \approx 4 \frac{D_H}{L} \quad (3.12)$$

where  $D_H$  is the H diffusion constant,  $L \equiv R_d \Delta t \sim 1 \text{ \AA}$  is the depth from the growing surface where the equilibrium growth process occurs and  $\Delta t$  is a time interval for equilibration. When the equilibrium is achieved, reactions 3.9 to 3.11 reach equilibrium during the deposition time, i.e. the H diffusion is high enough to allow thermal equilibrium conditions. The model predicts that the optimal  $T_s$  is given by the temperature at which  $\nu_H = R_d$ , for a given rf power (deposition rate). For a rf power of the order of 10 W the optimal  $T_s$  has a value of  $\sim 250$  °C. In this model the plasma power and the deposition temperature determine the material properties.

This model has been more elaborated in the hydrogen density of states model (HDOS) proposed by Street, taking into account the evolution of the chemical potential of the H in the plasma and on the growing surface [11], which tend to equalize. One important conclusion of the thermal equilibrium model is that the defect concentration in the material cannot be made arbitrarily small, but is limited by the disorder of the material (characterized by the Urbach energy).

Modifying the thermal equilibrium model, Hata et al. [33] proposed a quasi-equilibrium model where the surface defects formed during growth are annealed during deposition. The equilibrium is then developed through the *entire* thickness of the film and not only at the growing surface. The dependence of the defect density on the film thickness is explained by the depth dependent decay of the surface defects induced during deposition. The dependence of the defect density on the substrate temperature derives from the different annealing rate of defects by the substrate temperature.

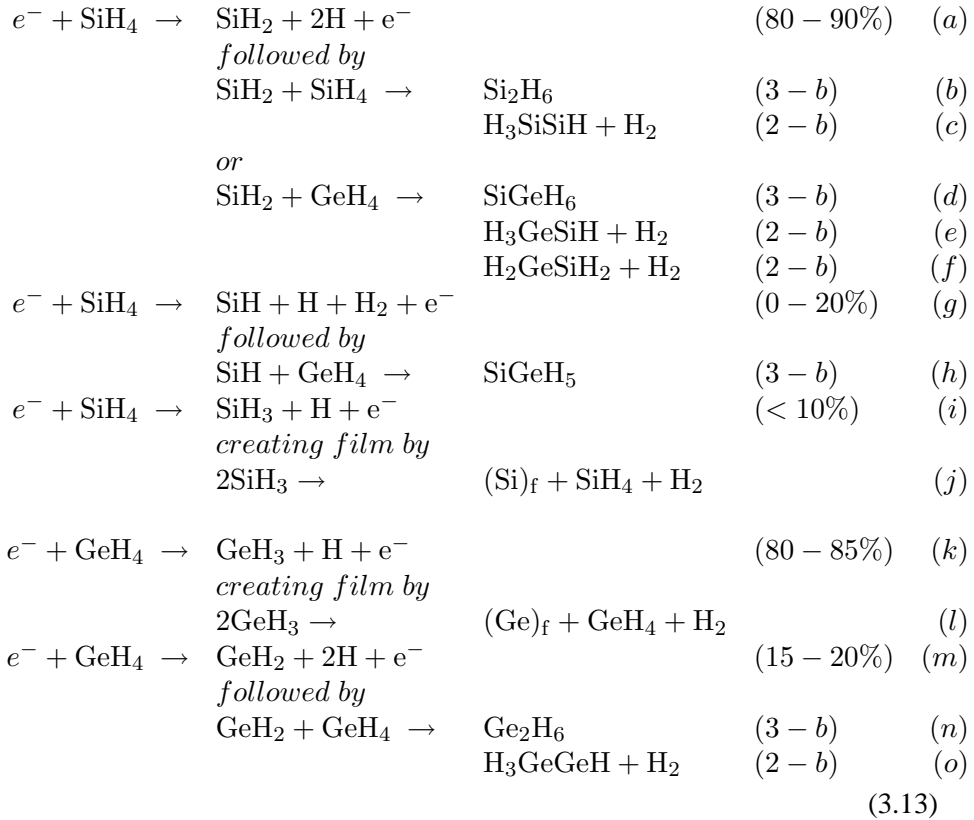
Away from primary reactions conditions, technology demands for higher deposition rates to reduce production cost, and for low deposition temperatures, which are needed to avoid damage to the underlying deposited layers [34]. Under these deposition conditions, secondary reactions are no longer negligible and determine the film quality. The effect of secondary reactions is mainly the formation of clusters. Higher silane radicals (due to their slow diffusion) and negative ions (because they are trapped in the plasma) have a long residence time in the plasma bulk and can eventually react with other species leading to powder (negatively charged). As the powder is negatively charged and trapped in the plasma, it is expected that clusters undergo polarity changes to allow them to escape the plasma, contributing to growth. As a result, a whole range of small particle sizes in the bulk of the plasma reach the surface during deposition. There is no clear picture of the effect of these small particles on film properties, which may explain the different conclusions by different groups [35,36,37,38]. Thus, for example, Roca i Cabarrocas et al. [38] have deposited *a*-Si:H material (so called polymorphous) under plasma conditions where silicon clusters together with radicals contribute to the growth. The size of the clusters can be selected by modifying the pressure. They claim that the clusters help to create films with medium range order, thanks to the presence of microcrystallinity regions [39]. The medium range order improves the transport properties and stability with respect to standard *a*-Si:H (see Section 5.4). They are able to deposit amorphous as well as microcrystalline material.

### 3.3 Growth of *a*-SiGe:H by PECVD

In the previous section the complexity of the *a*-Si:H plasma was stressed. The variety of radicals generated can easily lead to inhomogeneous growth if the conditions are poorly controlled. For the growth of *a*-SiGe:H the process becomes more complex. The two primary precursors, SiH<sub>4</sub> and GeH<sub>4</sub>, decompose at very

different rates. For 100 eV<sup>1</sup> electrons, the total dissociation cross section for GeH<sub>4</sub> is 2 times higher than for SiH<sub>4</sub> and the threshold for GeH<sub>4</sub> dissociation is 2 eV lower than for SiH<sub>4</sub>, which enhances the dissociation of GeH<sub>4</sub> over SiH<sub>4</sub>. A 2 to 6 times higher dissociation rate is expected for GeH<sub>4</sub> than for SiH<sub>4</sub> [28,42], depending on the deposition conditions and the measuring method used.

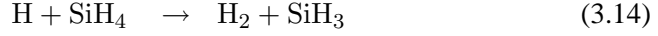
Following the work of Doyle [28], the most significant chemical reactions taking place in a SiH<sub>4</sub>-GeH<sub>4</sub> plasma dominated by electron collisional dissociation are the following:



where 2-*b* and 3-*b* stands for 2-body and 3-body reaction. The complex H<sub>2</sub>GeSiH<sub>2</sub> (reaction 3.13f) is expected to contribute to growth, while the other products of the 2-body reactions react with SiH<sub>4</sub> or GeH<sub>4</sub> to create higher radicals. Finally,

<sup>1</sup>In the range of 20-100 eV the total capture cross section for SiH<sub>4</sub> varies between 5-10×10<sup>-16</sup> cm<sup>2</sup>, for Si<sub>2</sub>H<sub>6</sub> varies between 10-25×10<sup>-16</sup> cm<sup>2</sup> while for GeH<sub>4</sub> at 100 eV it is 20×10<sup>-16</sup> cm<sup>2</sup> [40,41].

the H would react to produce:



Typical rate constants for neutral dissociation and dissociative ionization in rf plasmas for  $\text{SiH}_4$  are  $10^{-10} - 10^{-9} \text{ cm}^3\text{s}^{-1}$  and  $10^{-12} - 10^{-11} \text{ cm}^3\text{s}^{-1}$ , respectively.

The growth of *a*-SiGe:H can be described by considering first the reactions of  $\text{SiH}_4$  alone (reaction 3.1). When  $\text{GeH}_4$  is added, Doyle et al. have observed [28] that  $\text{Si}_2\text{H}_6$  production (reaction 3.13b) decreases because the radical  $\text{SiH}_2$  preferentially reacts with  $\text{GeH}_4$ , producing  $\text{SiGeH}_6$  and  $\text{H}_2\text{GeSiH}_2$  (reactions 3.13d and 3.13f). This last radical is not very reactive and should reach the substrate, contributing to growth. The efficiency in Si incorporation in the material is thus increased by the addition of  $\text{GeH}_4$ . On the other hand, most of the H (from reactions 3.13a, 3.13g, 3.13i, 3.13k and 3.13m) will react with  $\text{GeH}_4$ , due to its higher rate constant<sup>2</sup>, compensating the losses of  $\text{GeH}_3$  due to the reaction of  $\text{GeH}_4$  with  $\text{SiH}_2$ . In this way, the efficiency of Ge deposition remains roughly constant. The  $\text{SiH}$  is assumed to react with  $\text{GeH}_4$  contributing to growth (reaction 3.13h).

The final amount of Si and Ge incorporated in the film also depends on the sticking coefficient of each of the species. The sticking coefficient of  $\text{GeH}_3$  is 2 times higher than that of  $\text{SiH}_3$ . The weaker Ge-Ge surface bond may react easier with  $\text{GeH}_3$ , promoting the addition of Ge to the film, and possibly, the formation of Ge clusters. Moreover, H elimination from the Ge growing surface is much easier than from Si, which contributes to the higher density of defects in *a*-SiGe:H alloys with respect to *a*-Si:H. The structural properties and defect density will be discussed later.

From the discussion above, it is understandable that alloying *a*-Si:H produces a material with electrical properties that are not as good as those of the original material; the properties deteriorate with the degree of alloying. Although the reasons are still not fully understood, the well accepted ideas are

- a preferential attachment of H to Si over Ge, which leads to an increase in Ge dangling bond density [45];
- formation of microstructure (voids, clusters) [46] and
- thermal equilibrium effects according to the thermal equilibrium model, which result in higher defect densities for low band gap material [32] (the

<sup>2</sup>The rate constant for reaction 3.14 is in the range of  $4 \times 10^{-13} - 8 \times 10^{-12} \text{ cm}^3\text{s}^{-1}$  [43], whereas for reaction 3.15 the rate constant varies around  $2 \times 10^{-12} - 4 \times 10^{-10} \text{ cm}^3\text{s}^{-1}$  [44].

defect density increases when the difference between the energy level of the defect and the valence band edge decreases; in low band gap materials this difference is smaller than in wider band gap materials).

All the processes mentioned above modify the electronic properties through a change in the  $\mu\tau$  product.

To overcome these limitations various alternative deposition methods to the standard ones have been used (for example by remote electron-cyclotron-resonance (ECR) or higher frequencies than the standard PECVD techniques (VHF)), and different dilution gasses or deposition conditions have been tried (dilution gasses as  $F_2$  or Ar or deposition conditions near the powder regime).

In this research, the development of better and technologically friendly *a*-SiGe:H material is pursued by using high dilution with  $H_2$  of the precursor gasses, by depositing at low substrate temperatures, and by using  $Si_2H_6$  instead of  $SiH_4$ . In the following sections the influence of these parameters is discussed and the experimental results presented. In the next subsections, the motivation for changing these deposition parameters is given.

### 3.3.1 Hydrogen dilution of *a*-SiGe:H

The Ge-related radicals have a smaller surface diffusion coefficients on the growing surface than the Si-related radicals [45]. Moreover, the H bound to Ge thermally dissociates at lower temperatures than bound to Si. These two characteristics make Ge rich surfaces very reactive, reducing the surface diffusion of adsorbed radicals.

Supposing that the surface diffusion coefficient of precursors is the limiting parameter (as in the surface diffusion model [29,30]), an increase in the atomic H flux towards the surface would cover the growing surface better. This would increase the diffusion coefficient and decrease the number of Ge clusters. A higher  $H_2$  dilution would provide this extra amount of atomic H by the dissociation of  $H_2$  which in turn promotes the reactions 3.14 and 3.15 over the electron dissociation [47]. Nevertheless, this idea is under discussion due to the experiments of Matsuda [48] and Tachibana [49]. They observed how the density of atomic H in a  $SiH_4$  plasma decreases upon dilution with  $H_2$ . Taking into account the lower dissociation energy of  $GeH_4$  with respect to  $SiH_4$ , this result would be directly applicable to the  $SiH_4$ - $GeH_4$  plasma.

It is therefore proposed that a higher  $H_2$  dilution prevents the formation of radicals with a short lifetime due to the reaction with  $H_2$  instead of with other radicals. This applies in particular to Ge-related radicals because of the preferential depletion of  $GeH_4$  [50].

Finally, Street's model (modified thermal model) explains the improvement with H<sub>2</sub> dilution as follows [51]. Increasing the dilution causes an increase in the atomic H at the growing surface and the chemical potential of the H thus becomes closer to the energy of mobile H. At the same time, the deposition rate decreases. This gives time to optimize the local bonding configuration by the interaction of H with the network until the density of weak bonds at the surface and the H content is minimized for the deposition conditions. As a result, the defect density decreases with an increase in dilution.

Another important role of H<sub>2</sub> dilution is its influence on the microstructure; as H<sub>2</sub> dilution increases, the material changes from amorphous (short range order) to microcrystalline (long range order). Mobile H atoms can diffuse deeply into the lattice at the growth temperature and can extract excess H, that otherwise would lead to voids and columnar growth. A higher density of atomic H removes the excess H more efficiently. The same results could be achieved by ion bombardment with energies not exceeding 5 eV. (Higher ion energy would damage the material). Xu et al. [52] corroborated the creation of oriented microstructures (related with the formation of crystals) with H<sub>2</sub> dilution and the reduction in the void density.

In summary, the effects of H<sub>2</sub> dilution on *a*-SiGe:H are

1. an increase in H coverage of the growing surface [53],
2. a selective etching of Ge-Ge weak bonds [22],
3. the production of a more homogeneous structure [54] and
4. the suppression of gas phase polymerization in the plasma [55].

A drawback of high H<sub>2</sub> dilution is the decrease in deposition rate, mostly due to suppression in the radical production and etching processes during growth.

With respect to the stability, recent studies [52,26] have shown that *a*-Si:H solar cells, which intrinsic layer was deposited under very high H<sub>2</sub> dilution conditions of the SiH<sub>4</sub>, exhibit higher stability values than *a*-Si:H solar cells under lower H<sub>2</sub> dilution conditions. Several groups [52,56] have proposed the presence of a more ordered nanocrystalline network induced by the atomic H as the cause of the higher stability. The material grown near the transition to microcrystalline phase is known as protocrystalline material. No study has been reported on the stability of protocrystalline *a*-SiGe:H. In Section 3.4.1 the growth of protocrystalline *a*-SiGe:H is studied, and in Chapter 5 the stability against light exposure of the material itself and in solar cell structure is presented.

### 3.3.2 Low substrate temperature deposition of *a*-SiGe:H

The substrate temperature is an important parameter related to the problem of surface mobility of growth species and desorption of H. Even though a minimum in the defect density has been observed at a temperature around 250 °C for *a*-Si:H, a review of the literature dealing with the substrate temperature shows that the substrate temperature has to be optimized for each individual deposition process and alloy composition. Winer [32] proposed that the optimal deposition temperature varies with the rf power. However, the necessity of higher deposition temperature when the deposition rate is higher is well accepted [57].

The surface temperature during deposition affects the H content in the film. High temperature results in a lower H content and a lower  $E_g$ . However, the H and Ge contents of *a*-SiGe:H films do not independently influence  $E_g$ , as observed by Terakawa et al. [58]

Two factors related to the deposition temperature govern the growing surface defect density and therefore the quality of the material. On the one hand, the surface mobility of precursors increases with the substrate temperature. As mentioned before, the Ge-related precursors are expected to limit the film quality due to their lower surface mobility. Increasing the substrate temperature, the mobility would be enhanced resulting in a better quality material (higher photosensitivity). Perrin et al. observed a sharp increase in the surface reaction probability,  $\beta$ , above 200 °C [59] supporting this previous supposition. Similar results are obtained if the amount of Ge-related precursors on the surface is reduced.

On the other hand, the H surface coverage increases with a reduction in the substrate temperature. The thermal desorption of H from the growing surface occurs principally from Ge-H bonds, due to a lower activation energy for H desorption than for Si-H bonds (desorption occurs even at 110 °C for Ge-H compared with the 350 °C needed for Si-H). If the amount of Ge-related precursors at the surface is reduced the H desorption would be reduced at the same time.

With these ideas in mind, Matsuda et al. [60] and Middy et al. [61] proposed essentially the use of feed gasses at a low flow (to reduce the amount of Ge precursors on the surface), high H<sub>2</sub> dilution (to increase the H coverage of the growing surface) and high temperatures (to promote the mobility of Ge precursors). They observe a maximum in photosensitivity at a deposition temperature of 200 °C.

However, a high deposition temperature during the fabrication of solar cells may result in degradation in the previously deposited layers, in particular when they are deposited at lower temperature. TCO coated glasses also degrade at high temperatures [34] in a H<sub>2</sub> plasma. Some groups have opted for n-i-p solar cell structures deposited on stainless steel substrates, due to the higher deposition temperature of the n-doped layer [62].

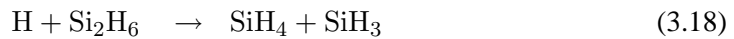
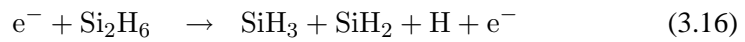
Zeman et al. [63] have recently shown how during the band gap profiling of *a*-SiGe:H solar cells, the initial layers deposited at lower dilution may have a higher Urbach energy than expected for a device quality material with a band gap of  $\sim 1.7$  eV. In computer simulations of solar cells with a graded intrinsic layer, the same high values for the Urbach energy of these materials are needed to simulate the external parameters. By decreasing the deposition temperature, the Urbach energy can be reduced to a value closer to device-quality material.

To avoid damage to the previously deposited layers during multijunction solar cell deposition as well as to prevent the inclusion of possible low quality material during the band gap profiling of *a*-SiGe:H solar cells, deposition at low substrate temperature is required.

### 3.3.3 Deposition of *a*-SiGe:H with Si<sub>2</sub>H<sub>6</sub>+GeH<sub>4</sub>

An advantage of using Si<sub>2</sub>H<sub>6</sub> instead of SiH<sub>4</sub> is that the dissociation rates of Si<sub>2</sub>H<sub>6</sub> and GeH<sub>4</sub> are very similar (see footnote on page 32). The difference in the dissociation rates of GeH<sub>4</sub> and SiH<sub>4</sub> is a factor between 2 and 6 [28,42], whereas the difference between GeH<sub>4</sub> and Si<sub>2</sub>H<sub>6</sub> dissociation rates is reported to be only 0.8 [42].

The study presented by Doyle et al. [28] proposed that the initial radical mix in the plasma remains similar to the SiH<sub>4</sub>+GeH<sub>4</sub> discharge. Thus, the flux of radicals contributing to growth is expected to be dominated by the same monoradicals (SiH<sub>3</sub> and GeH<sub>3</sub>) and higher radicals as in the SiH<sub>4</sub>+GeH<sub>4</sub> plasma. The study of Si<sub>2</sub>H<sub>6</sub> dissociation predicts a lack of disilicon radicals contributing to growth [28]. The reactions that may take place with Si<sub>2</sub>H<sub>6</sub> are the following:



While the Si<sub>2</sub>H<sub>6</sub>+GeH<sub>4</sub> plasma kinetics are similar to the SiH<sub>4</sub>+GeH<sub>4</sub> plasma, the explanation for the observed difference in the film quality between these two methods is not straightforward [64,65]. Using feed gasses with similar dissociation rates avoids the preferential depletion of one of them, in this case GeH<sub>4</sub>. Under deposition conditions where the GeH<sub>4</sub> is depleted, the presence of higher radicals and powder increases (see Equation 3.13). These higher radicals have surface reaction probabilities close to unity, and it can be expected that the sticking probabilities are also close to unity, i.e. the higher radicals can insert directly

into the SiH or GeH surface bonds. If these conditions are not optimized by ion bombardment or high hydrogen dilution, the presence of voids will create shadowed regions with unsaturated dangling bonds, a more disordered network and finally a highly defective material. By replacing SiH<sub>4</sub> with Si<sub>2</sub>H<sub>6</sub> the depletion of GeH<sub>4</sub> can be prevented, reducing the density of deep states.

Another source of difference between SiH<sub>4</sub> and Si<sub>2</sub>H<sub>6</sub> as feed gas could be a difference in the ion bombardment, due to the different optimal deposition conditions for SiH<sub>4</sub> and Si<sub>2</sub>H<sub>6</sub>. As will be shown in Section 3.5, other radicals than in SiH<sub>4</sub> plasma, such as Si<sub>2</sub>H<sub>5</sub>, must be contributing to the growth, which could affect the film properties.

An advantage that comes as a consequence of the similar dissociation rates, is the possibility of reaching a higher deposition rate while maintaining low structural disorder in the deposited material [66] as well as better uniformity in large area deposition.

### 3.4 Results in deposition of *a*-SiGe:H at low temperature

This section contains the characterization results of materials deposited with GeH<sub>4</sub>+SiH<sub>4</sub> at different substrate temperature. First, the results are presented to be discussed subsequently.

#### 3.4.1 Material properties

In order to investigate the influence of the deposition temperature on the properties of *a*-SiGe:H material at the edge of microcrystallinity, several series of materials were deposited in which the flow of hydrogen was changed for different substrate temperatures. The band gap was kept constant for all the series. The deposition temperature, T<sub>s</sub>, was controlled by heating the substrate holder. We have studied the range from 200 °C to 170 °C, because it was expected that this deposition temperature would best match that of the *a*-SiC:H p-doped layer of 160 °C.

The GeH<sub>4</sub>+SiH<sub>4</sub> flow was kept constant at 2.7 sccm. Hydrogen dilution, defined as  $f = \text{H}_2 / (\text{GeH}_4 + \text{SiH}_4)$ , was varied from  $f = 65\%$  to  $f = 85\%$ , the latter being the maximum value reachable by the deposition system. The very high dilution condition is expected to lead to material near the microcrystalline regime. The dilution could have been increased by decreasing the GeH<sub>4</sub>+SiH<sub>4</sub> flow. This procedure was not followed because it has the disadvantage of reducing the deposition rate and more importantly, it creates depletion of the source gasses (specifically GeH<sub>4</sub>), which would degenerate in higher radical formation (reactions 3.13) and low quality material [67,68].

Two different film thicknesses were deposited: thin films ( $\sim 100$  nm) as well as thick films ( $\sim 500$  nm).

Figures 3.1a and b show the deposition rate ( $R_d$ ) for three different dilutions as a function of the substrate temperature, for thin as for thick samples, respectively. Figure 3.1c and d show  $n_0$  for the same samples. The thin films show a deposition rate that is not dependent on the temperature. On the other hand, the dilution decreases the deposition rate, ascribed to the reduction of the fraction of the silane as well as of the germane gas. All the series for thin materials have a similar density, related with  $n_0$ , which is independent of  $T_s$ .

For the thick samples,  $R_d$  as well as  $n_0$  depend on  $T_s$  and on the  $H_2$  dilution ratio. The increase in  $H_2$  dilution reduces  $R_d$  (similar to the thin films case) except for the highest diluted series ( $f=85\%$ ), for which  $R_d$  is unexpectedly higher again at all the temperatures than for  $f=75\%$ . The values of  $n_0$  follow an inverse trend when compared with the microstructure factor,  $R^*$  (Fig. 3.3d) (more compact materials, high  $n_0$ , have lower  $R^*$ ). These differences are discussed in Section 3.4.2.

### Structural properties

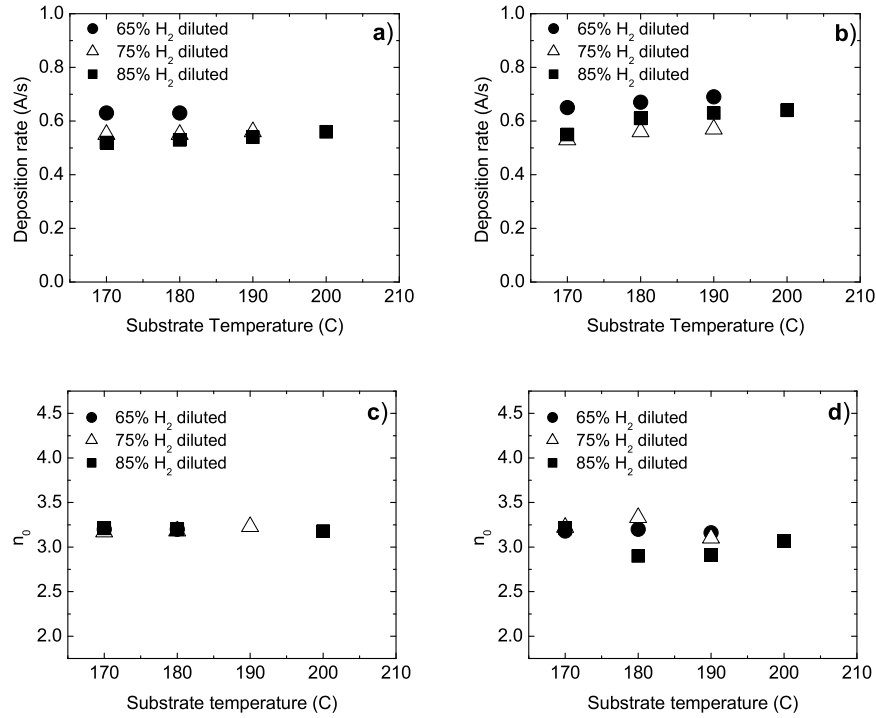
The structural properties were characterised by IR and Raman spectroscopy and by Rutherford Backscattering Spectrometry (RBS).

Figure 3.2 shows the Raman shift for the series under study. The Raman spectra were decomposed into the characteristic amorphous and crystalline transverse optical modes for Si-Si, Si-Ge and Ge-Ge bonding. An example of decomposition is shown on page 21.

By Raman spectroscopy, the presence of crystal structure and clusters, due to preferential Ge-Ge or Si-Si bonding, is investigated. The existence of these clusters is suggested (Section 3.3) as one of the causes of the poor electronic transport properties of *a*-SiGe:H [54].

Starting with the lowest dilution series ( $f=65\%$ ), no significant changes in the structure are observed by varying the  $T_s$ . The materials are amorphous with no clear sign of crystallinity, for both thin and thick films. The width of the amorphous peaks is too broad to distinguish the crystalline peaks, if any.

Increasing  $H_2$  dilution ( $f=75\%$ ) the crystalline peaks become visible. The variations in the Raman spectra in Fig. 3.2 show the genesis of the transition from amorphous to microcrystalline, in two ways. Firstly, the transition to microcrystalline structure is seen with the increase in the thickness. The material starts being amorphous (thin sample at  $T_s=190$  °C) to exhibit some microcrystalline structure in the thick sample ( $\sim 500$  nm). (The Raman spectra of the thin sample is virtually the same as that for the material deposited at  $T_s=170$  °C, thus it is not shown



**Figure 3.1:** Deposition rate and  $n_0$  value for thin (a and c) and thick (b and d) films respectively as a function of  $T_s$  for three different H<sub>2</sub> dilutions.

for clarity). Secondly, there is a transition to microcrystalline structure with  $T_s$ . The sample deposited at  $T_s=180$  °C does not have signs of microcrystalline structure, however at  $T_s=190$  °C the TO modes for crystalline Si-Si, Si-Ge and Ge-Ge clearly appear as shoulders at lower frequencies compared with the amorphous Raman spectrum of the sample at  $T_s=180$  °C.

When H<sub>2</sub> dilution is further increased ( $f=85\%$ ), pronounced resonance modes of crystalline Si-Si, Si-Ge and Ge-Ge appear. When the temperature is over 170 °C, the material steeply changes from being amorphous to display Raman peaks at the crystalline TO modes, indicating the presence of crystalline structure.

In summary, by increasing the dilution of source gasses with hydrogen during the deposition, the material has become partially microcrystalline. This is explained by the hydrogen etching the growing surfaces, which eliminates parts

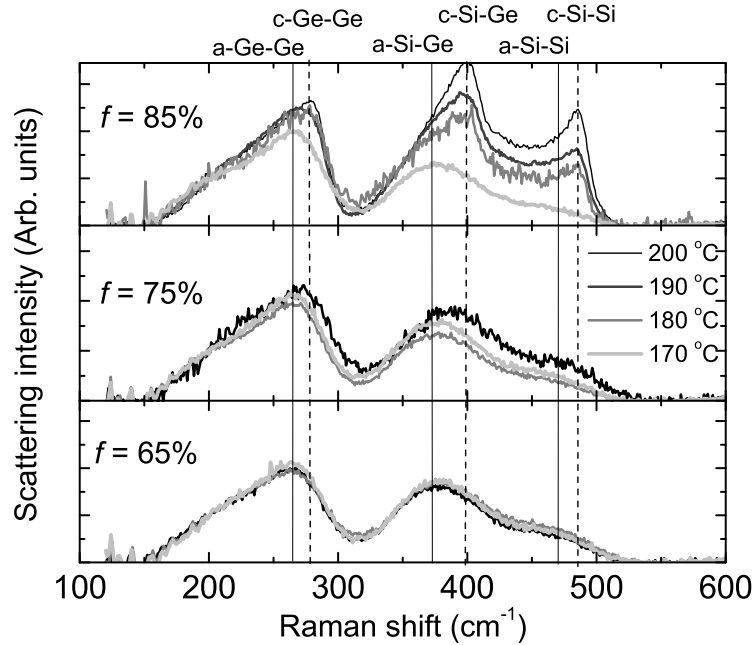


**Figure 3.2:** The Raman spectra of *a*-SiGe:H deposited at different  $T_s$  with several  $H_2$ -diluted ratio: a)  $f=65\%$ , b)  $f=75\%$  and c)  $f=85\%$ .

of the disordered configuration and strained or weak bonds. Thus the crystalline phase, with a lower energy configuration, remains in the structure. Low  $T_s$  reduces the H diffusion rate to values below the limit to allow changes in the bonding configurations. On the other hand, the hydrogen density of states model (HDOS) proposed by Street [11] suggests that lowering the  $T_s$  would raise the H chemical potential, accelerating the transition to crystalline growth. Section 3.4.2 will discuss the results in detail.

With respect to the H bonding configuration, Figures 3.3a to 3.3c show the infrared vibrational spectra for the three dilution series. The vertical lines in Figure 3.3a represent the position of the stretching mode for Si-H. Figure 3.3d shows the microstructure factor,  $R^* = I_{2080}/(I_{2000} + I_{2080})$ , for the three series. The shift in the position of the stretching mode for Si-H in *a*-Si:H has been related to the presence of microcrystalline structure [69]. In *a*-SiGe:H deposited at 200 °C

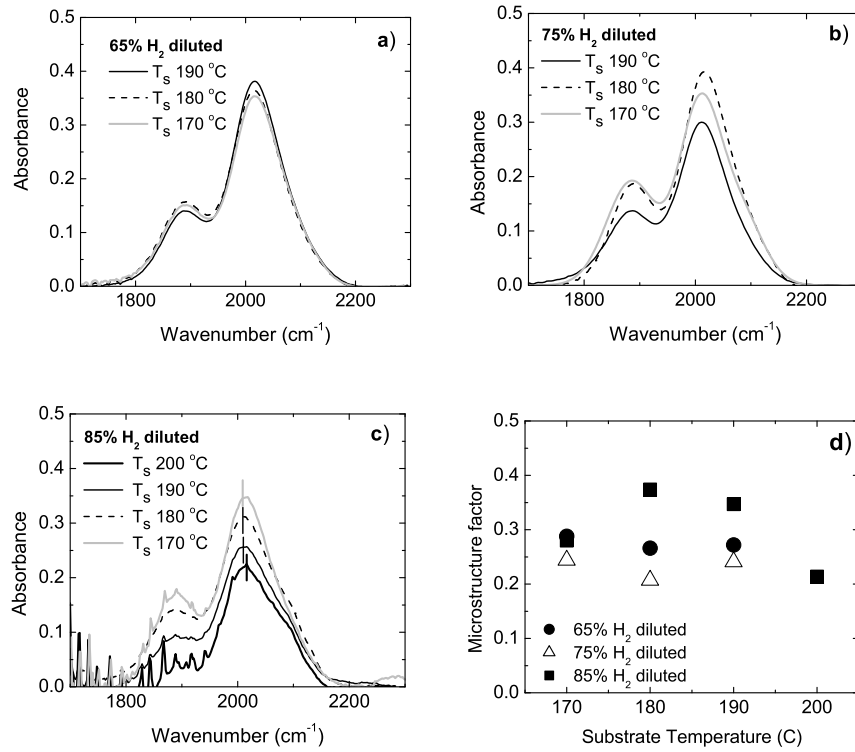


**Figure 3.3:** Infrared-absorption spectra of hydrogenated vibrational modes in *a*-SiGe:H grown at different T<sub>s</sub> under several H<sub>2</sub> dilution ratios: a)  $f=65\%$ , b)  $f=75\%$  and c)  $f=85\%$ . d) Microstructure factor for the same samples.

and  $f=85\%$ , the shift in the position of the stretching mode for Si-H can be related as well with the presence of microcrystalline structure, as Raman measurement corroborates (Fig. 3.2).

The H content in different bond configurations, for the dilution series under study, as a function of T<sub>s</sub> is shown in Figure 3.4. The total H and Ge contents in the material are shown in Figure 3.5. The materials with  $f=65\%$  exhibit no variation in  $C_{H(Si-H)}$ ,  $C_{H(Si-H_2)}$  or  $C_{H(Ge-H)}$  with T<sub>s</sub>, as well as in the total H and Ge content. For fully amorphous material at low T<sub>s</sub> and high H<sub>2</sub> dilution Shima et al. [70] have observed similar behaviour. When H<sub>2</sub> dilution is increased to  $f=75\%$ , the dihydride bonds decrease with respect to Si-H bonds. This is reflected in a lower microstructure factor with respect to  $f=65\%$  (Fig. 3.3d). The

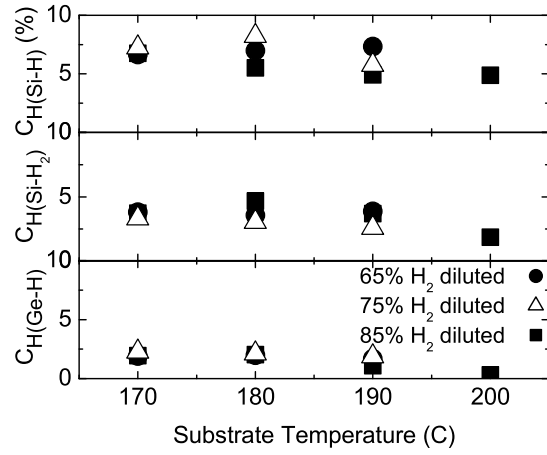


**Figure 3.4:** H content in different bond configurations of *a*-SiGe:H deposited at three different flows as a function of T<sub>s</sub>.

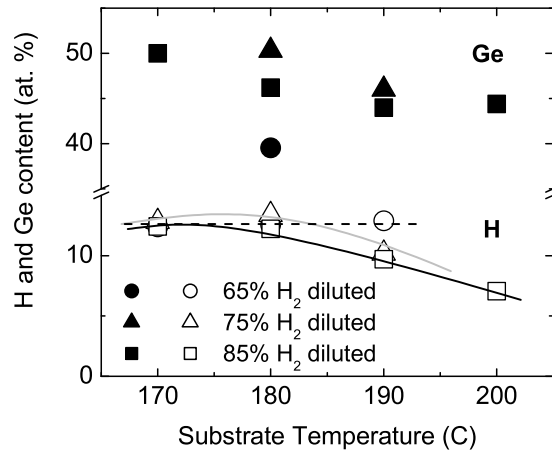


**Figure 3.5:** Total H and Ge content of *a*-SiGe:H deposited at three different flows as a function of T<sub>s</sub>.

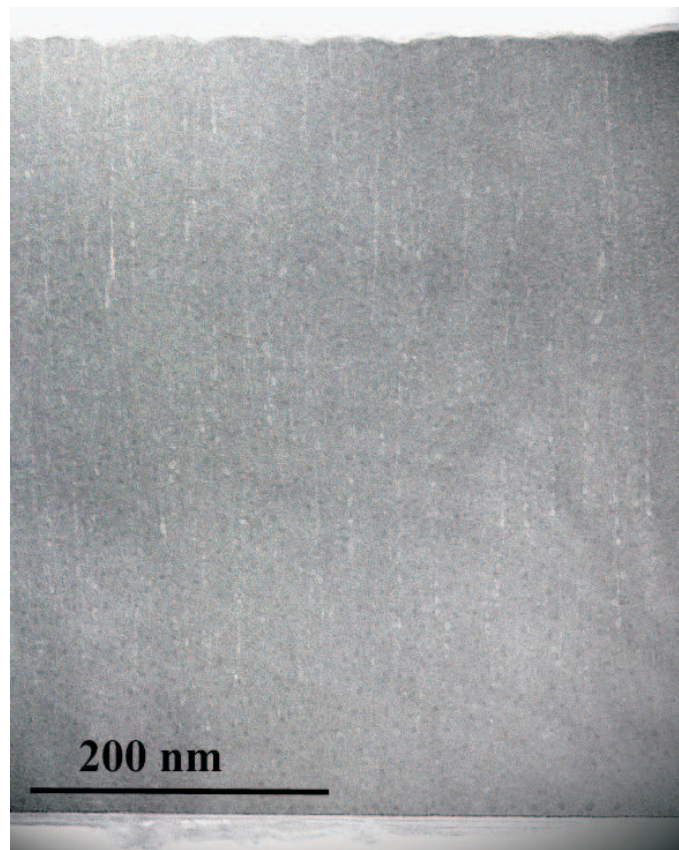


**Figure 3.6:** High resolution electron microscopy (HREM) image of protocrystalline *a*-SiGe:H material.

hydrogen content decreases with increasing  $T_s$ . Crossing the microcrystalline edge,  $f=85\%$ , the material shows as well a decrease in H content with increasing  $T_s$  at the Si-H peak. As a result, the material becomes more porous ( $n_0 \sim 2.90$  at  $T_s=180$  °C). At the lowest  $T_s$  (170 °C), the variation in dilution does not modify the amorphous structure of the material, showing for every  $f$  the same values for  $C_{H(Si-H)}$ ,  $C_{H(Si-H_2)}$  and  $C_{H(Ge-H)}$ . The low temperature on the surface may be limiting the diffusion of radicals and H; it is necessary to have an even higher  $H_2$  dilution.

Figure 3.6 shows a cross-sectional transmission electron microscopy (TEM) image of a material grown at the onset of microcrystallinity ( $f=75$  % and

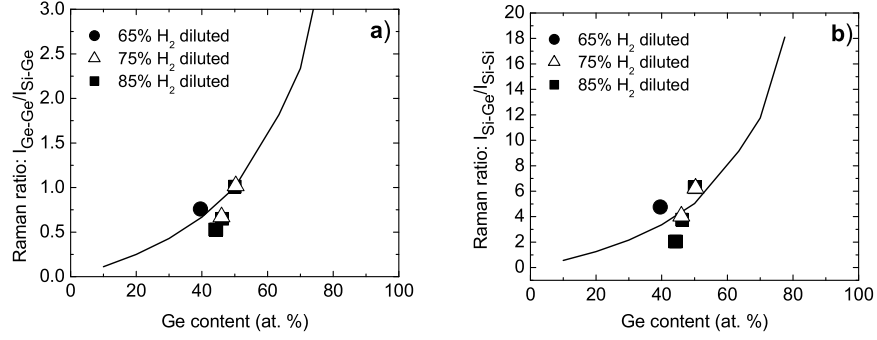


**Figure 3.7:** Raman ratios a)  $I_{Ge-Ge}/I_{Si-Ge}$  and b)  $I_{Si-Ge}/I_{Si-Si}$  as a function of Ge content for a-SiGe:H deposited under three different H<sub>2</sub> dilutions. The solid curve represents the ratios for random alloys. The error bars are inside the size of the points.

$T_s=180$  °C). Columnar void structures are observed along the thickness of the material. Hydrogens bonded at the internal surfaces of the voids are more tightly bound to the Si. This produces a shift of their stretching mode to higher frequencies ( $\sim 2080$   $\text{cm}^{-1}$ ), which contributes, together with the Si-H<sub>2</sub> stretching mode ( $\sim 2090$   $\text{cm}^{-1}$ ), to the vibrational mode at  $2080\text{-}2090$   $\text{cm}^{-1}$  observed in Fig. 3.4. The structural strain induced by Ge incorporated into the material is released through the creation of this columnar void structures.

With respect to the presence of homo- or heteronuclear bonds, Figure 3.7a shows the ratio  $I_{Ge-Ge}/I_{Si-Ge}$ , while Figure 3.7b shows the ratio  $I_{Si-Ge}/I_{Si-Si}$  as a function of the germanium concentration in the material. The vibrational modes measured by Raman spectroscopy are TO peaks of Si-Si, Si-Ge and Ge-Ge. Assuming a perfect random network, the amount of these bonds will be represented by the fractions  $(1-x)^2$ ,  $2(1-x)x$  and  $x^2$ , respectively, where  $x$  is the germanium concentration. Comparing the measured ratio ( $I_{Ge-Ge}/I_{Si-Ge}$  and  $I_{Si-Ge}/I_{Si-Si}$ ) with the predicted for random alloys ( $x/2(1-x)$  and  $2x/(1-x)$ ), an estimation of the presence of clusters can be found, knowing the Ge concentration ( $x$ ). The random alloy is calibrated by fitting the predicted bond density ratio,  $x/2(1-x)$  and  $2x/(1-x)$ , with the fractions  $I_{Ge-Ge}/I_{Si-Ge}$  and  $I_{Si-Ge}/I_{Si-Si}$  of a sample with very high concentration of Ge ( $\sim 70$  at.%). This material with high Ge concentration is expected to have a randomly mixed state [22]. The calibration of the ratio  $I_{Si-Ge}/I_{Si-Si}$  in the random distribution is less accurate than for the ratio  $I_{Ge-Ge}/I_{Si-Ge}$ , due to the small peak at TO mode for Si-Si in the

material with high germanium concentration used for the calibration.

The amorphous materials (made at low dilution conditions  $f \leq 75\%$  and low  $T_s$  or high  $H_2$  dilution and very low  $T_s$ ) exhibit a preferential formation of Ge-Ge bonds, and consequently formation of Ge clusters, as Figure 3.7a shows. Materials deposited under amorphous conditions show higher cluster formation (higher values of  $I_{Ge-Ge}/I_{Si-Ge}$  with respect to the random distribution). This indicates that the plasma chemistry conditions to grow amorphous material are unsuitable for promoting the formation of Si-Ge heterobonds. The presence of microcrystalline structure in the material promotes the formation of more ordered material. Small amounts of microcrystalline structure, obtained by depositing on the edge of the microcrystalline detection, are sufficient to reduce the cluster formation and promote the growth of more order regions. Materials with  $f=85\%$  and  $T_s$  over 170 °C present clear microcrystals, as Fig. 3.2a shows, and a ratio  $I_{Ge-Ge}/I_{Si-Ge}$  lower than the expected for random distribution. At the same time, the material deposited under  $f=75\%$  and  $T_s=190$  °C, exhibits the same higher amount of heterogeneous Si-Ge bonds as the more microcrystalline material. On the other hand, the material deposited under  $f=75\%$  and  $T_s=180$  °C presents the bond heterogeneity structure of an amorphous material with high Ge content and a random structure.

In Figure 3.6 it was shown a transmission electron microscopy image of the total thickness of the *a*-SiGe:H material previous to the microcrystalline formation (protocrystalline material). To study in more detail the structure of the protocrystalline material, high resolution electron microscopy (HREM) was used. Figure 3.8 shows the HREM images taken at different positions along the thickness of the film. The HREM image of the amorphous glass substrate (Figure 3.8a) shows an homogeneous structure typical for amorphous material. The fast-Fourier transform (FFT) of the image (inset figure) exhibits the diffuse halo ring confirming the amorphous structure of the glass substrate. An HREM image of the material deposited close to the substrate is shown in Figure 3.8b, while Figures 3.8c and 3.8d show images of the material close to the surface. The FFT of the image in Fig. 3.8b (inset figure) exhibits a ring slightly sharper than for pure amorphous material. The ring becomes sharper as the material grows, indicating a more ordered structure (inset Fig. 3.8c). This is also observed by selected-area diffraction pattern (inset Fig. 3.8d). We speculate that the improvement of the medium range order is due to the formation of small structures inside the material. These microstructures are visible in Fig. 3.8c and more clearly in Fig. 3.8d as darker regions with sizes of several tenths of Angstroms. The Raman spectrum of the protocrystalline material (at  $f=75\%$  and  $T_s=180$  °C in Fig. 3.2) shows that these microstructures are not in crystalline phase. At the same time, the microstruc-

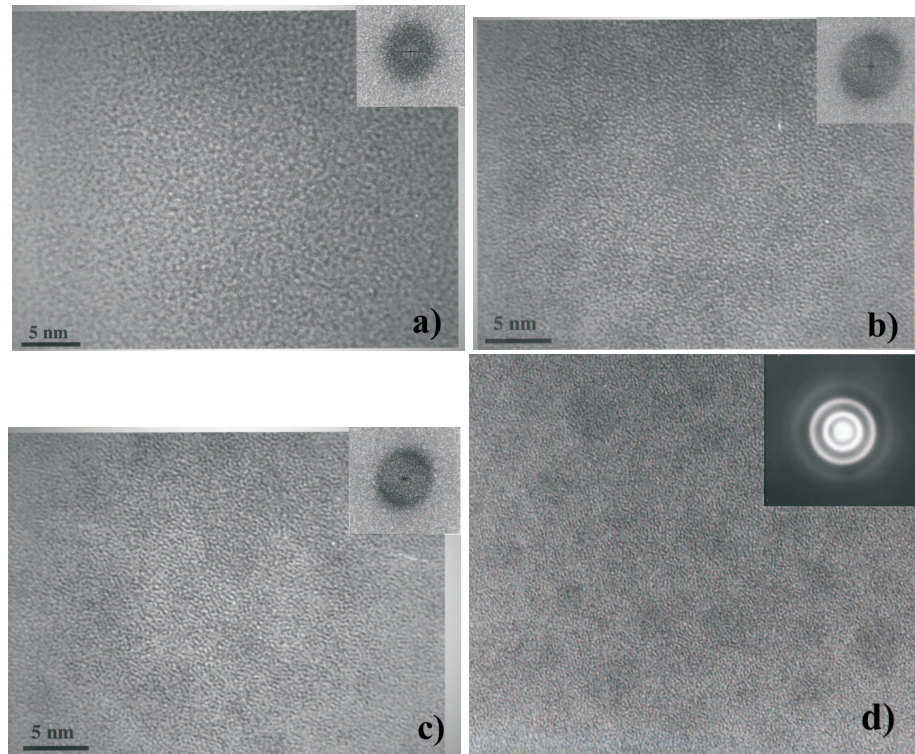


**Figure 3.8:** High resolution electron microscopy (HREM) images from different areas of the protocrystalline *a*-SiGe:H material. a) Area from glass substrate (amorphous); the inset shows the fast-Fourier transform (FFT). b) Area from material close to substrate; inset: FFT. c) Area from material close to surface; inset: FFT. d) Area from material close to the surface; the inset figure shows the selected-area diffraction pattern (SADP).

tures do not consist of only Ge atoms (which would be observed as Ge clustering formation) but as an heterogeneous mix of Ge and Si atoms. This is observed in Fig. 3.7a, where the measured  $I_{Ge-Ge}/I_{Si-Ge}$  ratio for the protocrystalline material has the same value as for a random alloy. Moreover, when the conditions lead to crystalline formation (see the change in material grown at  $f=75\%$  from  $T_s=180^\circ\text{C}$  to  $190^\circ\text{C}$  in Fig. 3.7a), the amount of Ge in the material decreases and the material shows a higher structural order (reduction of Ge-Ge cluster below the random level). Thus, the *a*-SiGe:H material starts growing amorphous with a high amount of Ge and changes to a material with a more ordered microstructure during growth. The crystallization begins at higher thickness (possibly at the site of

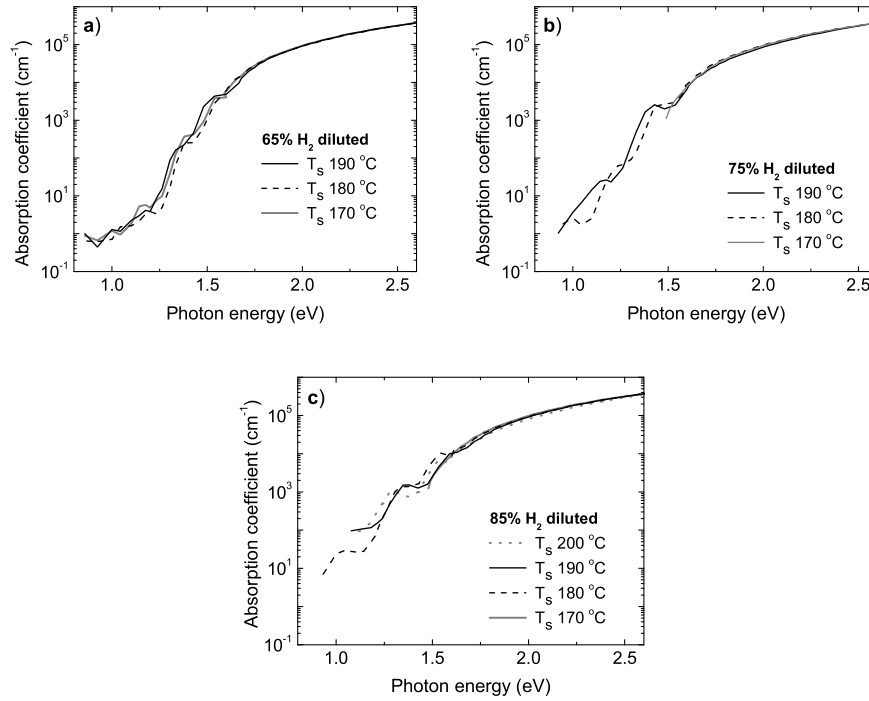


**Figure 3.9:** The absorption coefficient spectra measured by CPM versus  $T_s$  for  $a$ -SiGe:H deposited with several  $H_2$ -diluted ratio: a)  $f=65\%$ , b)  $f=75\%$  and c)  $f=85\%$ .

the ordered microstructures), reducing the amount of Ge in the material [71]. This has important consequences for the growth of  $\mu c$ -SiGe, as the structural strain in the network induced by high Ge concentration retards the crystalline nucleation.

### Optical characteristics

The optical band gap determined by Tauc's plot or by a cubic relation (as described in Section 2.2.1) remains constant for all series, amounting to 1.50-1.54 eV for the Tauc's gap and 1.20-1.25 eV for the cubic band gap.

Figures 3.9a to c show the absorption coefficient spectra for  $f=65\%$ , 75% and 85% respectively, as a function of the deposition temperature. The higher dilution series leads to a high Urbach energy (Fig. 3.10c), which could have been caused by a high concentration of Ge in the material or by microcrystals inserted in the

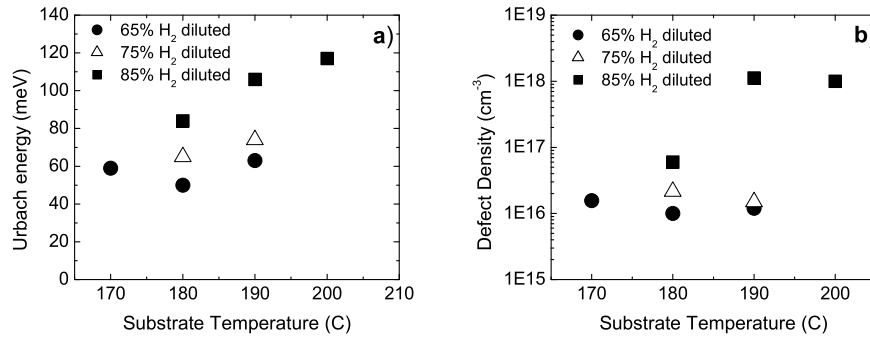


**Figure 3.10:** Urbach energy (a) and midgap density of states (b) as a function of  $T_s$  for three different H<sub>2</sub> dilutions.

amorphous phase. The Raman spectra (Fig. 3.2) and the concentration of Ge in the material measured by RBS (Fig. 3.5) were obtained to identify the cause of the exceptionally high Urbach energy values. The Ge concentration in the material for the higher dilution series is comparable with the other dilution series. On the other hand, the Raman spectra show crystalline structures that is not seen when the dilution is decreased (Fig. 3.2). This indicates that the microcrystals are the cause of the higher Urbach energy. For materials with a microcrystalline structure, the high defect density in the band gap contributes to the sub-band gap absorption. This excess absorption makes the Urbach energy higher, often over 100 meV [72]. If these microcrystals together with the presence of other phase, vary in a volume smaller than the volume under the illuminated area (10 mm<sup>2</sup> during the CPM measurement) the CPM measurement averages all the optical transitions within the illuminated volume. Thus, the high Urbach energy does not correspond with the conduction or valence band tail of the homogeneous alloy. A thinner layer of the material (to be applied in a solar cell) may show different properties than the more heterogeneous thick material, as the microcrystalline structure grows with the thickness of the film. For example, Xu et al. [73] observed for amorphous *a*-SiGe:H materials weak or no relation between material properties and solar cell performance. They observed that the decrease in the  $\mu\tau$  product with alloying is not reflected in the solar cell output, together with a lack of correlation between the defect density (that remains constant) and the fill factor (FF) (that decreases) with light soaking. The existence of a relation between the defect density and the FF is discussed in Chapter 4.

The Urbach energy and the midgap defect density measured by CPM are shown in Figures 3.10a and 3.10b, respectively. The value of both the parameters decreases when  $T_s$  is decreased, until the lower  $T_s$  limit of 170 °C. The Raman spectra of the materials that do not have clear crystalline peaks, correspond to a low Urbach energy and density of defects. They were deposited with  $f \leq 75\%$  at any of the  $T_s$  used. Higher dilution than 75% is clearly detrimental for the material, corresponding to higher defect density and Urbach tails. In Section 3.4.2 these results will be discussed in detail.

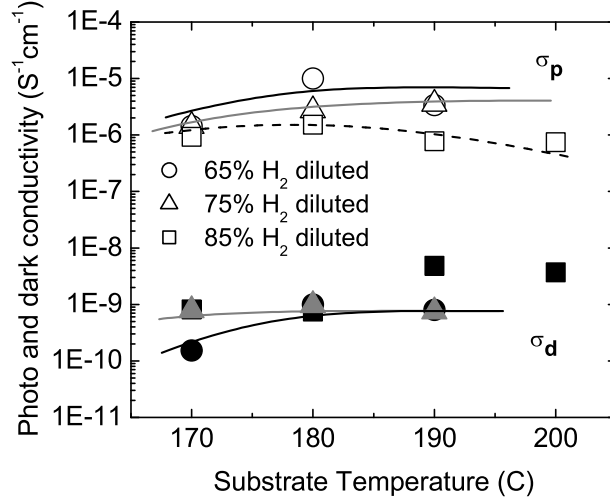
### Photo- and dark-conductivity

Figure 3.11 shows the photo- and dark-conductivity for the various dilution series as a function of  $T_s$ . The photo-conductivity increases as the  $H_2$  dilution decreases (the material becomes more amorphous). At the same time, the conductivity of the amorphous material exhibits a higher sensitivity to  $T_s$ , more significant for materials made at low dilution conditions. This is manifested in the drop of photo- and dark-conductivity at 170 °C. At this temperature all the dilution series produced are amorphous (Fig. 3.2), but only the most diluted series do not show a pronounced drop at 170 °C. An explanation could be found in the extra atomic H that is formed in the plasma at high dilution conditions. The bombardment of the atomic H to the surface imparts enough energy to the growing precursor on the surface to compensate the energy deficiency by decreasing  $T_s$ . At the same time, the atomic H eliminates excess of H from the *a*-SiGe:H film [74].

### 3.4.2 Discussion

The difference in the deposition rate between thin and thick samples is an issue normally overlooked but to which it is worthwhile to pay attention due to the plasma processes responsible for it. The growth model proposed by Winer does not explain properly this difference. According to this model (described in Section 3.2) the rf power (directly related with  $R_d$ ) and  $T_s$  control the material properties, while the plasma only provides the reactive species. If neither the rf power nor the  $T_s$  is changed and the material properties change with the deposition time, other processes than thermal diffusion of surface H are needed.

In accordance with the model proposed by Hata et al. [33] (see Section 3.2) the surface defects are buried into the bulk as the film grows. If the temperature and the annealing time are adequate, the bulk defects are annealed. The annealing time depends on the kind of defects created at the surface. Moreover, when the dilution is changed, the conditions in the plasma change at the same time, specially through the amount of atomic H probing the surface. As a result, the local



**Figure 3.11:** Photo- ( $\sigma_p$ ) and dark- ( $\sigma_d$ ) conductivity of a-SiGe:H deposited at three different flows as a function of  $T_s$ .

bonding configurations at the surface are significantly influenced by the plasma conditions. Then, the surface defect density depends on the plasma conditions ( $H_2$  dilution). For very high dilution conditions,  $f=85\%$ , the amount of atomic H bombarding the growing surface promotes a change in phase (creation of crystalline structures). The amount of surface defect density will be higher than that for lower  $H_2$  dilutions. If the deposition time is the same for materials created with different dilutions and long enough to cause observable differences, the material with higher dilutions will have more buried defects. More H is attached at the boundaries of the crystalline structure, resulting in the higher  $R^*$  observed in Fig. 3.3d and consequently an increase in  $R_d$ , not expected with increasing dilution. Porous materials exhibit higher thickness than more compact materials (for the same deposition time), which is observed as a higher deposition rate. The material exhibits lower density, as defined through  $n_0$  (Fig. 3.1d).

The results described in the previous section present the interesting characteristics of the materials made under different hydrogen dilutions of the plasma gasses and for different deposition temperatures. These are the principal parameters in the hydrogen density of states model (HDOS) proposed by Street [11], which makes it attractive to test the model for explaining the previous results.

According to this model the optimum conditions for growing *a*-Si:H material strongly depend on the hydrogen chemical potential ( $\mu_H$ ) in the plasma. The principal dependence of  $\mu_H$  lies on the concentration of H in the plasma (dilution) and in the temperature on the growing surface ( $T_s$ ). The model has succeeded in explaining the deposition of fully amorphous *a*-SiGe:H [75]. In this section, the model for material at the edge of the microcrystalline growth at low deposition temperatures will be discussed.

The model considers that the bonding structure in the film is to a large extent controlled by  $\mu_H$  in the plasma. The H chemically reacts with the bonds at and beneath the growing surface, altering the distribution of weak and broken bonds. At high enough temperatures the structure will reach an equilibrium state defined by the match of  $\mu_H$  in the plasma and in the film. The process is mediated by the interchange of H between the plasma and the surface as well as by the diffusion of H on the surface, promoting changes in the bonding configuration as defined in the weak bond model [76] (Eq. 4.1). The equilibrium is reached locally by minimizing the free energy of small volumes constrained by the long-range disorder in the amorphous network. When the equilibrium is reached, the structure will present the lowest weak bond and dangling bond density, limited by the amorphous network.

Figures 3.12b, c and d show the HDOS distribution,  $N_H(E)$ , as a function of the H bonding energy relative to the vacuum level,  $E_{HV}$ . Hydrogen is present in Si-H and Ge-H bonds, below  $\mu_H$ , represented by two broad bands indicating the different environment around the H bond. The Ge-H bond is weaker than the Si-H bond, so the energy needed to make the H mobile is smaller.  $E_M$  represents the minimum energy at which the H can diffuse freely, and is estimated to be 0.5 to 1 eV below  $E_{HV}$ . The energy difference between  $E_M$  and  $\mu_H$  corresponds to the activation energy for H diffusion (1.5 eV). Above  $\mu_H$ , the states are unoccupied and they include weak and stronger Si-Si bonds where the H can be inserted with different energies. The redistribution energy,  $E_R$ , is defined as the minimum energy at which the atoms can be redistributed in a time  $t_s$  by interacting with H, before they are definitely included in the film structure. The position of  $\mu_H$  in the plasma and  $E_R$  are defined by

$$E_{HV} - \mu_H = kT \ln \left( \frac{N_{H0}}{N_{HP}} \right) \quad (3.20)$$

$$E_M - E_R = kT \ln(\omega_0 t_s) \quad (3.21)$$

where  $N_{HP}$  is the H concentration in the plasma,  $N_{H0}$  is the inverse of the H quantum volume (the effective density of states,  $3 \times 10^{24} \text{ cm}^{-3}$ ),  $t_s$  is the deposition time and  $\omega_0 = 10^{13} \text{ s}^{-1}$ . The limiting step in the growth process is the

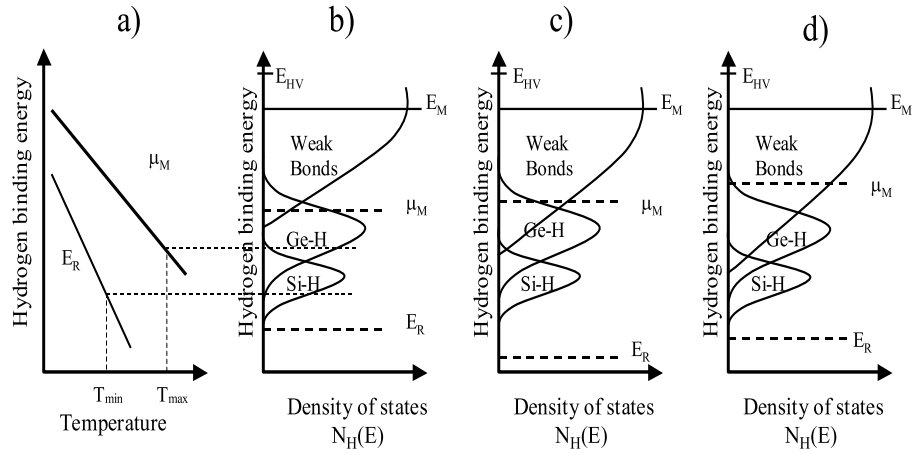


**Figure 3.12:** Hydrogen density of states distribution,  $N_H(E)$ , as a function of the H bonding energy correlated with a dilution of b) 65%, c) 75% and d) 85%, at  $T_s=190$  °C. A) shows the temperature dependence of  $\mu_H$  and  $E_R$

excitation of H to a mobile state. The most ordered structure is obtained when  $E_R$  lies deep below the Si-H band (longer  $t_s$ ). In other case the growth process will be kinetically limited by the H diffusion, broadening the weak bond distribution.

Figures 3.12b, c and d show the HDOS distribution which will be correlated with the dilution,  $f$ , of 65%, 75% and 85%, respectively, at  $T_s=190$  °C. Figure 3.12a together with 3.12b, 3.12c or 3.12d show the temperature dependence of  $\mu_H$  and  $E_R$  for the different HDOS. The  $T_{min}$  and  $T_{max}$  define the limits at which a low temperature shifts  $E_R$  inside the Si-H band and freezing the H in the Si-H bonds, unable to restructure. This case would produce a high density of weak bonds. The higher temperature limit is reached when  $\mu_H$  moves deeper into the Si-H band. In this case all the Ge-H bonds would be unoccupied together with many of the Si-H bonds, growing a highly defective material.

The material diluted at  $f=65\%$  presents a constant deposition rate, superior to the most diluted series. In these conditions the relaxation time during growth will be smaller than for series with  $f=75\%$  and  $85\%$ . The redistribution energy is

shifted to higher energies, but it is still low enough to allow for structural relaxation. The high H concentration in the material together with a low microstructure parameter (Fig. 3.3d) suggests that the greatest part of the dangling bonds would be passivated and the weak bonds relaxed. The weak bond band would be narrow with a small overlap with the Ge-H bond band. At the same time,  $\mu_H$  would lie above the Ge-H bond band ensuring that the Ge bonds are occupied with H (Fig. 3.12b). This is observed in the low Urbach energy and defect density (Fig. 3.10). Decreasing  $T_s$  to 180°C moves  $\mu_H$  closer to  $E_M$ , helping the redistribution of atomic H that needs lower energy to become mobile. The probability of dangling bond formation and the amount of weak bonds decreases. If  $T_s$  is decreased to 170 °C the model predicts a further improvement in the structure through the shift of  $\mu_H$  to  $E_M$ . But the diffusion of H to deeper states is critically reduced. This implies that the time available for redistribution processes decreases generating more weak bonds. This time the Urbach energy increases oppositely with  $T_s$  ( $E_R$  is shifted closer to the Si-H band).

At  $f=75\%$  the amount of atomic H in the plasma increases, providing the plasma with more energetic bombardment over the surface. The first bonds to feel this extra energy are the weaker bonds (Si-H<sub>2</sub> ~2.8 eV compared with Ge-H~3 eV and Si-H~3.4 eV). Figure 3.13 shows the ratio of Ge-H bonds in the material with respect to the weakest bonds (Si-H<sub>2</sub> and Ge-H). Together with Fig. 3.4, where the H content in different bond configurations is shown, one can observe how at these dilution conditions the Si-H<sub>2</sub> is preferentially removed from the material, leading to low microstructure fraction (Fig. 3.3d). On the other hand a larger extend of H on the subsurface may form small microcrystals, creating at the boundaries inhomogeneities and weak Si-H bonds. The weak bond band consequently will have a wider overlapping with the Ge-H band (Fig. 3.12c). The beneficial effect on  $\mu_H$  due to the higher dilution partially compensates the increase in defect density. The material exhibits slightly more pronounced Urbach energy and very similar defect density. A decrease in  $T_s$  decreases the deposition rate (shifting  $E_R$  downward) creating less disorder and lower Urbach energy (Fig. 3.10). At the same time, the H desorbs less from the surface, growing a material with higher H content (Fig. 3.5). A lower temperature,  $T_s=170$  °C, has the same effect as for the previous series.

When the dilution is increased to  $f=85\%$ , the formation of microcrystals is clearly observed by Raman spectroscopy (Fig. 3.2). The shift in the Si-H IR peak is correlated too with the presence of microcrystals [69]. The boundaries at the microcrystals and other microstructures will increase the density of weak bonds (broader weak bond band in Fig. 3.12d). The high amount of Si-H<sub>2</sub> observed could be located at these boundaries, pasivating the bonds created by the

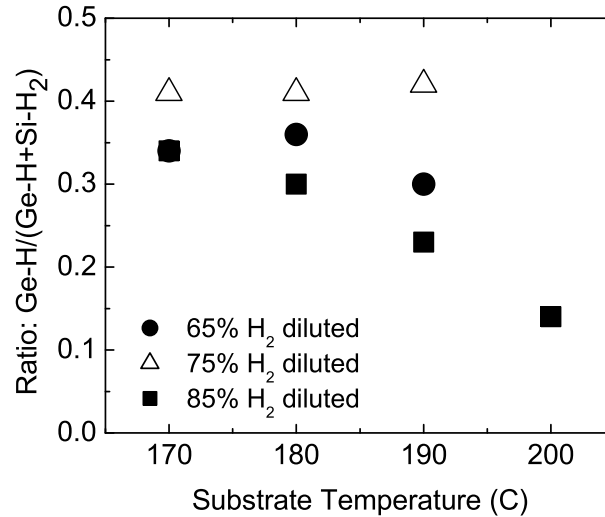


**Figure 3.13:** Ratio of Ge-H bonds to Ge-H/Si-H<sub>2</sub> as a function of  $T_s$  of *a*-SiGe:H deposited under three different H<sub>2</sub> dilution ratios.

mismatch of the amorphous and crystal networks. The broad weak bond band extensively overlaps the Ge-H and may be even the Si-H band. This would generate more Ge and Si dangling bonds than in the previous cases, which could be interesting to verify by ESR. In summary, the Urbach energy sharply increases at the same time as the density of defects (Fig. 3.10). Decreasing  $T_s$  avoids the desorption of H from the surface (Ge-H bonds), increasing the final amount of H incorporated in the material specially in the bond configuration Ge-H (Fig. 3.13) or as voids or clusters (Fig. 3.3d). The deposition rate decreases with decreasing  $T_s$ , which shifts  $E_R$  downwards. This implies that the time available for structural changes increases reducing the weak bonds band. This is observed in a reduction of the Urbach energy and the defect density with decreasing  $T_s$  (Fig. 3.10). Under  $T_s=170$  °C, the material behaves the same as for the previous dilutions. At this temperature the depth at which the H can promote structural changes kinetically limits the system, and even a higher dilution than  $f=85\%$  may be necessary to help the diffusion of H. In this case, the increase in dilution should be accompanied by a decrease in the deposition rate (by the higher dilution itself or through the rf power) to provide time for avoiding the insertion of higher radicals.

By modifying the thickness of the film and the  $T_s$  we have observed a phase transition in the  $\alpha$ -SiGe:H material. The influence of the hydrogen dilution and the substrate temperature on this process has been studied. As a result, the deposition parameters to obtain a material before the formation of microcrystals (protocrystalline material) were determined for different deposition conditions. The material which presents clear macrocrystalline structure (observed from Raman spectroscopy), exhibits an improvement in the medium range order with respect to amorphous material (Fig. 3.7). We speculate that the protocrystalline material exhibits similar improvement. This will ameliorate the stability of the material, fundamental for the stability of the solar cell (see Chapter 5).

### 3.5 Results in deposition of $\alpha$ -SiGe:H at high deposition rates

Several works have proposed the advantage of replacing  $\text{SiH}_4$  with  $\text{Si}_2\text{H}_6$  in order to provide the plasma with species dissociating at closer rate to  $\text{GeH}_4$ . Lundszein et al. [65] have obtained a considerable improvement in microstructure factor and Urbach tail in this way with very high  $\text{H}_2$  dilution. They suggested that once in this stage, the deposition rate ( $R_d$ ) could be easily increased through the rf power without adverse effect on the material properties. Sakata et al. [66] have observed for materials deposited with  $\alpha$ -Si:H that when depositing at high deposition rates, the use of  $\text{SiH}_4$  gas results in material with higher structural disorder than when  $\text{Si}_2\text{H}_6$  is used as feed gas.

The work presented below have a goal of depositing  $\alpha$ -SiGe:H material at high deposition rate and low temperatures. We present here a series of films made with  $\text{Si}_2\text{H}_6+\text{GeH}_4$  where the band gap was kept constant at  $1.52\pm 0.02$  eV (Tauc's band gap). The  $\text{H}_2$  dilution was varied from  $f=40\%$  to  $150\%$  by changing the total flow of  $\text{Si}_2\text{H}_6+\text{GeH}_4$  and keeping  $\text{H}_2$  flow constant at 185 sccm (the maximum permitted by the system).

All the materials obtained with  $\text{Si}_2\text{H}_6$  gas contain a higher concentration of hydrogen than for  $\text{SiH}_4$  as source gas (for the same band gap). The Ge concentration is also appreciably higher. The trends obtained show a general increase in  $R_d$  when the dilution is decreased, which comes along with a general deterioration of the photo- and dark-conductivity, Urbach energy and diffusion length.

Figure 3.14a, b, c and d show the H and Ge content, the photo- and dark-conductivity, the Urbach energy and the microstructure factor as a function of the deposition rate and for two different  $T_s$  (180 °C and 200 °C).

It has been suggested that a high amount of Ge in the material inhibits the mi-

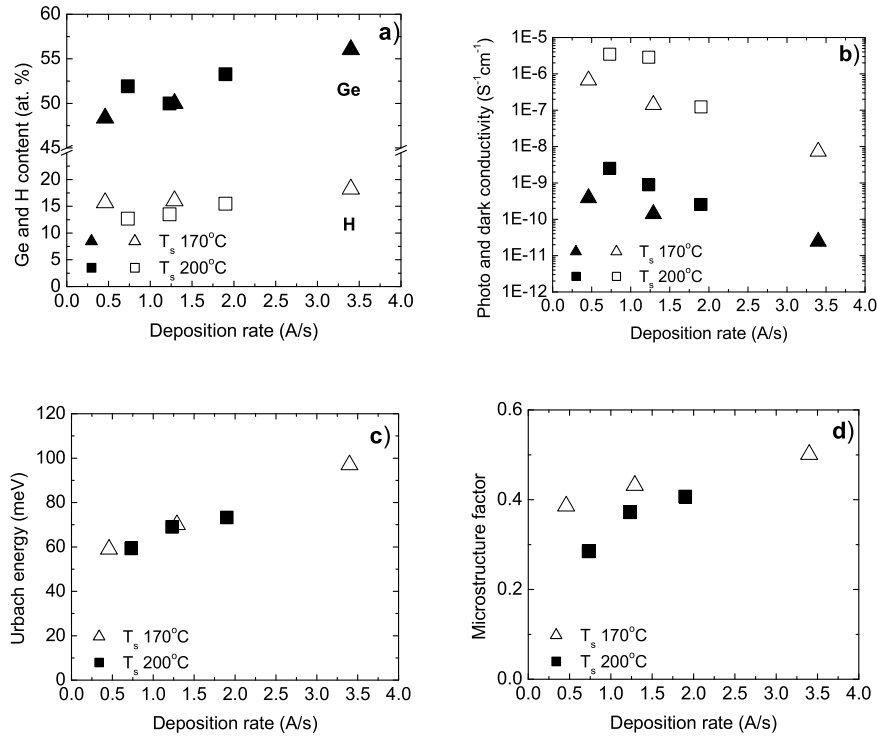


**Figure 3.14:** Germanium and hydrogen content (a), photo- ( $\sigma_p$ ) and dark- ( $\sigma_d$ ) conductivity (b), Urbach energy (c) and microstructure factor (d) for two series of *a*-SiGe:H material deposited with Si<sub>2</sub>H<sub>6</sub>+GeH<sub>4</sub> at T<sub>s</sub> of 170 °C and 200 °C, as a function of the deposition rate. The variation in deposition rate is obtained by changing the Si<sub>2</sub>H<sub>6</sub>+GeH<sub>4</sub> flow.

microcrystallinity formation due to the introduction of extra structural strain in the network [77]. On the other hand, the interaction of H within the material is expected to produce structural relaxation, promoting the microcrystalline formation. But when H is introduced as higher hydrides, the effect is the opposite, retarding the microcrystalline formation.

As shown in Figures 3.14a, the amount of Ge and H is higher for the case of Si<sub>2</sub>H<sub>6</sub> than in the case of SiH<sub>4</sub> (Fig. 3.5). At the same time, the microstructure factor exhibits a high presence of higher hydrides (Fig. 3.14d). Therefore the material growth with Si<sub>2</sub>H<sub>6</sub> as source gas is amorphous, even at the highest dilution

(lowest  $R_d$ ), confirmed by Raman spectroscopy measurements. An increase in  $T_s$  helps to decrease the presence of high hydrides but not enough to create nucleation. For very low dilution (high  $R_d$ ), the higher  $T_s$  helps to grow a more compact material, improving the surface diffusion of radicals and the H elimination from the surface and the bulk [78].

For the same dilution as in the case of  $\text{SiH}_4+\text{GeH}_4$ , the material deposited with  $\text{Si}_2\text{H}_6+\text{GeH}_4$  as source gasses (material with  $R_d=1.2 \text{ \AA/s}$  in Fig. 3.14), exhibits a 2 times higher deposition rate. The Urbach energy and the photo- and dark-conductivity show for both the cases very close values, and the defect density is one order of magnitude higher for the case of disilane compared to silane. But the most important drawback is the instability of this material to illumination. In Section 5.4 a degradation study of the protocrystalline material deposited with  $\text{SiH}_4+\text{GeH}_4$  is compared with two amorphous materials deposited with  $\text{Si}_2\text{H}_6+\text{GeH}_4$  at the same and two times higher  $R_d$  and  $T_s$  of  $200 \text{ }^\circ\text{C}$ . These are the materials deposited with  $\text{Si}_2\text{H}_6+\text{GeH}_4$  with the best properties.

In summary, the change in plasma chemistry when  $\text{SiH}_4$  is replaced with  $\text{Si}_2\text{H}_6$  as feed gas seems to be responsible for the significant increase in insertion of higher hydrides for the same dilution conditions. Under higher dilution conditions obtained at low  $\text{Si}_2\text{H}_6+\text{GeH}_4$  flow, a possible depletion of both gasses could be contributing to the deposition of higher radicals, with detrimental influence of the Urbach energy and defect density. To improve the formation of microcrystalline structure, the concentration of higher hydrides must be reduced. This can be achieved through a higher  $\text{H}_2$  dilution in those cases where the depletion of  $\text{Si}_2\text{H}_6$  and  $\text{GeH}_4$  gasses is at the same time avoided. Other possibility is through strong ion bombardment resulting in a release the strain in the network by H elimination. The use of  $\text{Si}_2\text{H}_6$  as a source gas towards higher deposition rates must go together with the growth of protocrystalline  $\alpha\text{-SiGe:H}$  material which exhibits high stability against the Staebler-Wronski effect. As mentioned before, higher  $\text{H}_2$  flows (not reachable in this study) are necessary when  $\text{Si}_2\text{H}_6$  is used as a source gas.

### 3.6 Conclusions

The influence of the deposition temperature and  $\text{H}_2$  dilution on the formation of microcrystalline phase in  $\alpha\text{-SiGe:H}$  material has been studied in detail. The  $\text{H}_2$  dilution was varied along with the  $T_s$  to promote the formation of microcrystalline phase at low deposition temperature ( $T_s=180 \text{ }^\circ\text{C}$ ), with the aim of depositing  $\alpha\text{-SiGe:H}$  at the edge of this transition. The material obtained exhibits a reduction in the amount of Ge-Ge cluster to values lower than amorphous material, pro-

**Table 3.1:** Material properties of fully *a*-SiGe:H, amorphous before crystalline formation (protocrystalline), deposited with SiH<sub>4</sub>+GeH<sub>4</sub> at low T<sub>s</sub>, and *a*-SiGe:H deposited with Si<sub>2</sub>H<sub>6</sub>+GeH<sub>4</sub>.

Material property	Amorphous SiH <sub>4</sub> +GeH <sub>4</sub>	Proto SiH <sub>4</sub> +GeH <sub>4</sub>	Amorphous Si <sub>2</sub> H <sub>6</sub> +GeH <sub>4</sub>
T <sub>s</sub> (°C)	180	180	200
Dilution ( <i>f</i> )	65 %	75 %	75 %
Deposition rate (Å/s)	0.6	0.7	1.2
Tauc band gap (eV)	1.55	1.52	1.52
Activation energy (eV)	0.73	0.7	.74
H content (at.%)	12.5	13.4	13.5
Ge content (at.%)	40	50	50
Microstructure R*	0.27	0.21	0.37
Urbach energy (meV)	50	65	70
CPM defect density (cm <sup>-3</sup> )	1 × 10 <sup>16</sup>	2 × 10 <sup>16</sup>	1 × 10 <sup>16</sup>
Ambipolar diffusion length (nm)	95	94	96
Dark-conductivity (S/cm)	1 × 10 <sup>-9</sup>	9.7 × 10 <sup>-10</sup>	8.9 × 10 <sup>-10</sup>
Photo-conductivity (S/cm)	1 × 10 <sup>-5</sup>	2.7 × 10 <sup>-6</sup>	2.9 × 10 <sup>-6</sup>
Photosensitivity <i>S</i>	1 × 10 <sup>4</sup>	2.8 × 10 <sup>3</sup>	3.3 × 10 <sup>3</sup>

moting the growth of more ordered material. We speculate that the improvement in the medium range order is generated by heterogeneous microstructures of Si and Ge atoms with more ordered amorphous structure than the *a*-SiGe:H network where they are immersed. Below a temperature of 180 °C a steep transition is observed where, independently of the dilution ratio, the material grows amorphous. The HDOS model was invoked to describe the results. At the same time, conditions for higher deposition rate were investigated. Replacing SiH<sub>4</sub> with Si<sub>2</sub>H<sub>6</sub> as a feed gas, the deposition rate was doubled. The different radical formation in the plasma degenerates in an amorphous material with higher H content. On the other hand, in high deposition rate conditions the deposition temperature must be increased to promote diffusion of radicals at the surface.

From this can be concluded that the deposition of protocrystalline *a*-SiGe:H is possible at low temperatures over a minimum T<sub>s</sub>. At the same time, higher deposition rate conditions obtained with Si<sub>2</sub>H<sub>6</sub> are incompatible with the growth of protocrystalline *a*-SiGe:H at low substrate temperature. Table 3.1 shows the summary of the characteristic parameters for three different materials: an fully amorphous *a*-SiGe:H material obtained at low T<sub>s</sub>; an *a*-SiGe:H material deposited below the crystalline formation (protocrystalline material) and a fully amorphous

$\alpha$ -SiGe:H material deposited with  $\text{Si}_2\text{H}_6 + \text{GeH}_4$ .

The stability of those materials against the Staebler-Wronski effect as well as their influence when implemented in a solar cell structure is studied in Chapter 5.

## 4 Computer-aided solar cell improvement

---

### 4.1 Introduction

To simulate accurately the electrical and optical properties of *a*-Si:H devices and its alloys, a precise description of the distribution of the density of states as a function of the energy is fundamental. Besides of fitting experimental results, computer simulations can open new development directions if implementing the appropriate model. The complexity of the processes in solar cells makes attractive the use of computational techniques. And it is for band gap engineering where these techniques are more powerful. Thus, in a tandem solar cell structure the characteristics of both, the top and the bottom, cell influence the global output of the double-junction. The *a*-SiGe:H alloy, constituent of the bottom cell, shows poorer transport properties than *a*-Si:H, due to the high defect concentration. Guha et al. [79] proposed the design of the band gap profile of this single junction in order to help the hole transport reducing the recombination losses. Since then several profiles have come up to improve *a*-SiGe:H solar cells [80,81].

In this chapter two different models describing the defect states density in the mid gap are compared with experimental characterization. The accuracy of the models is tested on the predictions they suggested as well as on the exactitude of the fitted characteristics. With the defect pool model [82,83] as the most reliable model, the band gap profile for the active layer of the *a*-SiGe:H single junction cell is investigated. Experimental results following computer predictions are presented and discussed.

### 4.2 Modelling. D-AMPS computer simulation program

#### 4.2.1 AMPS computer code

The computer simulations presented in this study are based on the computer code AMPS (Analysis of Microelectronic and Photonic Structures) developed at The Pennsylvania State University [84,85]. AMPS is a very general one-dimensional computer program for simulating transport physics in solid-state devices. The structure of these devices can be composed of crystalline, polycrystalline or amorphous material, or any combination of them. AMPS code was further developed

to D-AMPS, which includes a more sophisticated description of mid gap states through two models: a uniform density model (UDM) defined by an amphoteric distribution of states [86], or the defect pool model (DPM) [82,83]. Both the models are briefly described in the next section. D-AMPS also includes scattering at rough interfaces [87].

The physics of device transport can be described by three governing equations: Poisson's equation, the continuity equation for free holes and the continuity equation for free electrons. Each of these equations has two associated boundary conditions. The transport characteristics are determined by solving these three coupled non-linear differential equations .

In AMPS, these three coupled equations, along with the appropriate boundary conditions, are solved simultaneously to obtain a set of three unknown state variables at each point in the device: the electrostatic potential, the hole quasi-Fermi level, and the electron quasi-Fermi level. From these three state variables, the carrier concentrations, fields, currents, etc. can then be computed. To determine these state variables, the method of finite differences and the Newton-Raphson technique are incorporated. The Newton-Raphson Method iteratively finds the root of a function or roots of a set of functions if given an adequate initial guess for these roots. In AMPS, the one-dimensional device that is analyzed is divided into segments by a mesh of grid points, the number of which is defined by the user. The three sets of unknown variables are then solved for each particular grid point. AMPS allows the mesh to have variable grid spacing at the discretion of the user. Once these three state variables are obtained as a function of position, the band edges, electric field, trapped charge, carrier populations, current densities, recombination profiles, and any other transport information may be obtained.

#### 4.2.2 Set of device models implemented in D-AMPS

The optical model to simulate rough interfaces implemented in D-AMPS is still under development. For this study the light was supposed incoherent, so no interference phenomena were present. On the other hand, the roughness at the interfaces was described by a random distribution of angles around a value defined for each interface, measured with respect to the flat surface of the glass. The roughness was reduced at each interface from  $77.5^\circ$  at the TCO/p interface to  $70^\circ$  at the n/metal interface due to the thickness of the cell.

The most important improvement in the computer code AMPS is the implementation of the defect pool model to simulate the density of mid gap states. Section 4.3.1 deals in detail with this issue. In this section two mid gap state models are described: the uniform density model (UDM) and the defect pool model (DPM).

### Uniform density model (UDM)

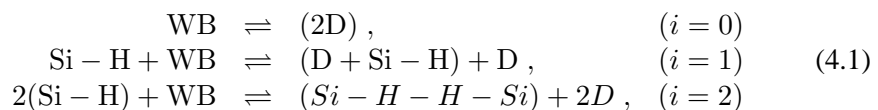
The amphoteric states model [86] approximates the defect density by two bands with Gaussian distributions, a donor-like state ( $DB^{+/0}$ ) and an acceptor-like state ( $DB^{0/-}$ ). The energy levels inside the band gap are  $E^{+/0}$  and  $E^{0/-}$  respectively. These two bands arise from the two transition levels of a dangling bond. They are separated from each other by a correlation energy ( $U$ ). The correlation energy is the energy necessary to add a second electron to a neutral dangling bond.

The occupation function is derived from statistical thermodynamics. The defect energy distribution of the three charge states of an amphoteric state (non-occupied (+), single-occupied (0) or double-occupied (-)) is determined by the occupation function, leading to  $D^+$ ,  $D^0$  and  $D^-$  charge states and the defect energy distribution, described as Gaussian.

In this study the peak energies of these Gaussian distributions are located in the lower half of the band gap ( $D^+$ ), close to the Fermi level of the intrinsic material ( $D^0$ ) and in the upper half of the band gap ( $D^-$ ). In a-Si:H buffer and doped layers the ratio of charged to neutral defects of 4:1 was adopted [82], and 6:1 in the a-SiGe:H lowest band gap intrinsic layer [80] and equal to ratios between 4:1 and 6:1 in band gap graded layers. The correlation energy  $U$  was always assumed equal to 0.2 eV. The peaks of the Gaussian were spaced apart in energy by 0.3 eV along the whole device. The separation between the non-occupied  $D^+$  peak and the double occupied  $D^-$  peak, was therefore adopted equal to 0.4 eV and independent of the band gap.

### Defect pool model (DPM)

The UDM does not take into account the origin of the states distribution in the band gap. It is capable of determining the states distribution with the drawback of not having a physical background. The defect pool model [82,83] defines the defect states distribution in the band gap starting from the initial formation of the dangling bonds. The principle of the DPM is the formation of defects in accordance with the weak bond-dangling bond conversion model of Stutzmann [76]. The weak bond (WB) breaking model describes the dangling bond formation by breaking weak Si-Si bonds in one or more of the following reactions, where the only difference is the number of Si-H bonds participating in the process (represented by  $i$ ):



Smith and Wagner [88] found that the distribution of weak bond energies is associated with the density of states in the valence band tail, exponentially distributed in energy. This permits the evaluation of the distribution of formation energy of dangling bonds from the valence band and the defect density distribution. On the other hand, when a weak bond breaks it creates two defects. It is accepted that the H atoms mediate the defect distribution by separating these dangling bonds. Finally, the Fermi energy determines the defect distribution through the occupation of the charge states. The DPM describes the equilibrium defect density distribution as the minimum in entropy of Eq. 4.1, directly influenced by the Fermi energy [82,83]. The importance of the DPM is more clear seen in a solar cell structure where the Fermi level changes through the entire intrinsic layer (see Section 4.3.1).

### 4.2.3 Sensitivity study of solar cells parameters for D-AMPS simulation program

The sensitivity study was performed on a solar cell consisting of p- and n-type doped layers, an *a*-SiGe:H intrinsic layer with no band gap grading profile and buffers between the doped layers and the intrinsic layer. The sensitivity of the light (AM1.5) J-V characteristics of a solar cell to the simulation model has been studied through several model parameters. Each parameter is changed one at a time. The influence of one model parameter,  $Y$ , on one light J-V characteristic,  $X$ , is determined as the variation of  $X$  with the parameter  $Y$ ,

$$S = \frac{dX}{dY} \times \frac{Y_{max} - Y_{min}}{X_r} \quad (4.2)$$

normalised to the total range where the parameter  $Y$  changes and to the reference value of the characteristic,  $X_r$ . In Equation 4.2  $Y_{max}$  and  $Y_{min}$  are the maximum and minimum values of the parameter  $Y$ , respectively, and  $S$  denotes the relative sensitivity of the characteristic  $X$  to the parameter  $Y$ .

The model parameters selected for the sensitivity study were: the band gap of the intrinsic layer ( $E_g$ ); the energy defining the slope of the valence band ( $E_{VO}$ ) as well as the conduction band ( $E_{CO}$ ); the capture cross section of charged ( $\sigma_{+/-}$ ) and neutral ( $\sigma_0$ ) states; the position of the defect pool ( $E_P$ ) and the width of the defect pool ( $\sigma_P$ ). Table 4.1 shows the dependence of the light J-V characteristics on these parameters. The range where the parameters were varied is also included.

In Table 4.1, the numbers from 0 to 5 indicate the ranking of the relative sensitivity of the characteristic  $X$  to the parameter  $Y$ , with 0 meaning no influence.

**Table 4.1:** Sensitivity of the light J-V characteristics of a *a*-SiGe:H solar cell to some selected parameters.

Parameter	Unit	Values	$V_{oc}$ (V)	FF	$J_{sc}$ (mA/cm <sup>2</sup> )	$\eta$ (%)
$E_g$	eV	1.1 – 1.8	5 <sup>-</sup> – 5 <sup>+</sup>	5 <sup>-</sup> – 5 <sup>+</sup>	3 <sup>-</sup> – 3 <sup>+</sup>	5 <sup>-</sup> – 5 <sup>+</sup>
Offset		in CB - in VB	1 <sup>+</sup> – 1 <sup>-</sup>	4 <sup>+</sup> – 4 <sup>-</sup>	1 <sup>+</sup> – 1 <sup>-</sup>	3 <sup>+</sup> – 3 <sup>-</sup>
$E_{VO}$	eV	0.03 – 0.06	3 <sup>+</sup> – 3 <sup>-</sup>	4 <sup>+</sup> – 4 <sup>-</sup>	2 <sup>+</sup> – 2 <sup>-</sup>	4 <sup>+</sup> – 4 <sup>-</sup>
$E_{CO}$	eV	0.01 – 0.04	0	0	0	0
$E_P$	eV	0.95 – 1.02	1 <sup>-</sup> – 1 <sup>+</sup>	2 <sup>-</sup> – 2 <sup>+</sup>	0	3 <sup>-</sup> – 3 <sup>+</sup>
$\sigma_P$	eV	0.12 – 0.18	3 <sup>+</sup> – 3 <sup>-</sup>	3 <sup>+</sup> – 3 <sup>-</sup>	1 <sup>+</sup> – 1 <sup>-</sup>	4 <sup>+</sup> – 4 <sup>-</sup>
$\sigma_{+/-}$	10 <sup>-15</sup> cm <sup>2</sup>	1 – 10	1 <sup>+</sup> – 1 <sup>-</sup>	1 <sup>+</sup> – 1 <sup>-</sup>	0	1 <sup>+</sup> – 1 <sup>-</sup>
$\sigma_0$	10 <sup>-16</sup> cm <sup>2</sup>	1 – 10	1 <sup>+</sup> – 1 <sup>-</sup>	1 <sup>+</sup> – 1 <sup>-</sup>	0	1 <sup>+</sup> – 1 <sup>-</sup>

The symbols "+" or "-" indicate if the change in the parameter *Y* increases or decreases the characteristic *X*, respectively.

The band gap of the intrinsic layer with respect to the doped layers generates a mismatch in the valence and conduction band between these layers, known as band offset. The offset creates a barrier for electron and hole transport. The distribution of the band offsets between the valence and the conduction band is not certain [55,89], but for simulation purpose it can be studied modifying the electron affinity. When the electron affinity of the layers is the same, the valence bands of the different materials have different energy with respect to the vacuum level (the offset is totally located in the valence band). This eliminates the barrier for electron transport, increasing the potential barrier for hole transport. On the other hand, when the electron affinity plus the band gap is the same for all the layers, the valence bands of the different materials have the same energy with respect to the vacuum level (the offset is totally located in the conduction band). In this case, the barrier for the transport of holes is reduced, enhancing the collection of holes (minority carriers). The output characteristics of the solar cell are consequently enhanced. Table 4.1 shows the sensitivity of the light J-V characteristics when all the offset happens in the conduction or the valence band.

In general, when the density of defects in the mid gap increases the output characteristics of the solar cell decreases due to higher recombination in the intrinsic layer. This is the case for wider valence band tail, wider defect pool or higher capture cross section.

The reproduction of measured solar cells is carried out by a careful control of model parameters. The current-voltage characteristics of the solar cell under dark and illumination condition as well as the spectral response exhibit an excellent match between the simulated and the measured cell (Figs. 4.2, 4.3 and 4.4). These model parameters are used as baseline to perform further simulations.

## 4.3 Results

### Experiments

The p-i-n amorphous silicon-germanium alloy solar cells studied in this research were grown in an ultrahigh vacuum multi-chamber system (PASTA) by Plasma Enhanced Chemical Vapor Deposition (PECVD). The substrates were textured SnO<sub>2</sub> coated on glass (Asahi U-type). There was no TCO at the back contact, between the n-layer and the metal (Ag) for optical enhancement. Deposition of the i-layer was done at a substrate temperature of 200°C, at a pressure of 1.65 Torr and an rf power density of 42 mWcm<sup>-2</sup>. The structure of the devices included a graded a-SiGe:H layer separated from the doped layers at both sides by buffers made with a-Si:H. By varying the germane flow during deposition, the graded a-SiGe:H intrinsic layers are fabricated as staircase profiles of four steps between the buffer layers and the lowest band gap (1.55 eV) layer. The band gap of the films was obtained from reflection and transmission optical measurements, identifying the band gap to the photon energy at which the absorption coefficient is 10<sup>3.5</sup> cm<sup>-1</sup>. The total density of dangling bond and the Urbach tail were extracted with the CPM technique. The activation energy of the material in each single layer was obtained from the temperature dependence of the dark-conductivity (after annealing at 160°C for one hour inside a vacuum chamber). Current-voltage (J/V) measurements of single a-SiGe:H cells were carried out in the dark, under AM 1.5 light and with filtered light. As a filter, a 100 nm a-Si:H layer on a glass substrate was used to simulate the light that reaches the bottom cell in a tandem structure.

The Rutherford Backscattering Spectrometry (RBS) measurements were done to determine the Ge/Si depth profile in the i-layer of the solar cell. The samples were a-SiGe:H deposited on a c-Si wafer. These samples had the same staircase profiles as the single junction cell but without the doped and the buffer layers. The composition profile of the samples was probed with 1.5 MeV He<sup>+</sup> ions.

### Modelling

A typical a-SiGe:H band gap structure under study is shown in Figure 4.1. It shows the band diagram of the p-i-n a-SiGe:H at short circuit conditions calculated by D-AMPS under AM1.5 illumination. The doped p- and n-type layers, separated from the intrinsic layer by a front and a back buffer are shown. The intrinsic layer consists of a 4-step staircase front grading between the p-layer and the uniform lowest band gap layer, and a 4-step staircase back grading between the lowest band gap layer and the n-layer.

For fitting purposes the optical parameters, band gaps, activation energies,

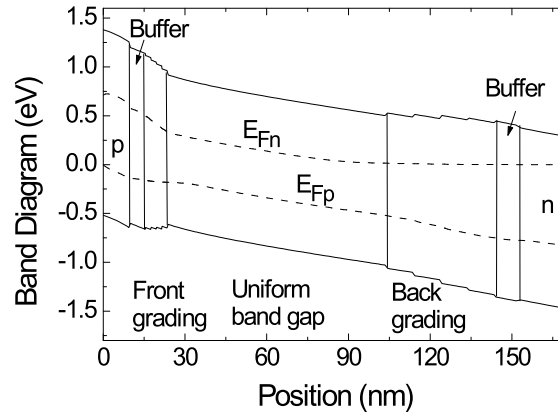


**Figure 4.1:** Computer generated band diagram of the a-SiGe:H p-i-n solar cell at short circuit conditions. The quasi Fermi levels for electrons ( $E_{Fn}$ ) and holes ( $E_{Fp}$ ) are shown by dotted lines.

total densities of dangling bonds and valence band slopes were provided by experiments. Most of the other electrical parameters were either adopted within the limited range regularly used in the literature or they do not affect the results. Dangling bond cross sections and band offsets are the only parameters not very well known (see Table 4.1), affecting the simulated J-V and SR curves. With respect to the band offset Fortmann et al. [55] proposed a flat valence band and all the offsets in the conduction band. Vasanth et al. [90] consistently observed a higher  $V_{oc}$  in the simulation than in practice, which they attributed to the location of the offset in the conduction band. Smole et al. [91], following the studies of Xu et al. [89], opted for equally dividing the offset between the valence and the conduction band. This is the option followed in this study.

The energy distribution of defect states in the band gap as a function of the alloy contribution is also controversial [92,93]. By electron spin resonance (ESR) measurements Si-related dangling bonds can be distinguished from Ge-related dangling bonds. On the other hand, Stiebig et al. [94] studied a-SiGe:H with a wide range of Ge concentrations by CPM and PDS measurements. The results from deconvoluting the sub-band gap spectra suggested that non significant differences exist between the capture cross sections or energy position for Si- and Ge- related dangling bonds. Cohen [95] has studied transient photocapacitance

spectra for a series of *a*-SiGe:H samples containing between 5 to 40 at.% Ge. To decompose the spectra two bands representing Si and Ge defect bands were needed for Ge concentration below 10 at.%, while only one band was needed for samples with 40 at.%. In accordance with these results, and taking into account the *a*-SiGe:H used in this study has 40 - 50 at.% Ge concentration, the defect distribution adopted in this study considers only one type of defect with a single capture cross section.

Sensitivity studies were performed for several parameters to determine their influences on the solar cell characteristics (especially the band gap, electron and hole mobility, charged and neutral cross sections, valence band tail slope, offset of the band gap and total density of states). Relations between some of the parameters used for the simulation have been consistently observed for several groups. For example the band gap of the *a*-Si:H is reduced continuously by alloying with germanium [96]; the total density of states increases exponentially with decreasing band gap [97]; and the Urbach tail, which reflects the valence band tail, increases linearly with decreasing band gap [88]. To probe the consistency of the results presented through out this chapter, simulations have been carried out in which several set of parameters used did not closely fit the experimental results. However, the variations of these set of parameters were done in keeping with the established relations as mentioned previously between the other parameters within the set. The trends observed with different sets of parameters are consistent and independent of the set of parameters selected. This permits us considering the tendencies as a real behaviour, independent of the set of parameters chosen, even when these parameters are finally selected to fit the experimental results.

To understand the influence of these models on the complete behavior of the solar cell, the density of dangling bond states was modelled using the two different electrical approaches previously described: (a) the model of uniform gap states density in each layer of the device (UDM), and (b) the defect pool model (DPM) as proposed by Powell and Deane [82,83].

#### **4.3.1 Defect Pool Model versus Uniform Defect Model for fitting purposes**

With the previous ideas in mind, Figures 4.2, 4.3 and 4.4 show the fit obtained for measurements of the dark current voltage (J-V), the illuminated (AM1.5 light) J-V characteristics and the spectral response (SR) curves at short circuit conditions under AM1.5 bias, respectively. It is obvious from these figures that it is possible to fit the J-V and the SR characteristics of the p-i-n structure in the initial state using either the UDM or the DPM approach. Except for the dangling bond

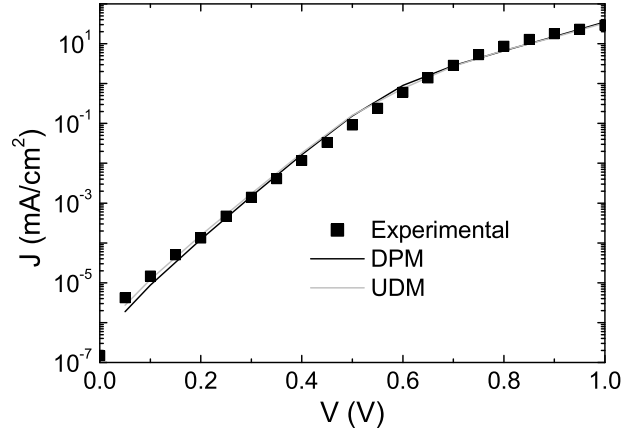


**Figure 4.2:** Measured and simulated dark current density-voltage characteristics of the single *a*-SiGe:H p-i-n solar cell.

**Table 4.2:** Total DB densities used in the UDM and position of the defect pool used in the DPM for fitting purposes.

Layers	doped	buffers	1 <sup>st</sup> & 9 <sup>nd</sup>	2 <sup>st</sup> & 8 <sup>nd</sup>	3 <sup>st</sup> & 7 <sup>nd</sup>	4 <sup>st</sup> & 6 <sup>nd</sup>	lowest grading band gap
DB ( $10^{16}\text{cm}^{-3}$ ) (UDM)	500	25	17.5	12.5	9.3	7.0	4.7
$E_P$ (eV) (DPM)	(p) 1.30	1.2	1.17	1.14	1.1	1.05	1.00
	(n) 1.20						

densities, all the electrical and optical parameters were assumed identical in both models. Table 4.2 gives the total dangling bond densities used in the UDM model and the most probable position of the defect pool ( $E_P$ ) used in the DPM model. Identical parameters were adopted for the layers with the same band gap.

Experimental studies show that the density of dangling bonds in good quality *a*-Si:H materials is around  $5 \times 10^{15}\text{cm}^{-3}$  while in good quality *a*-SiGe:H with optical gaps near 1.55 eV it is around  $5 \times 10^{16}\text{cm}^{-3}$ . This density increases with the concentration of Ge in the material [75]. In a UDM model, the density of dangling bonds of the various layers of the cell should correspond approximately to the density of dangling bonds of individual layers (materials) determined by experi-

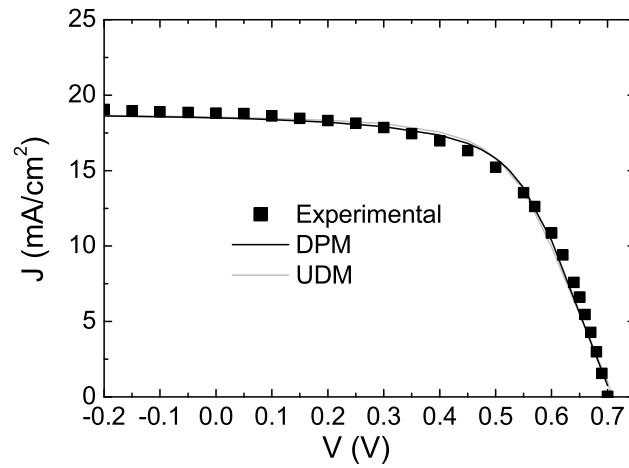


**Figure 4.3:** Measured and simulated illuminated current-voltage characteristics of the single *a*-SiGe:H p-i-n solar cell.

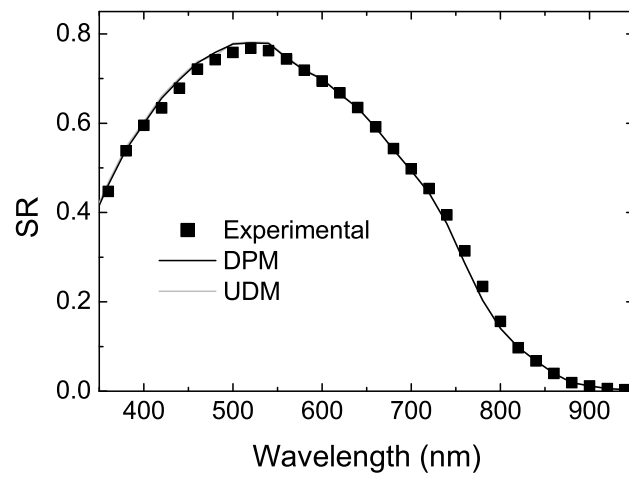


**Figure 4.4:** Measured and simulated spectral response characteristics at short circuit conditions under AM1.5 bias light of the single *a*-SiGe:H p-i-n solar cell.

ment. In such a case, if we choose a density of dangling bonds of  $5 \times 10^{15} \text{cm}^{-3}$  for the buffer layers and increase this density for increasing Ge concentration up to  $5 \times 10^{16} \text{cm}^{-3}$  until the lower desired band gap is reached (as it should be in accordance with the properties of the individual layers from the experiments), the simulation results with D-AMPS predict a very optimistic fill factor, FF, far from the experimental. The density of dangling bonds of the grading layers was therefore chosen to fit the experimental solar cell characteristics. In this case the density of dangling bonds *decreases* from the buffer layers towards the lower band gap material in the intrinsic a-SiGe:H (as shown in Table 4.2). This result contradicts the previously described experimental increase in density of dangling bonds with alloying [75]. The Defect Pool Model does present however a density of dangling bonds increasing in the experimentally observed direction. This gives more support to the DPM than to the UDM.

The profile of dangling bonds discussed for both models is presented in Figure 4.5, which compares (for the equilibrium state) the density of dangling bonds generated by the Defect Pool Model with the density of dangling bonds used in the Uniform Density of states Model. They are the profiles needed to fit the J-V and SR experimental curves. One can clearly see that the UDM case presents a lower density of dangling bonds for the lower band gap layer and how this density increases with the band gap, contrary to what is observed. On the other hand, the DPM tends to generate more dangling bonds near the p/i interface than near the i/n interface, due to the dependence of the dangling bonds on the position of the Fermi level. The comparison of the electric field profiles indicates that the DPM model leads to an increase in the electric field in the front and back grading and to a decrease in the electric field inside the bulk with respect to the UDM model (see Figure 4.6). In this figure, the right axes correspond with the band gap of the material in each of the layers used in the staircase profile for the UDM, stressing the non-experimental observation that the defect density decreases with the band gap in a-SiGe:H material. The DPM model tends to generate more positive trapped charges near the p/i junction and more negative trapped charges near the i/n junction than the UDM model. This can be clearly seen in the front region of the device in Figure 4.5. In the back region of the device we have to keep in mind that only between 2/5 and 3/7 of the total density of dangling bonds is effective in generating negative charge in the UDM model. Higher trapped charge concentrations near the p/i and n/i interfaces weaken the electric field in the bulk region. Recombination losses are more significant in the bulk using the DPM model and in the grading layers using the UDM model. We have to keep in mind that in lower band-gap materials (like for instances in a-SiGe:H) mid-gap states rather than tail states dominates in trapping and recombination processes. The scenario

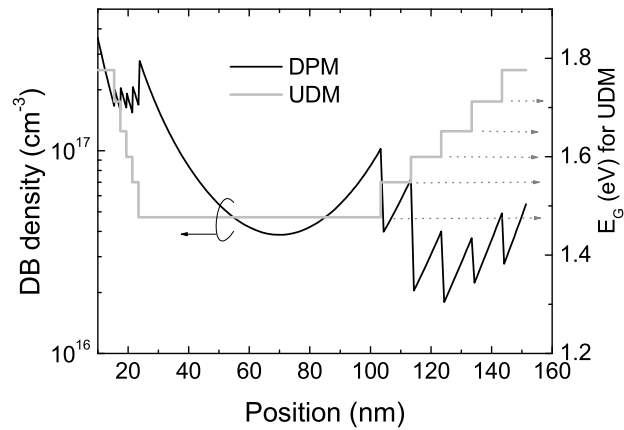


**Figure 4.5:** Comparisons of the dangling bond densities generated by the DPM and those used in the UDM to fit the J-V and SR experimental curves. The right axes correspond with the band gap of the material in each of the layers used in the staircase profile for the UDM.

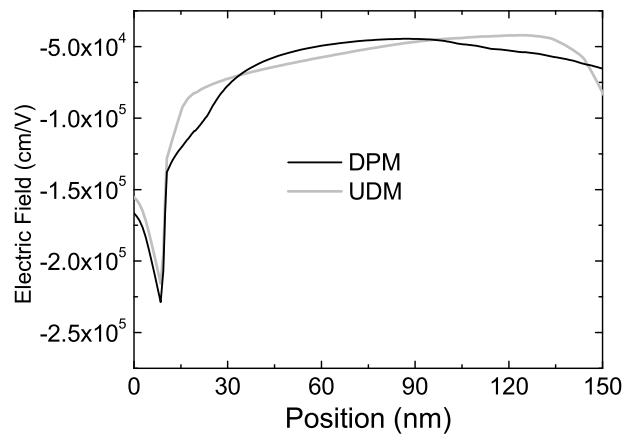


**Figure 4.6:** Change in the electric field profile under short circuit conditions and TFAM1.5 red bias light.

is quite different in a-Si:H where tails states and mid-gap states compete among themselves to define trapping and recombination.

### 4.3.2 Computer Predictions using the UDM and the DPM models

In order to optimize the performance of the single p-i-n a-SiGe:H solar cell, the dependence of the efficiency with respect to device band gap profile is studied using the models described previously and used for fitting the experiments. The main purpose of this section is to determine which of the models is capable of making predictions (not only fittings), which will open new ways of developing the a-SiGe:H solar cell.

The application of a-SiGe:H p-i-n structures as bottom sub-cells of a-Si:H/a-SiGe:H tandem solar cells is simulated in the following by replacing the AM1.5 illumination for filtered light. This light source results from filtering AM1.5 light through a thin a-Si:H layer having the same thickness as the intrinsic layer used in the top sub-cell of our a-Si:H/a-SiGe:H tandem cells. The light spectrum resulting after the absorption of the AM1.5 light by one pass through the a-Si:H thin film is termed TFAM1.5 light.

To avoid possible degradation resulting from excessively thick intrinsic layers, as has been widely observed [98], the total thickness of the i-layer is fixed at 150nm. This thickness excludes both doped layers and guarantees the presence of a strong enough electric field inside the intrinsic layer protecting the cell from Staebler-Wronski (SW) effect.

The study of the influence of the band gap profile on the solar cell performance is accomplished by varying systematically the devices layer thickness that defines the intrinsic layer (the front and the back gradings as well as the lowest band gap layer). When the lowest band gap layer thickness is reduced (increased), the excess (lack) of thickness is assigned in various proportions to (subtracted from) the front grading and/or to the back grading. Several possible cases are simulated for every thickness of the lowest band gap layer. In this way, the lowest band gap layer thickness is varied from 80 nm (curve A, Fig. 4.7) to a thickness of 10 nm (curve D, 4.7). Figure 4.7a represents the prediction made using the DPM while Figure 4.7b shows the predictions made with the UDM. The four layers that constitute the front grading are adopted of equal thickness. The same is applied to the back grading. The thickness of the buffers is unchanged.

The DPM predicts an improvement of the efficiency for a certain profile extending over the front grading, the lowest band gap layer and the back grading (36nm x 10nm x 90nm, respectively) (Fig. 4.7a). The advantage of this profile versus no profile has been previously experimentally demonstrated in the literature [90,99]. This band gap profile has been described in the literature as a 'V'-profile. On the other hand, the UDM predicts an optimum in efficiency when the front grading is completely removed (Fig. 4.7b). No experimental results confirm this outcome.

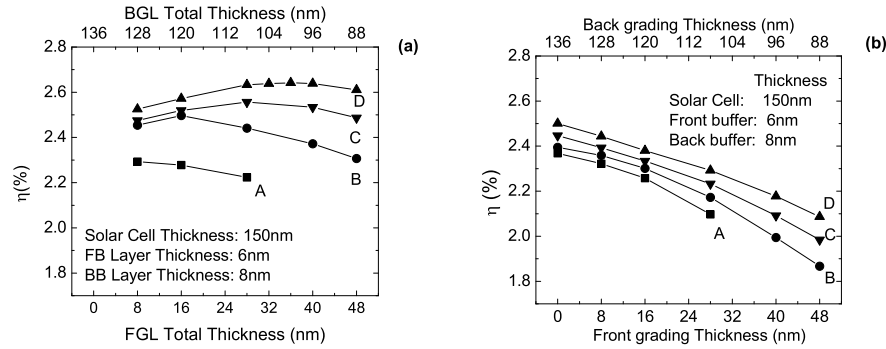


**Figure 4.7:** Dependence of the solar cell efficiency under TFAM1.5 red bias light with respect to the front and back band gap graded layer thicknesses. Labels:(A): 80 nm; (B): 40nm; (C): 20nm; (D): 10nm. Figure a: DPM. Figure b: UDM.

Next, the influence of the buffers is studied with both models. This study concerns only the electrical and optical influences of the buffer made with a well-defined material. Other effects related with inter-layer reactions during deposition (as the use of buffer as protecting or seed layers) are outside of the simulation possibilities. For the DPM the best profile previously obtained is used. For the UDM an intermediate profile with the same thickness for the lowest band gap layer is selected. With the two profiles the thickness of the buffers is varied. Figure 4.8 shows the efficiency as a function of the buffer thickness for the DPM (Fig. 4.8a) and the UDM (Fig. 4.8b). The total thickness of the solar cell is kept constant. Then, when the front buffer thickness is increased (decreased) the front grading thickness is decreased (increased) simultaneously. The low x-axis represents the front (back) buffer thickness and the top x-axis represents the front (back) grading thickness.

The simulation results are discussed in detail in the next two points.

### Influence of the front grading and front buffer

Concerning the buffers, the first important difference between the models found in the computer predictions is that an optimum thickness for the front buffer layer is recommended by D-AMPS when the DPM model is invoked and the entire removal of this layer is advised by D-AMPS when the UDM model is implemented. With respect to the grading, for these two different dangling bonds representa-

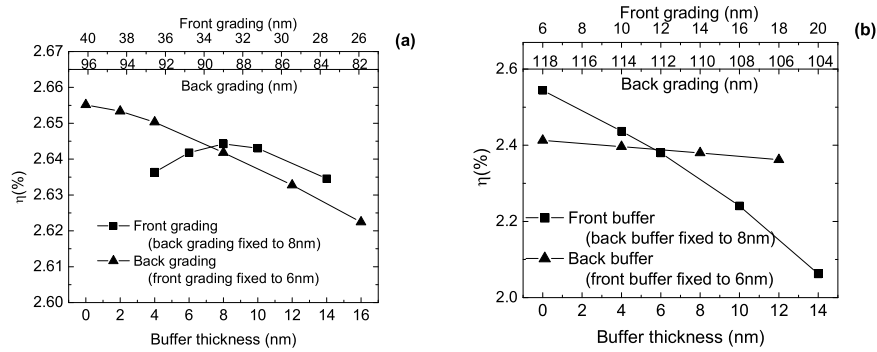


**Figure 4.8:** Dependence of the solar cell efficiency under TFAM1.5 red bias light with respect to the front and back buffer layer thicknesses. The front graded thickness is in one to one correspondence with the front (back) buffer thickness only (to keep the total thickness constant). Figure a: DPM. Figure b: UDM

tions the code predicts an optimum thickness for the front band-gap graded layers within the DPM model and the highest efficiency is achieved when the front grading is removed within the UDM model. Both predictions of D-AMPS when the UDM model is used are in contrast with experimental experience, while those of D-AMPS when the DPM model is used are in agreement with experimental practice. In order to understand the origin of such different predictions the computer generated electric field, concentration of trapped charges and recombination rate profiles are inspected.

UDM model: it is well known that the presence of front layers (as buffer or as grading) introduces a redistribution of the electric field in the solar cell. The positive charge trapped in these layers ( $D^+$  states predominates) enhances the electric field around the p/i interface and weakens the electric field in the intrinsic layer bulk. With the UDM approach, when the front layers (buffer or grading) are made thinner or when they are completely removed, the electric field becomes reinforced in the intrinsic a-SiGe:H bulk where recombination losses are more significant due to the lower mobility gap and the higher density of dangling bonds present in the lowest band gap layer. At the same time, the electric field is weakened at the front region of the a-SiGe:H layer near the p/i interface where recombination losses are less important (see Fig. 4.6). This redistribution of the electric field when the front layers are removed produces a net reduction of the global recombination loss present in the solar cell and gives rise to an improvement of its

overall performance (see Fig. 4.8b).

**DPM model:** Figure 4.5 shows that the DPM model introduces a significant density of dangling bonds near the p/i junction. These dangling bonds are mostly  $D^+$  states and provide positive trapped charges. Similarly dangling bonds introduced by the DPM model near the i/n junction are mostly  $D^-$  states and provide negative trapped charge. These extra  $D^+$  and  $D^-$  states generated by DPM significantly influence the electric field profile inside the bulk. Hence, when the front layers are made thinner or removed, the electric field in the intrinsic layer bulk is much less affected within the DPM model than in the UDM model. The dangling bond profile generated by the DPM model inside the lowest band gap layer already defines the electric field profile to a great extent. The second important point is that when the DPM model is invoked, the removal of front layers in the a-SiGe:H single p-i-n solar cells still produces a redistribution on the electric field that is quite different to the one found in the UDM model. When front layers are made thinner or removed the Fermi level in equilibrium moves closer to the valence band edge in the front region of the intrinsic layer, which forces the DPM model to generate a higher concentration of  $D^+$  states near the p/i interface. These additional  $D^+$  states reinforce the electric field near the p/i and the i/n junction and weaken the electric field in the bulk region (see Fig. 4.6). This redistribution of the electric field is quite different from the one observed in the UDM model. The third point to make is that these additional  $D^+$  states created by the DPM model not only strengthen the electric field but also increase recombination losses near the p/i interface. This trend is never observed in the UDM model where an increase (decrease) in the electric field is usually accompanied by a decrease (increase) in recombination losses. Thus there is a trade-off between too thin and too thick front layers. Very thin front layers have the negative effect of weakening the electric fields in the front region of the bulk where dangling bonds are mainly  $D^+$  states and recombination losses are significant. Very thick front layers have the negative effect of weakening the electric field in the back region of the bulk where dangling bonds are mainly  $D^-$  states and also recombination losses are important (Figures 4.7a and 4.8a). In the UDM model the physics is simpler: thinner front layers just enhance the electric field on the entire bulk region, decreasing the overall recombination losses and thicker front layers produce the opposite effect.

### **Influence of the back grading and back buffer**

When the back grading or the back buffer is made thinner a redistribution of the electrical field in the intrinsic a-SiGe:H layer is observed. In the UDM model the electrical field becomes weaker at the back region and stronger at the front region

of the intrinsic layer. Hence recombination losses become stronger (weaker) at the back (front) side of the intrinsic region. The most significant changes in recombination losses take place at the back region of the intrinsic layer what makes D-AMPS to predict higher efficiencies for thicker back grading (see Fig. 4.7b). In the DPM model, the field becomes stronger at the back region of the intrinsic layer and weaker at the front region of the intrinsic layer. However recombination losses also increase in the back region of the intrinsic layer for thinner back layers. The Fermi level in equilibrium is placed closer to the conduction band edge at the back region of the intrinsic layer which forces the DPM model to generate more dangling bonds ( $D^-$  states), enhancing simultaneously the electric field and the recombination losses. As a result of this, both models predict similar trends but different thicknesses for the back grading as can be seen in Figure 4.7.

The solar cell efficiency is more sensitive to changes in thickness of the front layers than of the back layers. It is important to notice that both the UDM and the DPM models are suggesting the removal of the back layer. However when the back buffer is made thinner the back grading is becoming at the same time thicker which results in a better optical absorption. The models predict a better performance of the solar cell when the back grading is made thicker. In this direction, an optimal thickness of 300 nm is predicted before the electric field collapse, and no degradation effects are introduced in the simulation.

Summarizing, the use of the uniform density of state model (UDM) cannot justify with D-AMPS the implementation of U- or V-shape band-gap profiles in the intrinsic layer of single p-i-n a-SiGe:H solar cells to improve its performance. On the contrary, using Defect Pool Model (DPM) in the computer simulations demonstrates the benefits of V-shape band gap profiles in the intrinsic a-SiGe:H layer in agreement with the experimental work of Guha et al [64,99] and Vasanth et al. [90], among others.

Knowing that the defect pool model is not only able to fit the experimental solar cell characteristics with physical inputs, but also presents trends widely observed from several groups, in the rest of the chapter the DPM is implemented in the computer model to predict new trends in the influence of the band gap profile, which will open new directions on the improvement of the a-SiGe:H solar cell.

### 4.3.3 Influence of the band gap profile studied by computer simulation

The profiling of the band gap of the intrinsic layer modifies simultaneously the distribution of the trapped charge and the electric field profile, which strongly influences the recombination rate. An appropriate band gap profile leads to a reduc-

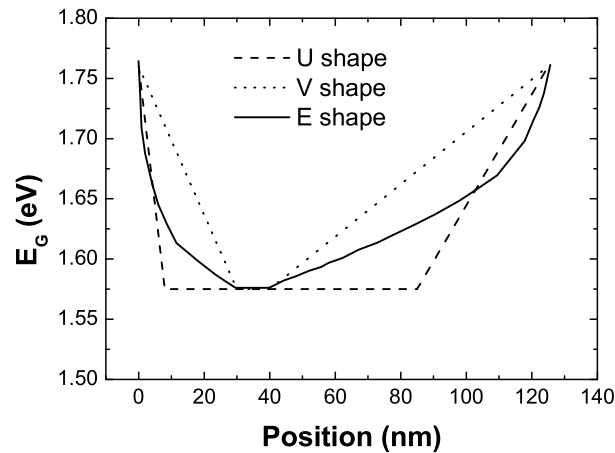


**Figure 4.9:** Schematic i-layer band gap profiling of the 'U-shape', 'V-shape' and 'E-shape' structures, without buffer layer.

tion in the recombination losses and to an improvement in the carrier collection within the i-layer.

Studying the losses that are present in the U-shape and V-shape band gap profile is the first step presented. These two profiles will then be compared with a new profile, which is designed for application in an a-SiGe:H bottom cell of a tandem structure. This new profile, named exponential profile (E-profile), will be described in detail.

The U-shape band gap profile used in the intrinsic a-SiGe:H layer of our solar cells, presents a short front grading ( $\sim 10$  nm), a long uniform low band gap layer ( $\sim 70$  nm and 1.5 eV) and a long back grading ( $\sim 40$  nm). Figure 4.9 shows the schematic U-shape i-layer band gap profile, excluding the buffer layers. The other two profiles in this figure are the V- and the E-shape profile. These two profiles are simulated starting from the U-shape profile by modifying only the thickness of the layers that form the i-layer. The same is done for the deposition of the solar cells where the only parameter modified is the deposition time of the individual layers.

The recombination losses in these structures have been studied in detail by simulating the cell with the computer code D-AMPS. Looking at the recombination profile at different forward bias voltages and for filtered light (TFAM1.5) for the U-shape band gap profile (Figure 4.10) it is observed how the main recombi-

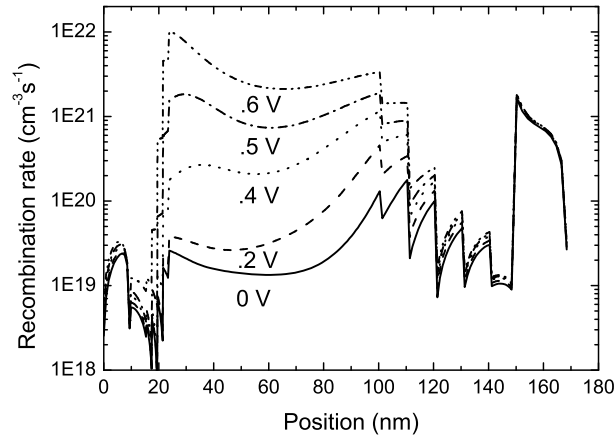


**Figure 4.10:** Spatial recombination rate for the 'U-shape' structure under different bias conditions (filtered illuminated TFAM 1.5).

nation region shifts from the rear part of the bulk, for 0 voltage bias, to the bulk at forward biases and to mostly the front of the bulk, near the p/i junction, for 0.6 V (a value close to the open circuit voltage,  $V_{oc}$ ).

The recombination current is directly responsible for the fill factor (FF) of the solar cell. It also has a significant influence on the  $V_{oc}$ . If the dark I-V characteristic of an a-Si:H alloy solar cell is shifted by the short circuit current ( $J_{sc}$ ) value under illumination (assuming that the superposition principle is valid), we end up with a  $V_{oc}$  that is significantly higher than the experimental  $V_{oc}$ . This is due to the rather large density of defects that is present in a-Si:H alloys, producing large recombination currents at forward voltages. Figure 4.11 shows the difference between the generation rate and the recombination rate for different forward voltages under filtered light for the U-profile. The loss of current due to the high recombination at forward bias results in a net current that is strongly bias dependent. The losses by recombination are clearly dominant near the p/i junction at high bias voltages, and they cause low FF and  $V_{oc}$  in the U-shape profile.

To increase the  $V_{oc}$  and to improve the FF, the recombination current should be lowered at high forward biases. An easy way to accomplish this is to elongate the front and back grading and reduce the thickness of the lowest band gap layer. Using material with a larger band gap (lower Ge concentration) reduces the density of trapped charges by reducing the defect density in the band gap. This strengthens the electric field in the bulk, and the cell thus extracts the photo

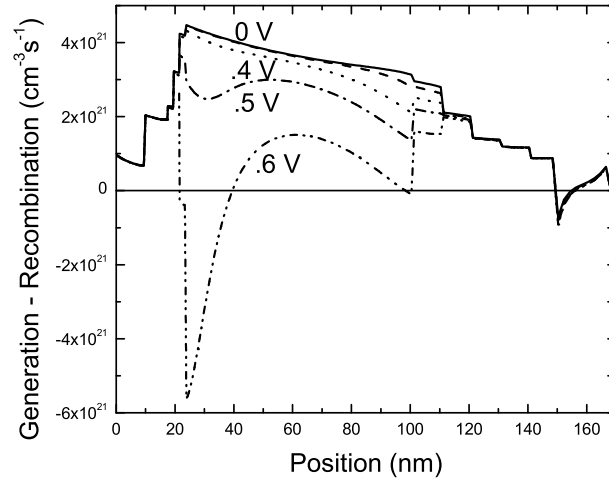


**Figure 4.11:** Generation (G) minus spatial recombination (R) rate for the 'U-shape' structure under different bias conditions (filtered illuminated TFAM 1.5).

**Table 4.3:** Solar cell simulated parameters of a U-, V- and E-shape p-i-n structure under illumination conditions of AM 1.5 spectrum without and with a filter of 100nm thick a-Si:H.

		$V_{oc}$ (V)	$J_{sc}$ (mA/cm <sup>2</sup> )	FF (%)	$\eta$ (%)
<b>U-shape</b>	AM 1.5	0.72	18.3	58.9	7.72
	TFAM 1.5	0.65	6.58	59.4	2.56
<b>V-shape</b>	AM 1.5	0.77	17.0	62.5	8.20
	TFAM 1.5	0.71	5.75	63.7	2.61
<b>E-shape</b>	AM 1.5	0.74	18.0	62.4	8.33
	TFAM 1.5	0.68	6.38	63.5	2.77

generated carriers more efficiently. Finally, the recombination losses are reduced, resulting in a higher FF and  $V_{oc}$ . But this approach has some drawbacks. A larger band gap material means a lower absorption coefficient and therefore a lower  $J_{sc}$ .

This indeed is the behavior observed in a V-shaped band gap profile, and it

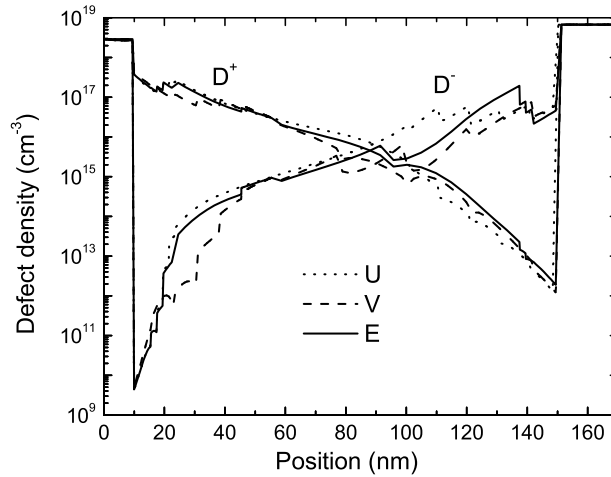


**Figure 4.12:** Spatial distribution of positively charged ( $D^+$ ) and negatively charged ( $D^-$ ) defect states inside the i-layer with 'U-shape', 'V-shape' and 'E-shape' profiles at 0V.

has also been observed experimentally as well as with simulation by Vasanth et al. [90]. Figure 4.9 compares the schematic band gap profile in the a-SiGe:H i-layer of a single junction having a U-shape and a V-shape profile. Table 4.3 displays the simulated current-voltage characteristics for the different band gap profiles. The position of the layer with the minimum band gap in the V-profile was optimised by computer simulation [100], as has been showed previously. Under filtered light and AM1.5 illumination, the V-shape leads to a significant improvement in  $V_{oc}$ , FF and efficiency ( $\eta$ ), as compared to the U-shape. The deeper front grading at the p/i interface in the V-type profile decreases the charged defect state density near the p/i-interface due to the Fermi level dependence of the defect state distribution predicted by the defect pool model. Figure 4.12 shows the equilibrium distribution of positively charged ( $D^+$ ) and negatively charged ( $D^-$ ) defect states at short circuit conditions and filtered light. The charged defect densities are significantly reduced by 30% within the i-layer with a V-shape band gap profile, especially the dominant negatively charged defect ( $D^-$ ) at the middle and rear part of the i-layer. The electric field improves as a result of the reduced screening introduced by space charge; it becomes more uniform inside the i-layer and decreases at the p/i and i/n junction (Fig. 4.13). The result is a reduction in the recombination process in the bulk of the i-layer, which in turn improves the  $V_{oc}$ . On the other hand, reduced recombination in the middle of the i-layer has an effect on FF. The

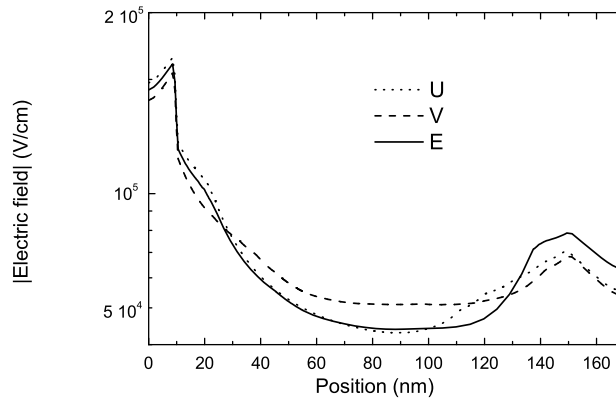


**Figure 4.13:** Electric field within the 'U-shape', 'V-shape' and 'E-shape' profiles at 0V.

larger back grading reduces the density of charged defect states in the middle and near the  $i/n$  junction. The screening effect of the electric field is reduced, improving the mobility-lifetime-electric field ( $\mu\tau E$ ) product and thereby improving the carrier extraction which decreases the recombination in the bulk and in the rear part of the cell. Thus the FF improves due to the overall reduction of the recombination current. Together, both the front and the back grading of the V-profile lead to better performance than the U-shape. Nevertheless, the V-shape leads to a loss in the short circuit current. Figure 4.14 shows the generation rate for the U- and V-shape profiles. A reduction in the optical generation is observed in the regions where the band gap has been increased. Finally, the enhancement in carrier collection does not compensate for the loss of photo generated carriers.

It is necessary to have a more sophisticated band gap profile that would be capable of reducing the recombination rate but at the same time maintains the  $J_{sc}$  that a U-shape profile generates.

By computer simulation we have designed a new band gap profile [101], exponential profile (E-shape profile), which reduces the recombination current, enhancing the FF and  $V_{oc}$ , and at the same time generates the same  $J_{sc}$  as the U-shape profile. Table 4.3 displays the simulated current-voltage characteristics for the three different band gap profiles. Figure 4.9 shows a schematic band gap profile of the  $i$ -layer of the a-SiGe:H single junction comparing a U-shape and an E-shape profile.

In amorphous silicon alloys the main loss of carrier collection is caused by bulk recombination. To reduce the bulk recombination, the density of states in the

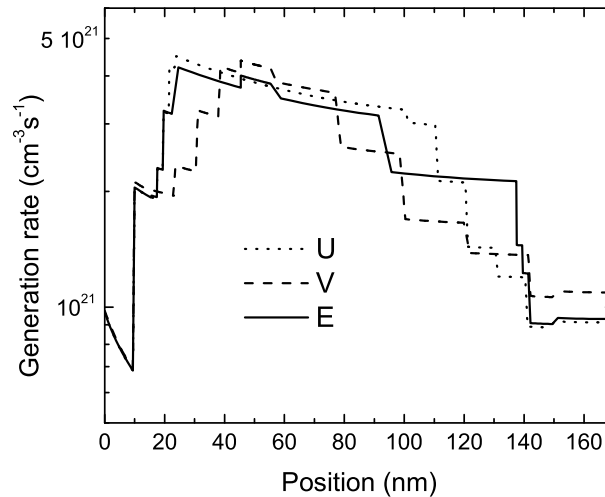


**Figure 4.14:** Generation rate within the solar cell with 'U-shape', 'V-shape' and 'E-shape' profiles at 0V (filtered illuminated TFAM 1.5).

band gap is modified by controlling the alloying of the amorphous silicon. This must be achieved with a gradual enlargement of the front and back grading by replacing the lower band gap material in the bulk of the intrinsic i-layer with a lower alloyed, higher band gap material. The higher band gap material introduces fewer defects inside the band gap, enhancing the electronic properties.

The gradual front grading moves the position of the minimum band gap away from the p/i junction. The electron and hole quasi Fermi levels can move further apart due to the higher band gap near the p/i interface, resulting in a higher  $V_{oc}$ . Comparing the shapes of the front grading between the E- and the V-profiles (Fig. 4.9) it is appreciated that even when both shift the minimum band gap position, the front grading of the E-shape profile generates more current, reducing the generation losses present in the V-shape profile. On the other hand the higher band gap in the front grading of the V-shape profile contributes to a higher built in potential, which we maintained in the E-shape profile.

The shape of the back grading is such that it reduces the mid gap defect density in the bulk of the intrinsic layer where the electric field is weaker. Figure 4.12 shows how the charged defect density, and specially the dominant  $D^-$  in the middle and rear parts of the ilayer, has been significantly reduced. Near the i/n junction the electric field is strong enough due to the high space-charge density

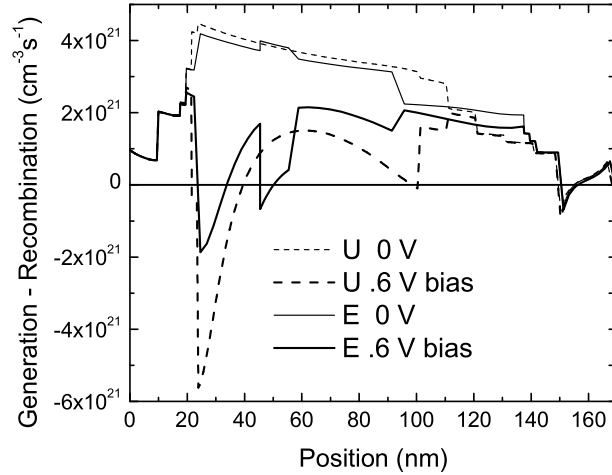


**Figure 4.15:** Generation (G) minus spatial recombination (R) rate for the 'U-shape' and 'E-shape' structure under different bias conditions (filtered illuminated TFAM 1.5).

in the highly doped n-layer. On the other side, near the p/i junction the built in potential is mainly dependent on the quality of the junction. These two ideas allow us to reduce the band gap near the i/n junction with respect to the U- and V- shape profile, while we increase it in the bulk. As we mentioned above, the material in the bulk has to host a low defect density due to the lower electric field strength in that region. This will reduce the recombination current, and improve the FF. Near the i/n junction we have decreased the band gap in order to generate the photocurrent that is lost by using the higher band gap bulk material. The high electric field in this region allows us to reduce the band gap without producing important recombination losses.

Figure 4.14 represents the generation profile under filtered light for the U- and E-shape band gap profile. The total generation rate is roughly the same in both profiles, with the advantage in the E-shape case of having less defect density in the bulk. Figure 4.15 represents the net generation (generation minus recombination) rate profiles for the U- and E- shape profile for different forward biases, under filtered light.

Figure 4.15 shows how the recombination current is generated as the forward bias increases. The E-shape profile presents lower recombination current than the U-shape for high forward bias, mainly in all of the bulk of the i-layer but especially near the p/i junction, resulting in an improved  $V_{oc}$ . The sharp increase

in the recombination current for E-shape in the region of the lowest band gap material is due to the "pool" for the carriers created in the band gap profile for this material. At high forward bias, the band gap profile tends to be flat, reducing the electric field. The free carriers are more sensitive to the discontinuities in the band profile at this low electric field. The lowest gap material acts as a "pool" where the free carriers are temporarily trapped with a consequent increase in the recombination. This thin low band gap layer could be removed, which would increase the FF and  $V_{oc}$ , but we keep it to obtain the same total generation in the E-shape profile as in the U-profile.

Considerable effort has been made by many groups in order to obtain more efficient band gap profiles. At the same time, band gap profiles that are easier to deposit are also desirable. The group of Jülich [102] presented an interesting idea, replacing the grading by an a-Si:H buffer near the p/i junction. In contrast with this idea, the simulations performed in this study predict that an appropriately designed band gap is necessary to improve the performance of the a-SiGe:H single junction even if these solar cells have a small thickness.

In summary, grading exponentially the band gap profile of the i-layer of the a-SiGe:H single junction solar cell generates roughly the same  $J_{sc}$  as the U-shape profile, but leads to higher FF and  $V_{oc}$ , with the result that the efficiency is improved.

In the next section these computer predictions are compared with experimental results for solar cells with the U-, V- and E- band gap profiles.

#### 4.3.4 From computer prediction to experimental observations

Several p-i-n single junction a-SiGe:H solar cells have been deposited with the three different band gap profiles. Table 4.4 shows the average solar cell characteristics for each profile. Together with the measurements appear the standard deviation of the parameter with respect to several measured cells. The deviation does not exceed 3.5 % in any of the parameters. The variation from the U- to the E-shape profile predicted by simulation is around 10 %, significant to rule out statistical deviations which could mask the results. The cells were deposited at the same time on a monitor Corning glass without TCO. The thickness of the whole cell was measured by R-T. The thickness of the different cells was the same within 10 nm. To simplify the comparison we have included the simulation values under filtered light of Table 4.3 as First Simulation. Where the simulations predicted a significant improvement in FF and  $\eta$  in the E- and V- profiles over the U-shape profile, as has been explained in the previous section, the deposited cells show the opposite behavior. The cells with V-shape profile show a higher  $V_{oc}$  and lower

**Table 4.4:** Solar cell experimental and simulated parameters of a U-, V- and E-shape p-i-n structure under illumination conditions of AM 1.5 spectrum with a filter of 100nm thick a-Si:H.

	$V_{oc}$ (V)	$J_{sc}$ (mA/cm <sup>2</sup> )	FF (%)	$\eta$ (%)
<b>U-shape</b> <i>Average (experiment)</i>	$0.64 \pm 0.01$	$6.5 \pm 0.2$	$62 \pm 2$	$2.57 \pm 0.05$
1 <sup>st</sup> simulation	0.65	6.58	59	2.56
<b>2<sup>nd</sup> simulation</b>	<b>0.66</b>	<b>6.55</b>	<b>61</b>	<b>2.65</b>
<b>V-shape</b> <i>Average (experiment)</i>	$0.67 \pm 0.01$	$5.8 \pm 0.2$	$62 \pm 1$	$2.43 \pm 0.08$
1 <sup>st</sup> simulation	0.71	5.75	64	2.61
<b>2<sup>nd</sup> simulation</b>	<b>0.68</b>	<b>5.88</b>	<b>64</b>	<b>2.56</b>
<b>E-shape</b> <i>Average (experiment)</i>	$0.65 \pm 0.01$	$6.3 \pm 0.2$	$61 \pm 2$	$2.54 \pm 0.09$
1 <sup>st</sup> simulation	0.68	6.38	64	2.77
<b>2<sup>nd</sup> simulation</b>	<b>0.66</b>	<b>6.72</b>	<b>61</b>	<b>2.68</b>

$J_{sc}$ , as predicted. This profile creates the stronger electric field in the bulk of the i-layer together with the lower defect density of states of the three profiles under study. Those properties are expected to produce a better FF in the solar cells with the V-profile. In contrast to this, the FF and  $\eta$  do not even reach the values that are obtained in the cells with U-shape profile. The case of the E-shape profile is more critical. Designed to improve the  $\eta$  and  $V_{oc}$  without losses in photo generated current, the deposited solar cells do not present any of these improvements.

In the case of the U-shaped profile, the simulations predict lower FF and  $\eta$  than those obtained in the deposited solar cells.

To understand these deviations between experiment and simulation we have performed RBS measurements on samples with these three profiles and we have compared the measured band-gap profiles with the designed profiles. The H concentration was found to be uniform through all the cell. The RBS spectra of three samples with band gap grading profiles U, V and E are shown in figure 4.17. A depth profile of the hydrogen concentration has been measured presenting a constant hydrogen concentration through all the film for the three profiles under study. This result permits an assumption of a linear relation between the amount of Ge in the material and the band gap. Figure 4.16 shows the band gap  $E_G$  versus the position, where the zero position is the surface of the substrate.

Comparing Figures 4.17 and 4.9 one clearly notes two important differences.

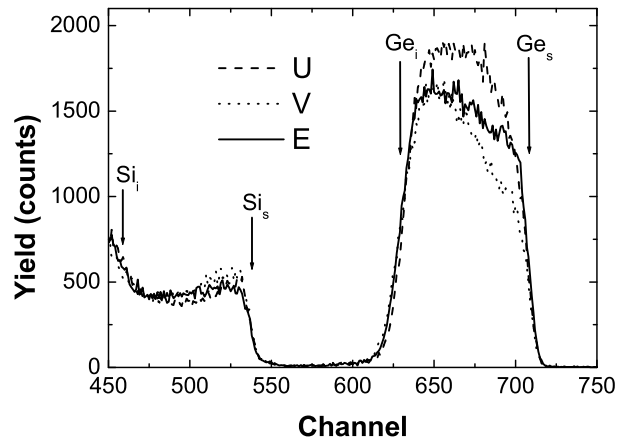


**Figure 4.16:** RBS spectra of samples with U-, V- and exponential (E) band gap profiles. The arrows indicated the surface channels of Si and Ge. Subscript "s" and "i" stand for surface and interface, respectively.

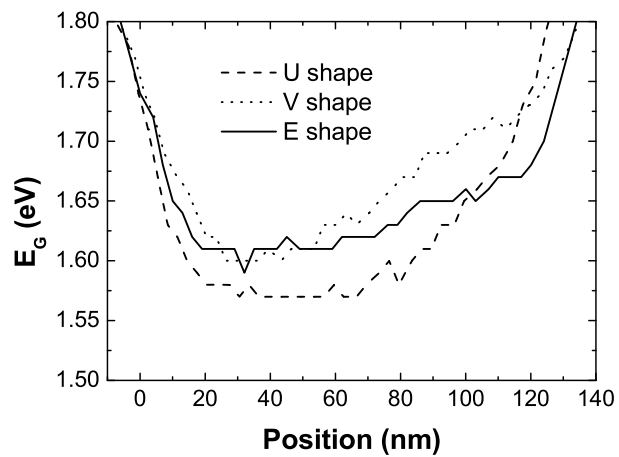


**Figure 4.17:** Band gap profile of measured samples as calculated from the RBS Ge profiles.

The first observation is that the V- and the E- shaped band gap profiles do not reach the low band gap values that are expected. The second observation is that the linear grading assumed from the gas flow in the U and V band gap profiles is in fact curved. This is possible as a result of a delay between the change in germane flow and the time it takes for this change in flow for producing changes in the concentration of Ge that is incorporated. Below will follow a detailed experiment corroborating this supposition.

In the staircase profile, where the changes in flow follow a regularly increasing or decreasing pattern, this delay produces only a small modification to the designed profile. However, these modifications to the profile still have a significant influence on the performance of the cell, as can be appreciated in Table II by comparing the first and the second simulations. The uniform change in flow is the case in both the linear U- and V- shape profiles. In these two profiles the changes in the germane flow are uniform in time as well as in amount of germane to produce a linear profile in the front and back grading of the intrinsic layer. The delay modifies the expected linear profiles, however the linearity is retained. In the U-shape profile, the front and back grading are thin compared with the total intrinsic layer (the total grading is the half of the i-layer, while in the V- and E-shape the grading represents the 90 % of the i-layer). Small variations in the grading will have less influence on the final cell behaviour.

The band-gap profiles in the simulation have been modified to follow the profiles as deduced from the Ge/Si concentrations (obtained from RBS) following the variations as caused by the delay. The modifications were done only in the thickness of step of the grading, with no intention of fitting the results but to observe if these modifications can account by them self with the mismatch between simulations and experiment. The new profiles are shown in Figure 4.18. The results of these simulations are included in Table 4.4, as Second Simulation. The small variation we have introduced in the simulation of the U-shape profile is enough to increase the  $\eta$  and FF, without modifying the open circuit voltage or the short circuit current. This brings the simulation closer to the experimental values and proves how a small variation of the front and back grading reduces the recombination. In the case of the V-shape profile, the variation of the band-gap profile reduces the  $V_{oc}$  and the  $\eta$ . The second simulation with the altered band gap grading also more closely approaches the experimental values.

Changing only the thickness of the layers, the E-shape profile is not possible to simulate. As the changes in germane flow are not uniform, the changes induced by the flow delay in the band-gap profile are larger. It may deposit in the grading a material with different characteristics than expected, compared with the U- and V-shape profile. However, introducing in the simulations the flow delay by changing

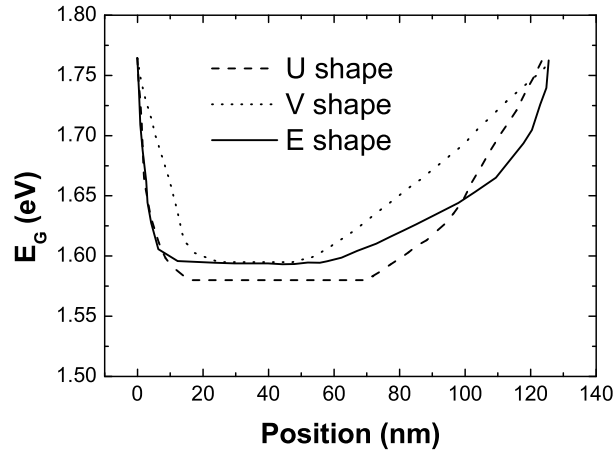


**Figure 4.18:** Simulated band gap profiles consistent with the RBS measured profiles taking into account a delayed response of the Ge incorporated on changes in the  $\text{GeH}_4$  flow. This is used in 2<sup>nd</sup> simulation.

the thickness of the step of the grading in the E band-gap profile, we observe how the adverse effect of this behaviour accumulates.

#### Study of the delay in Ge concentration in the plasma

To examine the influence of the flow delay, a film consisting of three layers was deposited with the following structure: 30nm of a-SiGe:H of  $E_G$  1.75eV, 60nm of a-SiGe:H of  $E_G$  1.56eV and 30nm of a-SiGe:H of  $E_G$  1.75eV. The RBS depth profile of this film together with a simulation profile of what we would expect from this structure are shown in figure 4.19. The slopes of the simulation and the measurement are parallel on the substrate side (a). However on the surface side (b), where RBS is more accurate, a higher concentration of Ge than expected is detected, which produces a difference in the slope between the simulation and the measurement. We associate this higher concentration of Ge with a delayed decrease in the  $\text{GeH}_4$  fraction in the chamber.

A second study of the influence of the flow delay was carried out with several films consisting of two layers. The delay is studied by comparing films where the plasma is stopped, the flow of germane is changed and the plasma is restarted with the desired composition with films where the flow of germane is changed without stopping the plasma. The thickness of each layer was kept small to increase the

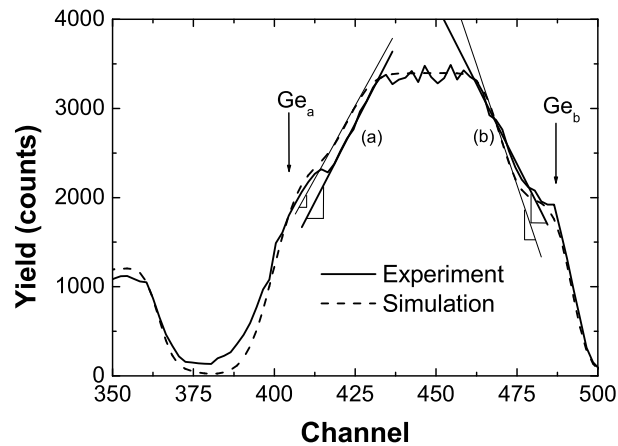


**Figure 4.19:** Experimental RBS spectra and yield simulation data of the 3 layers film. The slopes on the surface side (a) and the surface side (b) for both the film and the simulation are indicated.

RBS measurement accuracy and equally to simplify the comparison. Very small thickness differences are observed. The RBS depth profile for two sets of films is showed in Figure 4.20. Figure 4.20a corresponds with two films, one where the plasma was stopped and restarted and the other with continuous plasma. In this case the first layer was deposited with lower germane flow than the second. Figure 4.20b corresponds with two films, one where the plasma was stopped and restarted and the other with continuous plasma. In this other case the first layer was deposited with higher germane flow than the second. For each case the slopes where the layer change are plotted. When the flow of germane is increased, there is no considerable difference in the slopes when the plasma is stopped with respect to a continuous plasma deposition. This corresponds well with the results of the previous experiment at the substrate side. On the other hand a clear difference is observed when the germane flow is reduced. The slope in Figure 4.20b of the film with non-stopping plasma defines a more slight transition from the high to the low Ge concentration layer. Again this is in agreement with the results of the previous experiment on the surface side.

These results indicate that an increase in the GeH<sub>4</sub> flow is mirrored in the film composition profile with a constant delay, while a decrease in the GeH<sub>4</sub> flow leads to a continuously varying delay of Ge in the film.

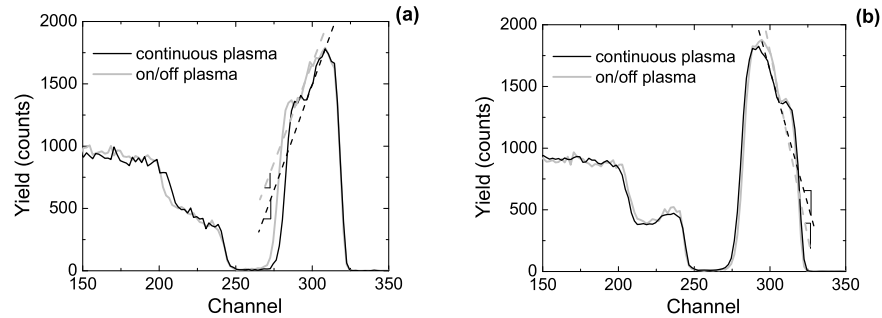


**Figure 4.20:** Experimental RBS spectra for a two-layer film where the germane flow is increased (a) or decreased (b) from the first to the second layer. "on/off plasma" stands for a film where the plasma is stopped, the germane flow changed and the plasma restarted. "continuous plasma" stands for a film where the plasma is not stopped when the germane is changed.

#### Modified exponential profile

With the knowledge of these experiments the E-shape profile has been modified in order to avoid the experimental delay and to obtain a real band gap profile closer to the original design. A p-i-n solar cell has been deposited including this correction. The characteristics of this cell are given in Table 4.5 where it is compared with the U- and V-shape profile. Figure 4.21 shows the J-V characteristics under AM 1.5 and TFAM 1.5. The intended improvements of the simulated E-shape profile are clearly observed as opposed to the standard U-profile: higher  $V_{oc}$ , FF and  $\eta$ , with no loss in  $J_{sc}$ .

## 4.4 Conclusions

In this chapter, the annealed state of a single junction *a*-SiGe:H p-i-n solar cell was studied by computer simulation. Two models describing the density of defect states in the band gap were compared. The uniform density of states model and the defect pool model. Both were able to fit the dark and the illuminated current voltage characteristics and the spectral response curve under short circuit conditions. It was found that the uniform density of state model was not able to justify improvements experimentally observed when the band gap is modified. On the other hand, the defect pool model showed agreement with the experimental ob-

**Table 4.5:** Solar cell experimental parameters of a modified E-shape p-i-n structure under illumination conditions of AM 1.5 without and with filter (TFAM 1.5), with respect to the best cells obtained with U- and V- profile.

		$V_{oc}$ (V)	$J_{sc}$ (mA/cm <sup>2</sup> )	FF (%)	$\eta$ (%)
<b>U-shape</b>	AM 1.5	$0.68 \pm 0.01$	$17.0 \pm 0.3$	$62 \pm 1$	$7.1 \pm 0.1$
	TFAM 1.5	$0.64 \pm 0.01$	$6.5 \pm 0.2$	$62 \pm 2$	$2.57 \pm 0.05$
<b>V-shape</b>	AM 1.5	$0.72 \pm 0.01$	$16.1 \pm 0.4$	$62 \pm 2$	$7.2 \pm 0.2$
	TFAM 1.5	$0.67 \pm 0.01$	$5.8 \pm 0.2$	$62 \pm 3$	$2.4 \pm 0.1$
<b>E-shape</b>	AM 1.5	$0.69 \pm 0.01$	$17.1 \pm 0.3$	$62 \pm 1$	$7.3 \pm 0.2$
	TFAM 1.5	$0.67 \pm 0.01$	$6.4 \pm 0.1$	$62 \pm 1$	$2.67 \pm 0.07$

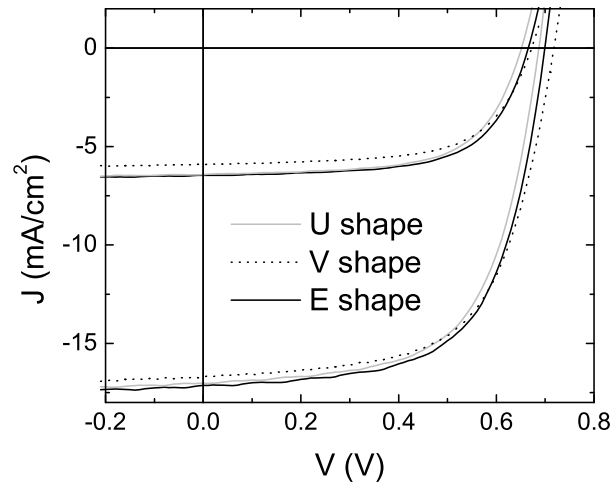


**Figure 4.21:** Solar cell experimental J-V characteristic of a modified E-shape p-i-n structure under illumination conditions of AM 1.5 without and with filter (TFAM 1.5), with respect to the best cells obtained with U- and V- profile.

servations.

Implementing the defect pool model, the influence of the band gap profile on the final characteristics of *a*-SiGe:H solar cells was studied. As a result, a new shape profile was found which increases the efficiency and the open circuit voltage without losses in photogenerated current. Experimental results following the direction observed in computer simulation were presented.

It can be concluded from this chapter that computer simulations must implement an appropriate model to correctly describe the complexity of the solar cell structure. Until now this model must be the defect pool model. It can be also concluded from the results obtained that computer simulation is a suitable tool to show new development directions when used in parallel with other experimental techniques.



## 5 Stability of *a*-SiGe:H as material, single junction and tandem solar cells

---

### 5.1 Introduction

Although *a*-Si:H is an inexpensive material for large area applications, suitable for very diverse fields, the major drawback for solar cell utilisation is its instability against light exposure or the so called Staebler-Wronski effect [3]. Intensive research since the first observation in the 1970s has resulted in more stable materials and devices through very high H<sub>2</sub> dilution, deuterium dilution and the use of multijunctions. Kobayashi has presented a cyanide treatment which passivates defects and defect precursors (such as Si-H), improving the degraded state [103].

In this chapter, the stability of *a*-SiGe:H solar cells is described. Results from the degradation of materials, single junction solar cells as well as tandem solar cells are discussed and compared with *a*-Si:H solar cells. Light soaking tests are performed on two types of materials: (1) *a*-SiGe:H (grown from SiH<sub>4</sub>+GeH<sub>4</sub>+H<sub>2</sub>) whose structure is in a mixed phase of amorphous and microcrystalline, as described in Chapter 3, and (2) *a*-SiGe:H (grown from Si<sub>2</sub>H<sub>6</sub>+GeH<sub>4</sub>+H<sub>2</sub>) which is fully amorphous. Single junction *a*-SiGe:H solar cells with several thicknesses were degraded and the results were compared with *a*-Si:H degradation. Finally, the stability of tandem solar cells is studied, with special attention to the current matching between top and bottom cells. The *a*-SiGe:H material used in these solar cells is expected to be protocrystalline. Special attention was taken to control the temperature during degradation so that it did not exceed 50 °C.

The solar cells are deposited on glass substrates coated with a transparent conducting oxide of SnO<sub>2</sub>:F (Asahi U type) and the back contact was Ag/Al. No back reflector apart from the metal was used.

### 5.2 Microscopic origin of the Staebler-Wronski effect

The Staebler-Wronski effect is a metastability phenomenon that describes the light-induced degradation in *a*-Si:H and its alloys. The main experimental observations associated with this effect are:

- A decrease in the photo- and dark-conductivity by at least one order of magnitude for *a*-Si:H [3], due to a shift of the Fermi level towards midgap and/or a decrease in the lifetime of photoexcited carriers together with a transition from the bimolecular to the monomolecular recombination.
- An increase in the density of neutral Si dangling bonds as measured by ESR [104,105], possibly due to non-radiative band-to-band recombination of photo-excited carriers rather than by the optical absorption [106].
- Structural changes locally or on a large scale [107,108], preceding the formation of metastable defects.

Some issues are still under debate:

- What type of defects are involved? The most widely accepted viewpoint is that the created defects are dangling bonds. Han et al. [109] proposed the creations of two types of dangling bonds with different kinetics to explain the different in behaviour of the optical absorption and the photo-conductivity characteristics measured during the annealing of the material. Shepard et al. [110] proposed that the energy of the created defects are distributed in gap states energies, while gap states at different energy levels play a different role during the degradation and annealing processes.
- What is the role of impurities in the defect creation? Even though the density of metastable defects increases with the concentration of impurities that are present in *a*-Si:H, samples with a low density of impurities still show degradation [111].
- Whether the increase in the defect density comes from the creation of new defects or by the change in occupancy of existing states [112]? The low rates of creation and annealing suggest that structural changes are taking place rather than a change in occupancy [1].
- What is the microscopic intrinsic model for the structure of the metastable dangling bonds? It is unclear whether the only dangling bonds created are those metastable dangling bonds with the same average distance from the H atoms as the stable dangling bonds (which would invalidate the local-H models) or the light-soaking produces two kind of dangling bonds (one identical to the measured dangling bonds plus another not detectable by ESR) [113].

Independent of the intrinsic and extrinsic mechanisms taking part in the Staebler-Wronski effect, the most widely accepted model to describe the defect creation rate is the Stutzmann-Jackson-Tsai (SJT) model [114]. The model is based on the hypothesis that the defects are created by *direct* electron-hole pair recombination. The defect creation is initiated by the non-radiative tail-to-tail recombination of an electron and a hole by which about 1.5 eV of energy is released, enough to break a weak bond and generate a defect. Assuming bi-molecular recombination statistics, as has been observed [115], the rate equation for the defect creation is

$$\frac{dN}{dt} = c_{SW} \frac{G^2}{N^2} - (N - N_0) \nu_0 e^{-\frac{E_A}{kT}} - (N - N_0) B \frac{G}{N} \quad (5.1)$$

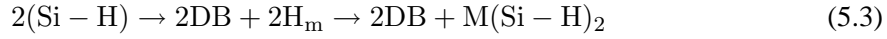
where  $N$  is the total defect density;  $N_0$  is the initial (stable) defect density;  $c_{SW}$  is a susceptibility parameter for metastable defect formation (describing the efficiency of creation of defects by bimolecular recombination);  $G$  is the generation rate of photoexcited electrons and holes;  $E_A$  is the annealing activation energy,  $\nu_0$  is a constant describing the decay of the carriers and  $B$  is a material parameter. The first term on the right-hand side describes the creation of new metastable defects by non-radiative recombination, while the second and third describes the thermal and the light-induced annealing of metastable defects, respectively. Defect creation by thermal excitation is not expected under room temperature conditions [116]. For long times the model predicts a valance between the direct recombination of the electron-hole pair (creating dangling bonds) and the recombination of the electron-hole pair through dangling bonds (with no new creation of dangling bonds). The model derives the widely observed relation:

$$N_{db}(t) \propto G^{2/3} t^{1/3} \quad (5.2)$$

Several experiments have casted doubts on the SJT model. Stradins et al. [117] have observed the  $N_{db}(t) \propto t^{1/3}$  kinetics down to 4.2 K at which dangling bonds have little influence on the photocarrier concentration. Laser-pulse experiments carried out by several groups [118,119] have shown that the degradation depends upon a second precursor which varies more slowly than the electrons and holes. Moreover, electron spin resonance (ESR) hyperfine measurements [113] do not show spatial correlation between the dangling bonds and the H atoms, excluding all the models involving local motion of H as a step in the dangling bond creation.

Branz [119] has proposed a model based on long range diffusion of H that mediates the reconfiguration of the dangling bonds (H collision model), which

accounts for the previous experimental results. For a recent overview see Ref. [120]. The model supposes Si-H sites (with density  $N_H$ ) and the mobile H (with density  $N_m$ ) as the main precursors of dangling bond (DB) creation. The recombination of the light-induced carriers generate the energy to liberate H from a Si-H sites. Mobile H,  $H_m$ , will diffuse rapidly by hopping between Si-Si sites until it is trapped at a dangling bond. When two mobile H get close to each other, they create a metastable complex,  $M(\text{Si-H})_2$ . Two dangling bonds are then created at the original Si-H where the mobile H were liberated. The reaction producing the dangling bonds is as follows



The rate equation for defect creation is

$$\frac{dN_{db}}{dt} = k_H N_H G - k_{db} N_m N_{db} \xrightarrow{\text{quasi equilibrium}} N_m N_{db} \propto G \quad (5.4)$$

$$N_m \propto \left( \frac{dN_{db}}{dt} \right)^{1/2} \quad (5.5)$$

where  $N_{db}$  is the density of dangling bonds,  $k_H$  is a proportionality constant and  $k_{db}$  is a rate constant. The model predicts that  $N_m$  will reach quasi-equilibrium rapidly with  $N_{db}$  through H emission from Si-H sites and retrapping at dangling bonds. On a more slow time scale, the dangling bonds are created by Eq. 5.3.

At present, the H collision model is going through problems to explain the degradation process in *a*-SiGe:H with Ge concentration below 20 at.%. Palinginis et al. [121] have studied the variation in the Si and Ge neutral defect densities during degradation, for *a*-SiGe:H with 7 at.% Ge fraction. They observed how Si and Ge independently do not vary in time as  $t^{1/3}$  while the total defect density follows the  $t^{1/3}$  kinetics. The relative change in the Ge versus Si defect density during degradation can not be explained considering the quasi-equilibrium between the mobile H and the total defect density (Eq. 5.4) at the same time. These results may not apply to *a*-SiGe:H with Ge concentration over 30 %, where Ge dangling bonds largely dominate in both the annealed and the degraded state [92].

Redfield [122,123] has proposed a quantitative model based on the single carrier trapping in combination with a time dependent prefactor, due to dispersive diffusion of hydrogen as a limiting structural process. The model proposes that the time dependence of generation of light-induced defects is described by the same

function as for the annealing process of the light-induced defects. This function is a stretched exponential time dependence (Eq. 5.6). This dependence is expected since there is a distribution of energies at which the defect can be created, defining a dispersive defect creation process.

$$N \propto N_0 \exp[-(t/\tau)^\beta] \quad (5.6)$$

where  $\beta$  is a dispersion parameter and  $\tau$  a relaxation time.

The participation of hydrogen in the structural relaxation of *a*-Si:H at low temperatures is likely, considering the similar relaxation behaviour observed for the case of the hydrogen diffusion. Hydrogen diffuses via a dispersive multiple trapping process (activation energy of around 1.4 eV) reaching a distance of several tenths of Angstroms (similar distances as between hydrogen atoms in the network). The hydrogen glass model [124] proposes to see the hydrogen atoms as constituents of a different sublattice in the *a*-Si:H structure. Above a certain temperature,  $T_m$ , the hydrogen atoms are mobile and mediate in thermal equilibration with dopants or defects.

Some of these processes will be discussed in more detail in the following sections.

## 5.3 Photodegradation techniques

### 5.3.1 Samples

The *a*-SiGe:H material together with the *a*-Si:H or *a*-SiGe:H single and double junction solar cells were deposited by Plasma Enhanced Chemical Vapour Deposition (PECVD) at a frequency of 13.56 MHz. Pure SiH<sub>4</sub>, Si<sub>2</sub>H<sub>6</sub> and GeH<sub>4</sub> were employed as reactive gasses and were diluted with H<sub>2</sub>. Materials were deposited on Corning glass for reflectance-transmittance, PDS and Raman scattering measurements. Aluminum coplanar contacts were deposited to measure the photo- and dark-conductivity and to perform CPM, SSPG and activation energy measurements. A crystalline silicon wafer was used as substrate for IR measurements. Single and double junction solar cells were deposited onto glass substrates coated with a transparent conducting oxide of SnO<sub>2</sub>:F (Asahi U type). Two kinds of contacts were used. On one case, silver contact followed by encapsulation of the solar cells was done. The encapsulation was done by gluing silver strips to the front and back contacts with a two component silver glue. The rest of the metal back contact was encapsulated with transparent epoxy (Norland electronic adhesive) with an approximate thickness of 0.5 mm. The glue was hardened with

ultraviolet radiation. On the case of the second type of contact a double Ag/Al back contact was used.

### 5.3.2 Light soaking conditions

Special care was taken to create uniform illumination and temperature conditions during the light soaking experiments. The illumination intensity was kept at  $90 \text{ mW/cm}^2$ ; the temperature was stable at  $50 \text{ }^\circ\text{C}$ ; the cells were degraded under open circuit conditions. The light soaking facility is described in Section 2.3.

In order to compare the degradation in an *a*-SiGe:H (*a*-Si:H) single junction with its behaviour in a tandem structure, the *a*-SiGe:H (*a*-Si:H) single junctions were degraded using a filter that simulated the top single junction in a tandem structure. A 100 nm thick *a*-Si:H layer ( $E_{opt} \sim 1.78 \text{ eV}$ ) was used as the filter in the case of *a*-SiGe:H cell, while a 110 nm thick *a*-Si:H layer made with high hydrogen dilution of silane was used ( $E_{opt} \sim 1.88 \text{ eV}$ ) for the *a*-Si:H cell. At the same time, some cells were degraded without a filter. The materials were light soaked with a red filter to obtain degradation under uniform absorption.

A detailed description of the light soaking facility can be found in Section 2.3.

## 5.4 Stability of *a*-SiGe:H as material

### 5.4.1 Introduction

The Staebler-Wronski effect is an intrinsic effect of the material, not associated with impurities [111]. It is characterised by the creation of metastable dangling bonds under illumination with photons of energy over 1.7 eV for *a*-Si:H [125], together with structural changes.

Even in the absence of a clear correlation between the film properties before and after light-soaking with the performance of a solar cell containing such a film as the *i*-layer [73], the study of the behaviour of thin films sheds light on the kinetics of the Staebler-Wronski effect.

The viewpoint that only one type of dangling bonds with a distribution of annealing energies is created due to degradation, is controversial. The hysteresis behaviour of the  $\mu\tau$  product versus the defect concentration during a process of degradation followed by annealing speaks against this viewpoint. Han et al. [109] and recently several other groups [126,127] have pointed to the creation of two kinds of defects during degradation. The second defect would be characterised by lower thermal activation energy than the neutral dangling bonds ( $D^0$ ) and would control the photo-conductivity after light soaking. The neutral dan-

gling bonds would control the changes in sub-band gap absorption. On the other hand, Stradins et al. [108] suggested the variation of the effective electron capture cross section with the microstructure of the sample and the exposure conditions. The structural changes around the defects would govern the capture coefficients.

Concomitant with the formation of defects, there are photoinduced structural changes, which could involve only a localized region around the defect [108] or all of the structure [128]. Based on the measurement of the polarized electroabsorption coefficient (caused by disorder mixing of localized and extended defects) with light soaking, Hata et al. [129] suggest that considerable disorder and strain are built up *before* the Staebler-Wronski defects appear, therefore they are not a consequence of the defect creation. The kinetics of the light induced defect creation and annealing are thus preceded by structural changes. This agrees with the observation that materials containing crystalline-like region show more stability. The crystalline regions tolerate recombination with less damage, suppressing the nonradiative recombination in the amorphous network [130]. As a result, fewer defects are created than in the more strained and disordered regions.

To enhance the stability by the improvement of the microstructure, several methods have been applied [26,131,132,133]. They have one thing in common; the material is deposited at the onset of the microcrystalline regime. This is achieved either by high dilution of the source gasses with H<sub>2</sub> or by depositing in the regime of powder formation (close to full depletion of SiH<sub>4</sub>). Sugiyama et al. [134] achieved a significant improvement in stability by replacing hydrogen with deuterium. This is due to a favorable network structure, as shown by the presence of nanometer size regions with nearly crystalline order embedded in the amorphous network [135].

Regarding the role of hydrogen, a high dilution of the gas mixture with hydrogen plays the role of passivating the dangling bonds on the growing surface, giving more time to the growing species to find favorable sites. This would form more ordered structures, as shown by the TEM micrograph of Tsu et al. [26]. They observed "linear" objects with more ordered structure than the rest of the amorphous network around them, even for *a*-Si:H with low hydrogen dilution. This supports the two-phase model of Han et al. [136].

Hydrogen would also etch the growing surface, eliminating parts of the disordered configuration comprising strained or weak bonds. Thus crystalline regions, with a lower energy configuration, would remain as building blocks in the structure. On the other hand, an excess of hydrogen would deposit microcrystalline materials in larger quantities, affecting the properties of the deposited layer due to problems associated with the presence of grain boundaries.

In conclusion, the best material is deposited under the conditions just below

the threshold of microcrystalline growth. A drawback is that microcrystals develop as the film thickness increases. This occurs earlier with higher hydrogen dilution. As shown by Koh et al. [56] the optimum strategy is to deposit the material in several steps so as to ensure that the growth process remains on the amorphous side of the amorphous-microcrystalline phase boundary while the film thickness increases.

The alloying of *a*-Si:H with Ge has several implications for the degradation process of *a*-SiGe:H materials, the most important being the relatively small Staebler-Wronski effect observed in *a*-SiGe:H materials [137] with respect to *a*-Si:H. As was mentioned before, addition of Ge into the *a*-Si:H produces a reduction of the band gap. This makes it difficult to distinguish the influence of the band gap and the Ge content on the stability of *a*-SiGe:H materials. On the one hand, Terakawa et al. [138] have observed how materials with the same band gap but different compositions degrade in a similar way. They suggest that narrower band gaps entail smaller recombination energy, which would suppress the light induced defect creation. On the other hand, while the density of Ge-like dangling bonds increases monotonically with the Ge content in the material until 40 at.%, the density of Si-like dangling bonds first increases with Ge until nearly 30 at.% Ge content and decreases continuously with further increase in Ge content, leading to a completely stable material for a Ge concentration over 40 at.% ( $E_{03} < 1.4$  eV) [75]. Stutzmann et al. [92] suggested a double effect. The increase in stability due to an increase in the density of stable dangling bonds defects with Ge content (increase in the denominator in the first term of Equation 5.1) would be counteracted by an increase in network disorder with alloying (increase in  $c_{SW}$ ) until 40 at.% Ge concentration. Beyond this concentration the disorder would not increase anymore (constant value of  $c_{SW}$ ). At this point, the degradation would be dominated by the high concentration of Ge-like dangling bonds alone. Along the same lines Cohen et al. [139,140,141] proposed that the neutral Ge-like dangling bond level in the band gap would cause a strong relaxation effect on the electrons trapped in this band. This relaxation effect may suppress the electron thermal re-emission to the conduction band, reducing the recombination with holes, and thus enhancing the lifetime of the minority carriers. The reduction in recombination by this relaxation process may be the dominant factor in determining the performance of *a*-SiGe:H devices.

The origin of the observed degradation in *a*-SiGe:H materials has to be found in the LESR results of the carriers in the Si-Si, Si-Ge and Ge-Ge bonds. Due to smaller bond energy, most of the strained Ge-Ge bonds are already broken in the annealed state. Then there would be more strained Si-Si dangling bond precursor sites in the annealed state and it is the breakage of these sites that produces the

light induced degradation [142,143]. This is in agreement with the results of Terakawa et al. who observed how the degradation kinetics depend on the band gap while the annealing process is independent of it [144]. Measuring the activation energy for the annealing of metastable defects in different band gap materials, they obtained the same value (1.2-1.3 eV), which is comparable to the activation energies for hydrogen diffusion and annealing of metastable defects in *a*-Si:H.

In this section, the stability properties against light induced degradation in materials suitable for the intrinsic layer component in a solar cell structure are studied. Several Si<sub>2</sub>H<sub>6</sub>+GeH<sub>4</sub> amorphous materials, as described in Section 3.5, are compared with a protocrystalline SiH<sub>4</sub>+GeH<sub>4</sub> material with the same band gap as described in the same Section.

#### 5.4.2 Experimental details

Three *a*-SiGe:H materials deposited on Corning glass with Al coplanar contacts were degraded. Sample A correspond to *a*-SiGe:H deposited from SiH<sub>4</sub>+GeH<sub>4</sub> feed gasses at 200 °C. The feed gasses were diluted with H<sub>2</sub> in a ratio  $f=\text{H}_2/(\text{SiH}_4+\text{GeH}_4)=80\%$ . Sample B and C correspond to *a*-SiGe:H deposited from Si<sub>2</sub>H<sub>6</sub>+GeH<sub>4</sub> feed gasses at 200 °C. The feed gasses were diluted with H<sub>2</sub> in a ratio  $f=80\%$  and  $140\%$ , respectively. All the samples were  $\sim 500$  nm thick. More details can be found in Chapter 3. The degradation experiments were performed under AM1.5 illumination conditions, keeping the temperature of the samples below 50 °C.

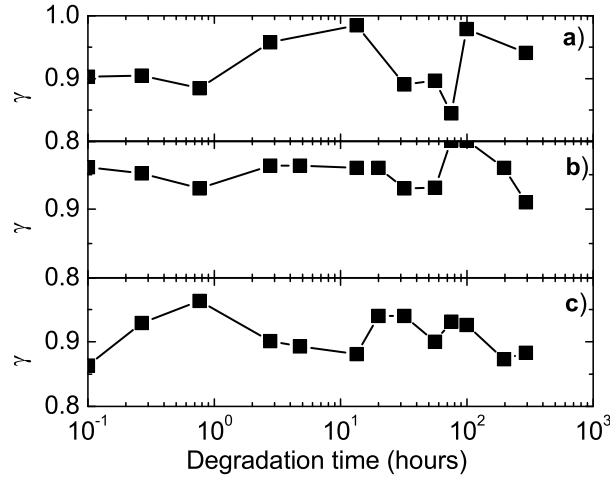
#### 5.4.3 Results and discussion

Photo-conductivity  $\sigma_P$  is the electrical conductivity when a material is exposed to light. The excess of charge carriers induced by the light generates a photocurrent. The photocurrent can be expressed as a function of the light intensity ( $F$ ) as

$$J_p \propto F^\gamma \quad (5.7)$$

where  $\gamma$  is an exponent to account for the nonlinear variations of current with light.

The photo-conductivity is controlled by the total amount of defect states between the dark Fermi level and the quasi Fermi levels. The division of the quasi Fermi levels depends on the intensity of the light. Under AM1.5 illumination the photo-conductivity will reflect the total states from midgap to the band tails, while at low light intensities (used to determine  $\gamma$ ), the photo-conductivity reflects only the defect states close to midgap. Figure 5.1a shows  $\gamma$  for sample A. Figures 5.1b



**Figure 5.1:** Evolution of  $\gamma$  during light-soaking for samples grown from a)  $\text{SiH}_4+\text{GeH}_4$  with  $f=80\%$  (sample A), b)  $\text{Si}_2\text{H}_6+\text{GeH}_4$  with  $f=80\%$  (sample B) and c)  $\text{Si}_2\text{H}_6+\text{GeH}_4$  with  $f=140\%$  (sample C).

and c show  $\gamma$  for samples B and C. The degradation in the photo-conductivity is shown in Figure 5.2 for the same samples.

No appreciable variation in  $\gamma$  with the degradation time is observed for any of the samples. On the contrary, for samples B and C the photo-conductivity measured under AM 1.5 conditions start degrading after 100 hours of light exposure. This result suggests that the defect states induced by the light are generated closer to the band tails. Cohen et al. [145] observed two defect bands inside the band gap. A shallower band (with respect to the vacuum level) related to Ge neutral dangling bonds dominates the annealed state. After degradation, a deeper band appears, which they relate to Si neutral dangling bonds. The difference observed in  $\gamma$  and  $\sigma_P$  could be explained by the preferential formation of Si dangling bonds [92], part of which would be located closer to the valence band tail.

With respect to the microcrystalline structure, samples B and C do not present signs of crystallinity formation in the Raman spectrum (not even by decomposing the spectra). Sample A shows clear crystalline transverse optical modes for Ge-Ge, Si-Ge and Si-Si bonds together with broad bands at lower frequencies indicating the presence of amorphous structure (see Fig. 3.2). Samples A and C were grown at the same deposition rate, while sample B was 2 times faster.

The degradation in the amorphous materials starts earlier than the degradation

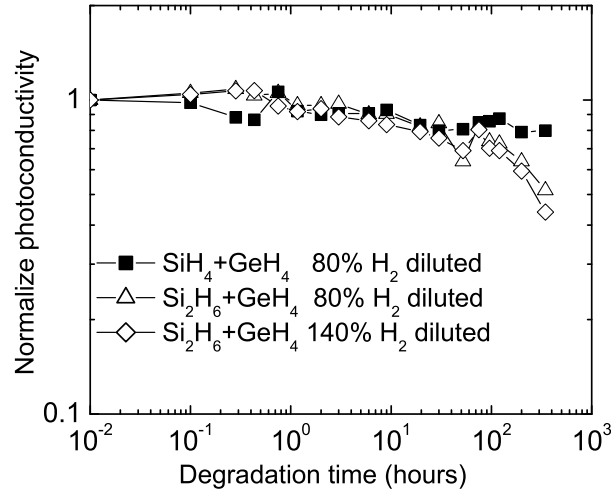


**Figure 5.2:** Evolution of  $\sigma_p$ , normalised to the as-deposited state, during light-soaking for samples grown from a)  $\text{SiH}_4 + \text{GeH}_4$  with  $f=80\%$ , b)  $\text{Si}_2\text{H}_6 + \text{GeH}_4$  with  $f=80\%$  and c)  $\text{Si}_2\text{H}_6 + \text{GeH}_4$  with  $f=140\%$ .

in the sample with a mixed phase. Between the amorphous samples, sample B with lower dilution (higher  $R_d$ ) degrades slightly slower than sample C (nearly two times higher dilution and lower  $R_d$ ). The Urbach energy stays constant at 70 meV for sample B, slightly increases from 60 to 70 meV for sample C, while for the sample with a mixed phase (A) the Urbach energy increases from 110 to 140 meV. This high value for sample A was discussed in Section 3.4.1 to be due to microcrystals embedded the amorphous network.

From these results it is clear that, the higher deposition rate obtained with  $\text{Si}_2\text{H}_6$  as feed gas presents the drawback of higher sensitivity to light induced degradation. Increasing the dilution by nearly two times reduces the deposition rate to the initial value obtained with  $\text{SiH}_4$  as feed gas, but the material is not as stable as with  $\text{SiH}_4$  as a feed gas. The higher content of H and Ge in the material deposited with  $\text{Si}_2\text{H}_6$  must be preventing the nucleation of microcrystals. Unless the conditions to deposit near the edge of microcrystallinity are set, the material obtained with  $\text{Si}_2\text{H}_6$  instead of  $\text{SiH}_4$  as feed gas will suffer from light induced degradation.

## 5.5 Stability of *a*-SiGe:H in single junction solar cell structure

### 5.5.1 Introduction

Of great importance for the photovoltaic application of *a*-SiGe:H is the stability of this material in a solar cell structure under optical excitation. The *a*-SiGe:H shows a variety of light induced instability and metastability phenomena that depend on a wide range of parameters. The complexity of the process has produced an extensive bibliography with contradictory observations.

As mentioned in the previous Section 5.4, *a*-SiGe:H as a material is expected to be rather stable under illumination [92]. Studies of the influence of the band gap on the degradation have shown how a lower band gap of *a*-SiGe:H in a solar cell structure implies higher stability [146]. Terakawa believes that the composition, such as  $C_H$  or  $C_{Ge}$ , is not the cause of the influence on the degradation, but that it is the variations in the band gap itself, mainly due to a smaller recombination energy [144]. Nevertheless, Xu et al. reported on the degradation in *a*-SiGe:H solar cells [73], and Carlson et al. observed even more degradation after long illumination times than in *a*-Si:H solar cells [147].

Several methods have been used to try to reduce the degradation in *a*-SiGe:H. Fölsch et al. [148] have investigated the degradation behaviour in solar cells with different U-type grading schemes for the i-layer. The *a*-SiGe:H was deposited at a substrate temperature of 200 °C, a pressure of  $7 \times 10^{-2}$  mbar, a rf power density of 35 mW/cm<sup>2</sup> and a dilution  $H_2:[SiH_4 + GeH_4]$  of 10:1. These conditions are representative of conditions leading to an amorphous material. Though they observed degradation for all the solar cells with different band gap grading, the degradation is reduced by a suitable design of the band gap grading. Díaz et al. [133] have studied the influence of the deposition temperature on the stability. They deposited *a*-SiGe:H material under the following conditions: substrate temperature between 150 °C to 250 °C, pressure of 0.4 mbar, rf power density of 25 mW/cm<sup>2</sup> and dilution  $H_2:[SiH_4 + GeH_4]$  of 30:1. They reported that the material deposited at temperatures above 200 °C is fully stable; they even observed an increase in the photocurrent. Vasanth et al. [90] have presented *a*-SiGe:H stable solar cells for Tauc band gaps under 1.4 eV. They observed how solar cells with higher band gaps suffer from degradation.

With respect to the source gasses, the substitution of silane as a source gas for disilane increases the deposition rate, due to the very similar decomposition rates of  $GeH_4$  and  $Si_2H_6$  [42]. Matsuda et al. [60] reported an improvement of *a*-SiGe:H alloys by using low power discharge of gas mixture  $Si_2H_6 + GeH_4$

without H<sub>2</sub> dilution. No real correlation between the replacement of SiH<sub>4</sub> for Si<sub>2</sub>H<sub>6</sub> and the degradation process has been found in the literature. The use of He instead of H<sub>2</sub> was used in some early work for technical reasons, such as the reduction of hazard. Middy et al. [61] compared the effects of H<sub>2</sub> and He dilution. H<sub>2</sub> dilution results in smaller concentration of polyhydrides (reduced porosity).

The method more widely used to date is the hydrogen dilution of the source gasses [48], in its two versions of low H<sub>2</sub> dilution and high H<sub>2</sub> dilution. The low dilution method is expected to reduced the formation of Ge-Ge clusters [149] and microstructure, which is believed to be the cause of the degradation in *a*-SiGe:H [150,151]. Terakawa et al. [152,153] attempted to obtain stable the *a*-SiGe:H solar cells by controlling the concentration of hydrogen, C<sub>H</sub>, in the material. The deposition conditions were modified to keep the optical band gap and the dilution constant. The parameter ranges were as follows: deposition temperature of 120 °C to 350 °C, pressure of 0.2 mbar, rf power density of 10 to 100 mW/cm<sup>2</sup> and dilution H<sub>2</sub>:[SiH<sub>4</sub>+ GeH<sub>4</sub>] of 2.5:1. They obtained a maximum efficiency for a C<sub>H</sub> of nearly 10%, which produces the lowest defect density and Urbach tail. On the other hand they obtained a maximum stable efficiency with the lowest C<sub>H</sub> in the material, which is the material with the lowest contribution of the IR peak at 2090 cm<sup>-1</sup> (associated with Si-H<sub>2</sub> bonding and microvoids resulting from columnar-like growth [19,46]).

A more remarkable improvement in stability comes when the medium range order in the material is increased. This is mostly achieved by embedding crystalline structures in the amorphous network [130]. Depositing at the onset of the microcrystalline regime by high H<sub>2</sub> dilution contributes to the growth of such crystalline-like nanostructures, as it has been observed in *a*-Si:H [154,131]. Shima et al. [70] and Yang et al. [155] presented more stable double and triple junction incorporating high H<sub>2</sub> dilution. One should mention the results of Koh et al. [56] for *a*-Si:H solar cells showing an improvement in stability when the i-layer is deposited in several steps to remain on the amorphous side of the amorphous-microcrystalline phase boundary while depositing the desired layer thickness.

In this section, the degradation kinetics of *a*-SiGe:H solar cells with different thicknesses, band gap profiles, substrate temperatures, source gasses and dilutions are compared. The aim is to obtain a clear picture of the degradation process in protocrystalline *a*-SiGe:H solar cells (deposited at the onset of microcrystalline formation under high dilution conditions) and compare them with solar cells made with fully amorphous silicon germanium material (under low dilution conditions or using Si<sub>2</sub>H<sub>6</sub> instead of SiH<sub>4</sub> as feed gas). A stable behaviour is expected for the material deposited with SiH<sub>4</sub> as feed gas from the results on material degradation

in the previous Section 5.4. The improvements in efficiency obtained through the band gap profile are expected not to deteriorate the stability. Finally, the degradation studies in *a*-SiGe:H deposited at low deposition temperature and with disilane as a source gas are presented and discussed.

### 5.5.2 Experimental details

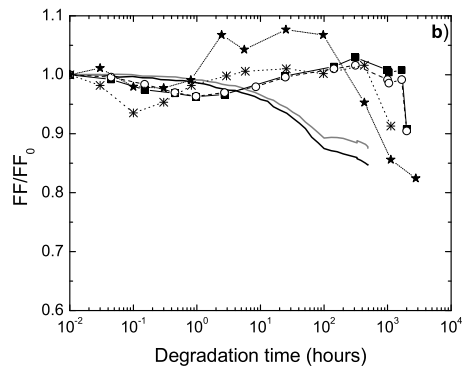
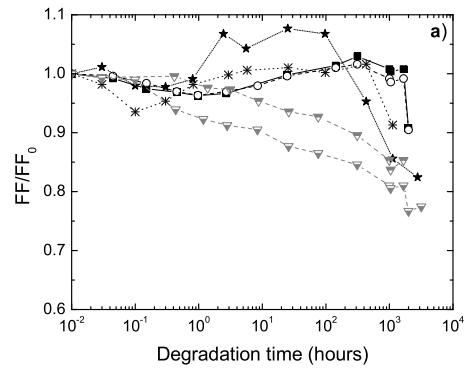
The illumination conditions under degradation are described in Section 5.3.2. Several *a*-SiGe:H solar cells with different thickness and deposition conditions were degraded and compared with two *a*-Si:H solar cells. The different thickness in the case of *a*-SiGe:H solar cells were obtained by changing the deposition time for the lowest band gap layer of the intrinsic layer. The deposition conditions were modified as described in Section 3.4.1. Protocrystalline material was obtained by adjusting the hydrogen flow. Fully amorphous material was deposited by two methods. In one case, as described in Chapter 3, *a*-SiGe:H material is amorphous when deposited under low hydrogen dilution condition of the feed gasses together with low substrate temperature. In the other case, by replacing SiH<sub>4</sub> with Si<sub>2</sub>H<sub>6</sub> as source gas, *a*-SiGe:H material grows amorphous.

The band gap profile for the *a*-SiGe:H solar cells consists of a U-shape profile of a front grading of 10 nm, a constant band gap layer of 75 nm, 85 nm or 95 nm and a back grading of 40 nm. Three *a*-SiGe:H solar cells were degraded under AM 1.5 conditions filtered with a 100 nm thick *a*-Si:H layer ( $E_{opt} \sim 1.78$  eV) that simulate the top cell in a *a*-Si:H/*a*-SiGe:H tandem structure.

When both the top and the bottom cells are *a*-Si:H, the top cell is deposited with hydrogen dilution of the silane gas. In this case the *a*-Si:H top cell has a thickness of 110 nm and a band gap of 1.88 eV. To match the top and the bottom photogenerated current the bottom cell has a thickness of 500 nm. An *a*-Si:H solar cell of 500 nm thick has been degraded under AM 1.5 conditions filtered with an *a*-Si:H film that matches the characteristics of the top cell in the *a*-Si:H/*a*-Si:H tandem structure. To compare *a*-Si:H and *a*-SiGe:H solar cells with the same initial efficiency under AM 1.5, a thinner *a*-Si:H solar cell has been degraded and compared with the *a*-SiGe:H solar cell degraded under AM 1.5 conditions. The cells were light soaked in open circuit conditions.

### 5.5.3 Results and discussion

The evolution of the normalised FF during light exposure is shown in Figure 5.3. Figure 5.3a compares the *a*-SiGe:H solar cells deposited at the onset of microcrystalline formation with *a*-Si:H solar cells. Figure 5.3b compares the same protocrystalline *a*-SiGe:H solar cells as before with fully amorphous silicon ger-



**a-SiGe:H**  
Protocrystalline

Filtered light

—■— 75 nm  $FF_0 = .52$

---○--- 85 nm  $FF_0 = .50$

—\*— 95 nm  $FF_0 = .48$

AM 1.5

—★— 85 nm  $FF_0 = .50$

**a-SiGe:H**  
Amorphous  
AM 1.5

— SiH<sub>4</sub>+GeH<sub>4</sub> gasses

$FF_0 = .51$

— Si<sub>2</sub>H<sub>6</sub>+GeH<sub>4</sub> gasses

$FF_0 = .54$

**a-Si:H**  
Amorphous

Filtered light

--▽-- 500 nm  $FF_0 = .67$

AM 1.5

--▽-- 220 nm  $FF_0 = .67$

**Figure 5.3:** Evolution of the FF normalised to the as-deposited state of three a-SiGe:H solar cells with different thickness of the lower band gap layer in the i-layer. The thickness of front plus back grading is 50 nm. Two references a-Si:H solar cell are plotted as references. a) Protocrystalline a-SiGe:H versus a-Si:H. b) Protocrystalline a-SiGe:H versus a-SiGe:H.

manium solar cells grown with a mix of  $\text{SiH}_4+\text{GeH}_4$  or  $\text{Si}_2\text{H}_6+\text{GeH}_4$  as source gasses. The initial fill factor ( $\text{FF}_0$ ) is measured on the as-deposited solar cell, with no previous annealing. For comparison, an *a*-SiGe:H solar cell under AM 1.5 illumination is plotted together with the solar cells light soaked with filtered light. The two *a*-Si:H solar cells suffer from a pronounced degradation compared with the *a*-SiGe:H solar cells. Although the light intensity is higher (without the filter) during the degradation in the thin *a*-Si:H solar cell this cell degrades less than the thicker cell. The enhancement in the electric field in the bulk of the solar cell is achieved by reducing the thickness of the intrinsic layer, which reduces the extra recombination processes that originate during the light-induced formation of defects.

All the protocrystalline *a*-SiGe:H solar cells show a high stability against light induced degradation for a period of 1000 hours, under the conditions applicable for a tandem structure i.e. under filtered illumination. For the thickness range under study no difference in the degradation behaviour is found. The stability is confirmed in the investigation of the carrier collection length, as shown in Figure 5.4, where the ratio of the carrier collection length over the thickness of the solar cell is represented. As has been discussed in Section 4.3, the FF is very sensitive to the variation in internal recombination. As expected, the internal electric field in the i-layer is reduced as the thickness increases. The decrease in the electric field creates internal regions where recombination is more likely to take place. This is reflected in a lower initial FF as the thickness increases. The same weakening of the electric field causes the reduction in the initial  $L_c/W$  with the thickness.

In Chapter 3 the deposition conditions leading to formation of microcrystals in *a*-SiGe:H material were studied. The influence of the  $\text{H}_2$  dilution and the substrate temperature on the growth of microcrystals were shown. At the same time, the formation of microcrystals was observed to increase with the thickness of the deposited film, for the right deposition conditions. We speculate that the *a*-SiGe:H material deposited under these conditions, with an appropriate thickness, exhibits an improvement in the medium range order, which improves the stability of the material. Figure 5.3b shows the degradation results for several *a*-SiGe:H solar cells. In this figure, solar cells are represented deposited at the onset of microcrystalline formation, with different thickness of the i-layer. In the same figure, two fully amorphous silicon germanium solar cells are also plotted. The deposition conditions for the *a*-SiGe:H material used in these fully amorphous solar cells were such that the *a*-SiGe:H material did not exhibit crystalline transverse optical modes in the Raman spectroscopy measurements even for a thickness of 500 nm and substrates temperatures of 200 °C. A mix of  $\text{SiH}_4+\text{GeH}_4$

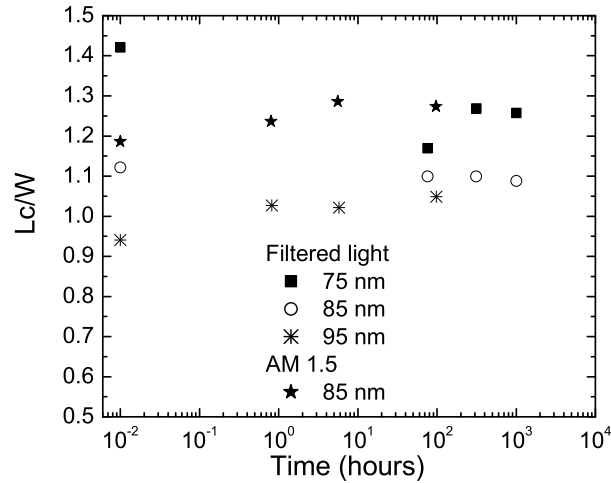


**Figure 5.4:** Evolution of the carrier collection normalised to the thickness of the film three *a*-SiGe:H solar cells with different thickness of the lowest band gap sublayer in the *i*-layer.

gasses was used for one of the fully amorphous solar cells, deposited at a substrate temperature of 170 °C and 65 % hydrogen dilution. The second fully amorphous solar cell was deposited with  $\text{Si}_2\text{H}_6 + \text{GeH}_4$  as the source gasses, with a  $T_s$  of 200 °C and 80 % hydrogen dilution. The fully amorphous silicon germanium solar cells exhibit clear sensitivity to light exposure, in contrast to the solar cells in which the intrinsic layer is protocrystalline. The protocrystalline solar cells exhibit high stability against light induced degradation, confirmed from the degradation studies in several solar cells.

A more careful study on the performance of the FF during illumination for protocrystalline solar cells shows, as a standard trend, an initial decrease in the FF that is followed by a rise, normally to values higher than the initial value. Finally, a sharp drop in FF is observed after 1000 hours of light soaking for the solar cells under filtered illumination. This on-set time of FF collapse is shorter for the solar cell under AM 1.5 illumination, and depends on the thickness of the *i*-layer. The sharp drop is correlated with a strong increase in the series resistance of the cells. The annealing of the cells was not possible due to the bad state of the contacts. Several reasons could be considered to explain this sudden drop and its dependence on illumination conditions. The high intensity white light could

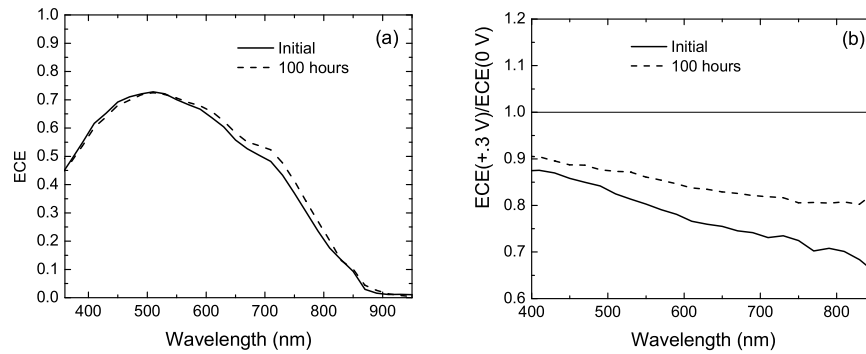


**Figure 5.5:** Variation of (a) the spectral response (ECE) and (b) the ratio  $ECE(+0.3 \text{ V})$  to  $ECE(0 \text{ V})$  of an *a*-SiGe:H cell as a result of 100 hours light soaking time (white bias). The *a*-SiGe:H solar cell of 135 nm thickness degraded under AM 1.5 is represented.

damage the n-*a*-Si:H/Ag contact more rapidly than the filtered light. The stress on the contact may be increased by the encapsulation glue due to the local heat produced by the high intensity light. The most probable reason is failure of the back contact. Other effects have been reported in the literature. An ultra-violet (UV) degradation of the  $\text{SnO}_2/\text{p-}a\text{-SiC:H}$  interface could produce similar effects. Mandracci et al. [156] reported on the degradation in very thin *a*-Si:H devices, for UV detectors of only 20 nm thickness, exposed to 365-nm light, confirming the influence of the interface degradation.

The consistent behaviour of the FF for protocrystalline solar cells before the strong increase in series resistance could be explained by initial light induced degradation followed by a stable equilibrium between defect creation and defect annealing by light (third term in Equation 5.1). The improvement in the FF with light soaking is confirmed by spectral response measurements, which show a consistently increase in the collection in the red part of the spectrum (Figure 5.5a). The improvement is more pronounced under forward bias, as shown in Figure 5.5b. In Fig. 5.5 the *a*-SiGe:H solar cell of 135 nm thickness degraded under AM 1.5 conditions is represented.

Question arises from these inverse SW effect results. Is this a typical process for *a*-SiGe:H material made with high  $\text{H}_2$  dilution of source gas? In his study about the effect of the intrinsic layer thickness on the degradation kinetics of *a*-Si:H p-i-n solar cells with *a*-Si:H i-layer made with low  $\text{H}_2$  of silane, Munyeme [98] observed, *only for thin i-layers (100 nm)*, an initial reduction of the FF in the

first hour of degradation followed by a constant increase during the next tenths of hours before the degradation process started to dominate. Besides, Cabarrocas et al. [157] reported a similar behaviour for polymorphous silicon p-i-n solar cells thinner than 450 nm under high intensity red light illumination. Their polymorphous silicon is characterised by a low initial defect density ( $\sim 2 \times 10^{16} \text{cm}^{-3}$ ).

To find a plausible explanation for this effect in these diverse materials and in cells with different thicknesses, the following processes must be taken into account. First, the defect density in *a*-Si:H deposited with low H<sub>2</sub> dilution of silane increases with light soaking. In *a*-SiGe:H the density of stable (as deposited) as well as metastable (light-induced) Si-like dangling bonds decreases with increasing Ge concentration. Then, the degradation behaviour should be dominated by the high Ge-like dangling bond density alone, or at least until the light induced Si-like dangling bond density exceeds that of Ge-like dangling bonds. The behaviour of the thinner *a*-Si:H solar cell compared with the *a*-SiGe:H solar cell, where the inverse Staebler-Wronski effect is observed, would be explained by the higher defect creation in the *a*-Si:H material. If the amount of defects in the *a*-Si:H solar cells created by illumination increases with the thickness of the solar cell, a thinner solar cell than in the *a*-SiGe:H case is needed to keep the electric field in the bulk of the i-layer and to observe a more stable behaviour against the Staebler-Wronski effect, similar than for *a*-SiGe:H material. The defect density in the polymorphous material is lower than in *a*-Si:H as reported in reference [158]. This induces a smaller screening of the internal electric field, allowing a thicker solar cell. The process that counteracts the defect generation by light soaking may be found in the intrinsic material itself (thermal or light induced annealing) or in the response of the interfaces to the light soaking process. The degradation temperature in this study is 50 °C, similar to Munyeme's procedure. This is a quite low temperature to allow annealing even when it is applied for long periods of degradation. Roca i Cabarrocas performed high intensity degradation at 80 °C for periods of 30 hours. On the other hand, light soaking of p-*a*-SiC:H layers may result in the activation of boron, which improves the doping efficiency and therefore should increase the internal electric field in the intrinsic layer. This will act together with light annealing of defects to compensate the shielding of the electric field by the creation of metastable defects.

The case of *a*-SiGe:H has been further studied by computer simulation with the program D-AMPS. The details about the solar cell structure and the simulation parameters are discussed in Chapter 4. The inverse Staebler-Wronski effect is more pronounced for the solar cell degraded under AM 1.5 illumination than for the solar cells degraded using filtered light. The following simulation results are based on two assumptions. First, the inhomogeneous absorption of the light, for

the first case, induces an inhomogeneous defect creation with the thickness of the solar cell. Second, only the *a*-SiGe:H material with higher band gap (low alloyed) used for the front grading and the intrinsic *a*-Si:H material in the front buffer are sensitive to light induced degradation. The *a*-SiGe:H material in the back grading and the back buffer degrade less in a given time. The first assumption is based on the wide wavelength spectrum of the sun and the dependence of the absorption coefficients on the wavelength for the various materials in the solar cell. The second assumption is based on the results presented in Section 5.4. The stability against light soaking for the protocrystalline *a*-SiGe:H material with a band gap of 1.5 eV was demonstrated. We assume that when the band gap is increased by reducing the Ge content, the material degrades faster [138]. When the Ge flow decreases, the material is deposited closer to the crystalline regime, due to a higher H<sub>2</sub> dilution. Although the front grading must be amorphous material (due to the small thickness of the layers and because it was deposited on intrinsic *a*-Si:H material), the back grading shows crystalline structures by Raman spectroscopy. The same band gap profile for the i-layer used in the solar cell was deposited on a Corning glass to perform Raman scattering measurements. The vibrational modes observed are TO resonance modes of crystalline Si-Si, Si-Ge and Ge-Ge bonds. Due to the presence of the small amount of microcrystalline structure and the lower light intensity reaching the back of the cell, the graded part of the cell in the back will degrade less than the front graded part.

After 1 hour of degradation, the  $V_{oc}$  and the  $J_{sc}$  show a value lower than the as-deposited initial state, after which they remain constant until the failure of the contacts. This step coincides with the increase in FF. Figure 5.6 shows the variation of the  $V_{oc}$ ,  $J_{sc}$ ,  $\mu$  and FF for the same cell as presented in Figure 5.5. This solar cell was degraded under AM 1.5 conditions.

Following the previous assumptions, the increase in defect density during degradation is implemented in the computer simulation only for the front and back buffers and for the first two front and back grading layers. The increase in the defect density was profiled from the front (higher) to the back (lower) of the solar cell. Limited by the computer code, the increase in defect density during degradation was simulated by increasing the width of the defect pool. At the same time, the characteristic energy of valence band tail was sharper to maintain a uniform distribution of defects (characteristic of an intrinsic material) through the band gap. A second suitable method was to shift the defect pool position closer to mid gap and modify again the characteristic energy of the valence band tail to maintain a uniform distribution of defects through the band gap.

The Fermi level, previously closer to the conduction band, is shifted towards mid gap in the rear part of the solar cell when the defect density is increased near

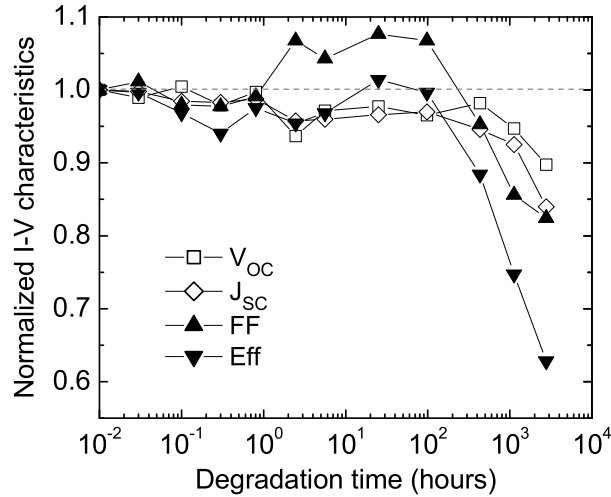


**Figure 5.6:** Variation of normalised I-V characteristics for the *a*-SiGe:H solar cell degraded under AM 1.5 conditions. The characteristics are normalised to the as-deposited state.

the *i/n* junction (high band gap region). This reduces the recombination there where new defects were not created (for example the low band gap region at the back of the solar cell which does not suffer from degradation), enhancing the red response as is observed experimentally (Fig. 5.5a). The defects generated by degradation are negatively charged (lying below the Fermi level, which is above mid gap). The screening of the electric field by the negative charges reduces the overall I-V characteristics. On the other side, near the *p/i* junction both methods shift the Fermi level from near the valence band toward mid gap. The shift of Fermi level is extended deeper in the intrinsic layer causing a higher recombination process. The defects created are positively charged (the Fermi level is below mid gap). The material degradation at the *p/i* junction results in a general deterioration of all the I-V characteristics parameters.

None of the previous methods provide agreement with the experimental increase in FF and  $\eta$  together with a deterioration of the  $V_{OC}$  and  $J_{SC}$ . Only with the presence of negatively charged states near the *p/i* junction it is possible to simulate the experimental results. The defect states closer to the valence band enhance the electric field in the bulk of the intrinsic layer, increasing significantly the FF and to a lesser extent the  $\eta$ . At the same time, the excess of recombination near the *p/i*

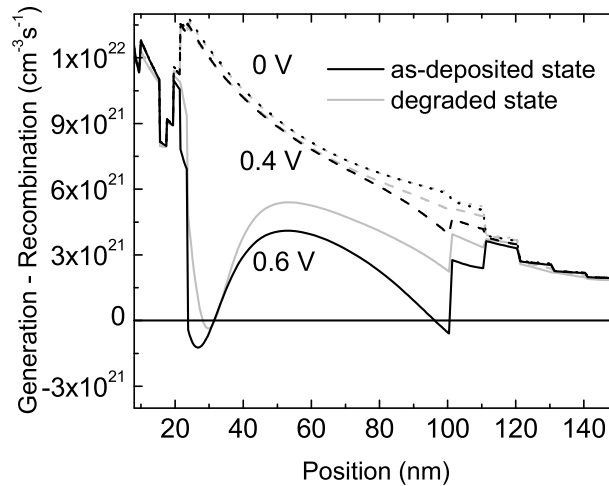


**Figure 5.7:** Computer simulation of sample from Fig. 5.5. Generation ( $G$ ) minus spatial recombination ( $R$ ) rates for the 'U-shape' structure under different bias conditions (AM 1.5) in the as-deposited state against the degraded state. Computer simulations of the sample from Fig 5.6.

junction reduces the  $J_{sc}$  and the  $V_{oc}$ .

In summary, the most probable mechanisms that takes place during light soaking are an activation of boron, which improves the doping efficiency or boron diffusion from the p-layer to the front buffer and first layers of the front grading. In both cases, degradation in the front and back buffer and the material with higher band gap in the i-layer may be taking place at the same time. Figure 5.7 shows the recombination current (generation minus recombination rates) for a simulated solar cell implementing boron doping in the front buffer and defect state increase at the buffers and the first (last) layers of the front (back) grading. An improvement in the collection is observed in the rear part of the i-layer, becoming more significant at higher forward bias, in agreement with the measurements of Figure 5.5b (the spectral response ratio of positive bias voltage to zero bias voltage). The application of these mechanisms improves the performance of the stable *a*-SiGe:H solar cell.

For the solar cells degraded under filtered light, the same discussion can be applied with smaller variations in the I-V characteristics due to the lower intensity of the light. In the experimental degradation time presented here, the initial

degradation in the material at the junctions appears to be stable. Longer exposure time could further degrade the material at the junctions with negative effects. This result opens new ways to design profiles that are more stable against degradation.

The initial degradation in the material close to the p/i and i/n junction seems to be responsible for the steep decrease in the  $V_{oc}$  and  $J_{sc}$  and the improvement of the FF and  $\eta$ .

## 5.6 Stability of *a*-SiGe:H in a tandem solar cell structure

### 5.6.1 Introduction

Multi-junction solar cells are expected to relieve the degradation in efficiency during light exposure [159]. The thickness of each photovoltaic layer is thinner than for single-junction solar cells, and a rather strong electric field prevents carrier recombination and maintains a higher FF after illumination. However, in addition to the cell structure the stability of the materials themselves must also be improved.

To obtain a high performance multijunction solar cell the component cells should have a high efficiency and stability. Even when this is achieved, the degradation in the resulting multijunction could present unexpected kinetics. Yang et al. [160] have studied the effect of the band gap variation and the current mismatching on the stability of tandem devices. From their analysis they concluded that in order to obtain a higher stabilized efficiency, the single junction cell with the higher efficiency (until now the top *a*-Si:H) should limit the current of the complete tandem solar cell. The amount of mismatch depends on the performance of the lower efficiency single junction.

In this section the implementation of the stable *a*-SiGe:H materials and single junctions in tandem solar cells is explored and discussed. Comparison with *a*-Si:H/*a*-Si:H tandem solar cell is presented.

### 5.6.2 Experimental details

Several *a*-Si:H/*a*-SiGe:H tandem solar cell structures were deposited in a p-i-n/p-i-n configuration with silver as back contact. The top solar cell is made of *a*-Si:H material deposited under low  $H_2$  dilution conditions with a band gap of 1.78 eV and thickness of 100 nm. The *a*-SiGe:H bottom cell consists of the single junction protocrystalline solar cell presented in the previous section with a thickness of 85 nm for the lowest band gap layer of the intrinsic layer (in total 135 nm). As a reference, an *a*-Si:H/*a*-Si:H tandem with the same p-i-n/p-i-n configuration is used. In this case the *a*-Si:H top single junction is made at low substrate temperature

and high  $H_2$  dilution ( $E_g$  of 1.88 eV) with a thickness of 110 nm. The bottom single junction of the  $a$ -Si:H/ $a$ -Si:H tandem cell is made of the same conditions as the  $a$ -Si:H top single junction  $a$ -Si:H/ $a$ -SiGe:H tandem cell, with a thickness of 500 nm. In both the cases the thicknesses are such that the top and bottom short circuit currents are matched.

### 5.6.3 Results and discussion

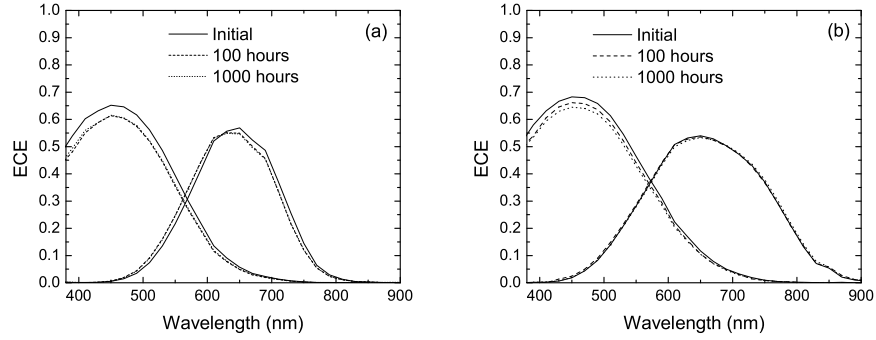
Table 5.1 shows the evolution of the short circuit current for both the top and the bottom components of the studied tandem solar cells. The  $J_{sc}$  is obtained from the SR measurement shown in Figure 5.8. One observes that in both the tandem solar cells the top single junction suffers from strong degradation. In the case of the  $a$ -Si:H/ $a$ -SiGe:H tandem solar cell the  $a$ -SiGe:H bottom cell does not show signs of photodegradation. This is in agreement with the results obtained in single  $a$ -SiGe:H junctions. The higher stability of the tandem solar cells with an  $a$ -SiGe:H bottom cell is obvious from the evolution of the FF presented in Figure 5.9. The FF in a tandem structure depends on the ratio  $J_{sc}^{top} / J_{sc}^{bot}$ . For ratios lower than 1 the top cell is generating less current than the bottom, and thus limiting the tandem  $J_{sc}$ . The recombination processes in the top cell will determine the losses of  $J_{sc}$  and thus the FF. The contrary is valid for ratios greater than 1. For ratios close to unity, none of the cells is limiting the  $J_{sc}$  so that the current is a combination of both. The resulting FF will be an intermediate value between the FF of the top and the bottom cell. When one of the cells has a lower FF, then the cell with the better FF is deliberately made limiting.

The importance of current matching between the top and the bottom cell becomes more significant during degradation. During degradation, the increase in photo-generated defects especially reduces the FF of the tandem cell and to some degree the  $J_{sc}$ . When selecting a cell to limit the  $J_{sc}$  of the tandem, special attention must be taken regarding its stability. With the development of better  $a$ -SiGe:H material (see Chapter 3) the FF can be higher than the FF of  $a$ -Si:H solar cell during degradation. For example,  $a$ -SiGe:H deposited at low substrate temperature shows a FF~0.66, while after 200 hours of degradation a 150 nm thick  $a$ -Si:H solar cell shows a variation from FF~0.7 to 0.65 [98]. At the same time, the less stable cell will become the limiting cell as its  $J_{sc}$  decreases during degradation. Thus, to reduce the Staebler-Wronski effect in the tandem solar cells presented here it is not enough to make the more stable bottom cell the limiting cell, but the  $a$ -Si:H top cell must become more stable against light soaking.

From the previous analysis, one can observe that the stability of the tandem solar cell is improved by using stable single junction components. In this case,

**Table 5.1:** Top and bottom  $J_{sc}$  measured by SR in the initial state and after 1000 hours of light soaking under AM 1.5.

Sample	State	$J_{sc}$ (mA/cm <sup>2</sup> )
		top/bottom
<i>a</i> -Si:H/ <i>a</i> -SiGe:H	Initial	8.11/8.72
	1000 h	7.49/8.75
<i>a</i> -Si:H/ <i>a</i> -Si:H	Initial	6.92/6.72
	1000 h	6.38/6.63

**Figure 5.8:** Spectral response of (a) *a*-Si:H/*a*-Si:H and (b) *a*-Si:H/*a*-SiGe:H tandem cell for different light soaking time

a thick bottom cell constituted of *a*-Si:H material, which has degradation kinetics proportional to its thickness, is replaced with a more stable material such as *a*-SiGe:H.

## 5.7 Conclusions

In this chapter, the incorporation of protocrystalline *a*-SiGe:H material in single junction and tandem solar cell structures was presented. A study of the stability under light-soaking conditions of *a*-SiGe:H as a material and in different device configurations was carried out. In Chapter 3 it was demonstrated that under certain deposition conditions, *a*-SiGe:H evolves in crystalline phase formation. It was shown how this phase grows with the thickness of the layer. For  $\text{SiH}_4 + \text{GeH}_4$

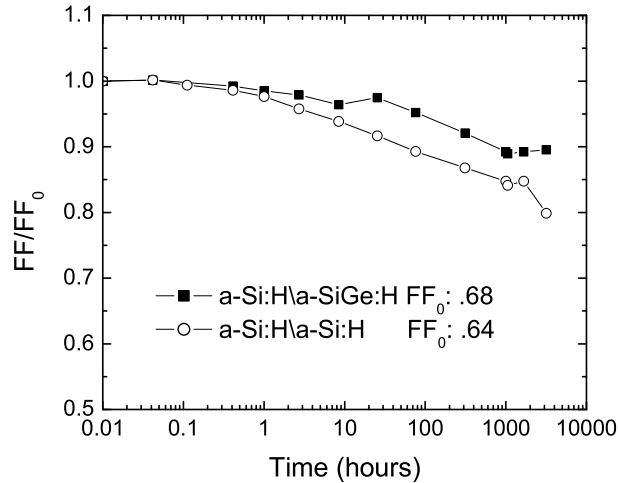


**Figure 5.9:** Evolution of the normalised FF of *a*-Si:H/*a*-SiGe:H solar cell compared with *a*-Si:H/*a*-Si:H with degradation time. The FF is normalised to the as-deposited state.

as the feed gasses, a substrate temperature of 200 °C and an hydrogen dilution of 80 % the material changes from being amorphous (at 100 nm thickness) to exhibiting crystalline transverse optical modes in the Raman spectrum (at 500 nm thickness). In contrast to this, when SiH<sub>4</sub> is replaced with Si<sub>2</sub>H<sub>6</sub> no change of phase was observed. The degradation experiments have shown how fully amorphous silicon germanium deposited from Si<sub>2</sub>H<sub>6</sub> suffers from photo-conductivity degradation while *a*-SiGe:H material with a mix of amorphous and crystalline phase is stable during 500 hours of light exposure. As mentioned before, a thinner film has no appreciable crystalline modes in the Raman spectrum. It is this thin film which is used in the solar cell structure. Comparing the degradation in several solar cells with protocrystalline intrinsic layer against *a*-Si:H and fully amorphous silicon germanium solar cells, it was demonstrated that protocrystalline *a*-SiGe:H behaves stable as a material in the solar cell structure during 1000 hours of the light soaking experiments. Moreover, when implemented in a tandem solar cell, it was shown by spectral response measurements that the top cell is responsible for the degradation of the tandem cell while the bottom cell remained stable. As a conclusion, the stability of *a*-SiGe:H deposited at the onset of microcrystalline formation has been demonstrated. At the same time, the advantage of higher depo-

sition rates obtained by replacing  $\text{SiH}_4$  with  $\text{Si}_2\text{H}_6$  has the drawback of suffering from larger instability. More experiments are needed to find the conditions for remaining in a protocrystalline phase at higher deposition rates.



## References

---

- [1] R. A. STREET, *Hydrogenated amorphous silicon* (Cambridge University Press, Cambridge, 1991).
- [2] S. M. SZE, *Physics of semiconductor devices* (John Wiley & Sons, New York, 1981).
- [3] D. STAEBLER and C. WRONSKI, *Appl. Phys. Lett.* **31**, 292 (1977).
- [4] J. TAUC, *Amorphous and liquid semiconductors* (Plenum Press, London, 1974).
- [5] A. MADAN, P. RAVA, R. SCHROPP, and B. VAN ROEDERN, *Appl. Surf. Sci.* **70/71**, 716 (1993).
- [6] R. SCHROPP, K. FEENSTRA, E. MOLENBROEK, H. MEILING, and J. RATH, *Phil. Mag. B* **76**, 309 (1997).
- [7] L. BALAGUROV, Y. DROZDOV, N. KARPOVA, O. KOROBV, A. LUPACHEVA, E. OMEL'YANOVSKIĀ, A. ORLOV, and T. UKHORSKAYA, *Sov. Phys. Solid State* **31**, 1783 (1990).
- [8] V. VORLÍČEK, M. ZÁVĚTOVÁ, S. PAVLOV, and L. PAJASOVÁ, *J. Non-Cryst. Solids* **45**, 289 (1981).
- [9] R. KALZES, M. VAN DEN BROEK, J. BEZEMER, and S. RADELAAR, *Phil. Mag. B* **45**, 377 (1982).
- [10] Y. HISHIKAWA, N. NAKAMURA, S. TSUDA, S. NAKANO, Y. KISHI, and Y. KUWANO, *Jpn. J. Appl. Phys.* **30**, 1008 (1991).
- [11] R. STREET, *Phys. Rev. B* **43**, 2454 (1991).
- [12] K. PIERZ, W. FUHS, and H. MELL, *Phil. Mag. B* **63**, 123 (1991).
- [13] W. LUFT and Y. SIMON TSUO, *Hydrogenated amorphous silicon deposition processes* (Marcel Dekker, Inc., New York, 1974).
- [14] A. ROSE, *Concepts in photoconductivity and allied problems* (Krieger, New York, 1978).
- [15] K. F. FEENSTRA, *Hot-wire chemical vapour deposition of amorphous silicon and the application in solar cells*, Ph.D. thesis, Utrecht University, the Netherlands, 1998.
- [16] M. BRODSKY, M. CARDONA, and J. CUOMO, *Phys. Rev. B* **16**, 3556 (1997).
- [17] A. LANGFORD, M. FLEET, B. NELSON, W. LANFORD, and N. MALEY, *Phys. Rev. B* **45**, 13367 (1992).

- [18] M. SHIMA, A. TERAKAWA, M. ISOMURA, M. TANAKA, and S. TSUDA, in *13th European PV. Solar Ener. Conf.* (Conference Proceedings, Nice, France, 1995), p. 269.
- [19] J. DAEY OUWENS, R. SCHROPP, and W. VAN DER WEG, *Appl. Phys. Lett.* **65**, 204 (1994).
- [20] M. ALONSO and K. WINER, *Phys. Rev. B* **39**, 10056 (1989).
- [21] J. LANNIN, *Phys. Rev. B* **16**, 1510 (1977).
- [22] L. YANG, J. NEWTON, and B. FIESELMANN, in *Amorphous and Heterogeneous Silicon-Based Films—1989* (Materials Research Society, Warrendale, 1989), Vol. 149, p. 497.
- [23] J. BURDICK and T. GLATFELTER, *Sol. Cells* **18**, 301 (1986).
- [24] P. BASORE, *IEEE Trans. Electron Devices* **37**, 337 (1990).
- [25] A. GORDIJN, Stability of Hydrogenated Amorphous Silicon Germanium Solar Cells, M.Sc Thesis, Utrecht University, the Netherlands, 2000.
- [26] D. TSU, B. CHAO, S. OVSHINSKY, S. GUHA, and J. YANG, *Appl. Phys. Lett.* **71**, 1317 (1997).
- [27] J. SCHMITT, *J. Non-Cryst. Solids* **59&60**, 649 (1983).
- [28] J. DOYLE, D. DOUGHTY, and A. GALLAGHER, *J. Appl. Phys.* **71**, 4727 (1992).
- [29] A. MATSUDA, *J. Non-Cryst. Solids* **59-60**, 767 (1983).
- [30] G. GANGULY and A. MATSUDA, *J. Non-Cryst. Solids* **164-166**, 31 (1993).
- [31] P. VIGNERON, P. P.W., and R. J., in *Amorphous and Heterogeneous Silicon-Based Films—2003* (Materials Research Society, Warrendale, 2003), Vol. 762, p. A9.2.
- [32] K. WINER, *Phys. Rev. B* **41**, 12150 (1990).
- [33] N. HATA, S. WAGNER, P. ROACA I CABARROCAS, and M. FAVRE, *Appl. Phys. Lett.* **56**, 2448 (1990).
- [34] R. BANERJEE, S. RAY, N. BASU, A. BATABYAL, and A. BARUA, *J. Appl. Phys.* **62**, 912 (1987).
- [35] B. SCOTT, J. REIMER, and P. LONGEWAY, *J. Appl. Phys.* **54**, 6853 (1983).
- [36] R. ROSS and J. JAKILK, *J. Appl. Phys.* **65**, 3785 (1984).
- [37] G. STUTZIN, A. OSTROM, R.M. GALLAGHER, and D. TENENBAM, *J. Appl. Phys.* **74**, 91 (1993).
- [38] P. ROCA I CABARROCAS, S. HAMMA, S. SHARMA, G. VIERA, E. BERTRAN, and J. COSTA, *J. Non-Cryst. Solids* **227-230**, 871 (1998).
- [39] L. BUOFENDI and BOUCHOULE, *Plasma Sources Sci. Technol.* **3**, 262 (1994).
- [40] J. PERRIN, J. SCHMITT, G. DE ROSNY, B. DREVILLON, J. HUC, and A. LLORET, *Chem. Phys.* **73**, 383 (1982).

- [41] J. PERRIN and J. AARTS, *Chem. Phys.* **80**, 351 (1983).
- [42] H. CHATHAM and P. BHAT, in *Amorphous Silicon Technology*, edited by M. J. MADAN, A. THOMSON, P. C. TAYLOR, P. G. LECOMBER, and Y. HAMAKAWA (Materials Research Society, Pittsburgh, 1988), Vol. 118, p. 31.
- [43] M. KUSHNER, *J. Appl. Phys.* **62**, 2803 (1987).
- [44] E. AUSTIN and F. LAMPE, *J. Phys. Chem.* **81**, 1134 (1977).
- [45] A. MATSUDA, K. YAGII, M. KOYAMA, T. M., Y. IMANISHI, N. IKUCHI, and K. TANAKA, *Appl. Phys. Lett.* **47**, 1061 (1985).
- [46] J. YANG, L. CHEN, and A. CATALANO, in *Amorphous Silicon Technology*, edited by P. T. Y. H. A. MADAN, M.J. THOMPSON and P. LECOMBER (Materials Research Society, ADDRESS, 1991), Vol. 219, p. 259.
- [47] V. DALAL, S. KAUSHAL, J. XU, and K. HAN, In: *Proc. of First World Photovolt. Spec. Conf., Hawaii* 464 (1984).
- [48] A. MATSUDA, M. KOYAMA, N. IKUCHI, Y. IMANISHI, and K. TANAKA, *Jpn. J. Appl. Phys.* **25**, L54 (1986).
- [49] K. TACHIBANA, *Jpn. J. Appl. Phys.* **33**, 4329 (1994).
- [50] G. GANGULY and A. MATSUDA, *J. Non-Cryst. Solids* **198-200**, 559 (1996).
- [51] S. HAZRA, A. MIDDYA, and S. RAY, *J. Non-Cryst. Solids* **202**, 81 (1996).
- [52] X. XU, J. YANG, and S. GUHA, *J. Non-Cryst. Solids* **198-200**, 60 (1996).
- [53] K. TANAKA and A. MATSUDA, in *Amorphous and Heterogeneous Silicon-Based Films—1986* (Materials Research Society, Warrendale, 1986), Vol. 70, p. 245.
- [54] A. CATALANO, R. ARYA, M. BENNETT, L. YANG, J. MORRIS, B. GOLDSTEIN, B. FIESELMANN, J. NEWTON, and S. WIEDEMAN, *Sol. Cells* **27**, 25 (1989).
- [55] C. FORTMANN, In: *Proc. of 21<sup>st</sup> Photovolt. Spec. Conf., Kissimmee, FL* 1493 (1990).
- [56] J. KOH, Y. LEE, H. FUJIWARA, C. WRONSKI, and R. COLLINS, *Appl. Phys. Lett.* **73**, 1526 (1998).
- [57] S. GUHA, X. XU, and J. YANG, *Appl. Phys. Lett.* **66**, 595 (1995).
- [58] A. TERAKAWA, M. SHIMA, K. SAYAMA, H. TARUI, H. NISHIWAKI, and S. TSUDA, in *Amorphous Silicon Technology—1994*, edited by E. A. SCHIFF, M. HACK, A. MADAN, M. POWELL, and A. MATSUDA (Materials Research Society, Pittsburgh, 1994), Vol. 336, p. 487.
- [59] J. PERRIN and B. ALLAIN, *J. Non-Cryst. Solids* **97&98**, 261 (1987).
- [60] A. MATSUDA and G. GANGULY, *Appl. Phys. Lett.* **67**, 1274 (1995).
- [61] A. MIDDYA and S. RAY, *J. Appl. Phys.* **75**, 7340 (1994).

- [62] J. YANG, A. BANERJEE, and S. GUHA, *Appl. Phys. Lett.* **70**, 2975 (1997).
- [63] M. ZEMAN, J. RATH, and R. SCHROPP, NOVEM Report, Project 146.120-024.1 (2002).
- [64] S. GUHA, J. PAYSON, S. AGARWAL, and S. OVSHINSKY, *J. Non-Cryst. Solids* **97&98**, 1455 (1987).
- [65] D. LUNDSZEIN, J. FÖLSCH, F. FINGER, and S. WAGNER, in *14th European PV. Solar Energy Conf.* (Conference Proceedings, Barcelona, 1997), p. 578.
- [66] I. SAKATA, S. OKAZAKI, M. YAMANAKA, and Y. HAYASHI, *Jpn. J. Appl. Phys.* **24**, L428 (1985).
- [67] J. DOYLE, D. DOUGHTY, and A. GALLAGHER, *J. Appl. Phys.* **69**, 4169 (1991).
- [68] A. BIEBERICHER, *Deposition techniques of hydrogenated amorphous silicon using modulated radio-frequency plasmas*, Ph.D. thesis, Utrecht University, The Netherlands, 2002.
- [69] A. MAHAN, J. YANG, S. GUHA, and W. D.L., *Phys. Rev. B* **61**, 1677 (2000).
- [70] M. SHIMA, M. ISOMURA, E. MARUYAMA, S. OKAMOTO, H. HAKU, K. WAKISAKA, S. KIYAMA, and S. TSUDA, in *Amorphous and Microcrystalline Silicon Technology—1998*, edited by R. SCHROPP, H. M. BRANZ, M. HACK, I. SHIMIZU, and S. WAGNER (Materials Research Society, Warrendale, 1998), Vol. 507, p. 145.
- [71] J. RATH, F. TICHELAAR, and R. SCHROPP, *Sol. Energy Mater. & Sol. Cells* **74**, 553 (2002).
- [72] D. SHEN, J. KOLODZEY, D. SLOBODIN, J. CONDE, C. LANE, I. CAMPBELL, P. FAUCHET, and S. WAGNER, in *Amorphous and Heterogeneous Silicon-Based Films—1986* (Materials Research Society, Warrendale, 1986), Vol. 70, p. 301.
- [73] X. XU, J. YANG, and S. GUHA, *Appl. Phys. Lett.* **62**, 1399 (1993).
- [74] M. SHIMA, A. TERAKAWA, M. ISOMURA, H. HAKU, M. TANAKA, K. WAKISAKA, S. KIYAMA, and S. TSUDA, *J. Non-Cryst. Solids* **227-230**, 442 (1998).
- [75] J. RATH, A. MIDDYA, and S. RAY, *Phil. Mag. B* **11**, 821 (1995).
- [76] M. STUTZMANN, *Phil. Mag. B* **60**, 531 (1989).
- [77] S. MIYAZAKI, H. TAKAHASHI, H. YAMASHITA, M. NARASAKI, and M. HIROSE, *J. Non-Cryst. Solids* **299-302**, 148 (2002).
- [78] V. DALAL, *Solid State & Materials Science* In press (2002).
- [79] S. GUHA, J. YANG, A. PAWLIKIEWICZ, T. GLATFELTER, R. ROSS, and S. OVSHINSKY, *Appl. Phys. Lett.* **54**, 2330 (1986).

- [80] J. ZIMMER, H. STIEBIG, and H. WAGNER, in *16th European PV. Solar Ener. Conf.* (Conference Proceedings, Glasgow, 2000), p. 381.
- [81] J. ZIMMER, H. STIEBIG, and H. WAGNER, *J. Appl. Phys.* **84**, 611 (1998).
- [82] M. J. POWELL and S. C. DEANE, *Phys. Rev. B* **48**, 10815 (1993).
- [83] M. J. POWELL and S. C. DEANE, *Phys. Rev. B* **53**, 10121 (1996).
- [84] P. MCELHENY, J. ARCH, H. LIN, and S. FONASH, *J. Appl. Phys.* **67**, 3803 (1990).
- [85] J. ARCH, F. RUBINELLI, J. HOU, and S. FONASH, *J. Appl. Phys.* **69**, 7057 (1991).
- [86] H. OKAMOTO, H. KIDA, and Y. HAMAKAWA, *Phil. Mag. B* **49**, 231 (1984).
- [87] F. RUBINELLI, J. OUWENS, and R. SCHROPP, in *13th European PV. Solar Ener. Conf.* (Conference Proceedings, Nice, France, 1995), p. 19.
- [88] S. SMITH, Z.E. AND WAGNER, *Phys. Rev. Lett.* **59**, 688 (1987).
- [89] X. XU, A. BANERJEE, J. YANG, and S. GUHA, in *Amorphous and Heterogeneous Silicon-Based Films—1995*, edited by M. P. A. M. M HACK, E.A. SCHIFF and A. MADAN (Materials Research Society, Warrendale, 1995), Vol. 377, p. 651.
- [90] K. VASANTH, A. PAYNE, B. CRONE, S. SHERMAN, M. JAKUBOWSKI, and S. WAGNER, in *Amorphous and Heterogeneous Silicon-Based Films—1995*, edited by M. P. A. M. M HACK, E.A. SCHIFF and A. MADAN (Materials Research Society, Warrendale, 1995), Vol. 377, p. 663.
- [91] F. SMOLE, M. TOPIČ, and FURLAN, in *14th European PV. Solar Energy Conf.* (Conference Proceedings, Barcelona, 1997), p. 632.
- [92] M. STUTZMANN, R. STREET, C. TSAI, J. BOYCE, and S. READY, *J. Appl. Phys.* **66**, 569 (1989).
- [93] S. ALJISHI, Z. SMITH, D. SLOBODIN, J. KOLODZEY, V. CHU, R. SCHWARZ, and S. WANER, in *Amorphous and Heterogeneous Silicon-Based Films—1986* (Materials Research Society, Warrendale, 1986), Vol. 70, p. 269.
- [94] H. STIEBIG, F. SIEBKE, R. CARIUS, and J. KLOMFAB, in *Amorphous and Microcrystalline Silicon Technology—1998*, edited by R. SCHROPP, H. M. BRANZ, M. HACK, I. SHIMIZU, and S. WAGNER (Materials Research Society, Warrendale, 1998), Vol. 507, p. 403.
- [95] J. COHEN, NREL Technical Report, NREL/SR-520-32535 (2000).
- [96] J. CHEVALIER, H. WIEDER, A. ONTON, and GUARNIERI, *Solid State Comm.* **24**, 867 (1977).
- [97] S. ALJISHI, V. CHU, Z. SMITH, and J. CONDE, *J. Non-Cryst. Solids* **97&98**, 1023 (1987).

- [98] G. MUNYEME, *Experimental and computer modeling studies of metastability of amorphous silicon based solar cells*, Ph.D. thesis, Utrecht University, The Netherlands, 2003.
- [99] S. GUHA, J. YANG, A. PAWLIKIEWICZ, G. T., R. ROSS, and S. OVSHINSKY, In: Proc. of 20<sup>th</sup> IEEE Photovolt. Spec. Conf., Las Vegas, NV 79 (1988).
- [100] F. RUBINELLI, R. JIMENEZ ZAMBRANO, J. RATH, and R. SCHROPP, J. Appl. Phys. **91**, 2409 (2002).
- [101] R. JIMENEZ ZAMBRANO, F. RUBINELLI, J. RATH, and R. SCHROPP, J. Non-Cryst. Solids **299-302**, 1131 (2002).
- [102] D. LUNDSZEIN, F. FINGER, and S. WAGNER, in *17th European PV. Solar Energy Conf.* (Conference Proceedings, Munich, 2001), p. 2854.
- [103] I. KOBAYASHI, T. OGAWA, and S. HOTTA, Jpn. J. Appl. Phys. **31**, 336 (1991).
- [104] H. DERSCH, J. STUKE, and J. BEICHLER, Appl. Phys. Lett. **38**, 456 (1980).
- [105] I. HIRABAYASHI, K. MORIGAK, and S. NITTA, Jpn. J. Appl. Phys. **19**, L357 (1980).
- [106] D. STAEBLER and C. WRONSKI, J. Appl. Phys. **51**, 3262 (1980).
- [107] S. SHIMIZU, T. TABUCHI, K. HATTORI, H. KIDA, and H. OKAMOTO, in *Amorphous and Microcrystalline Silicon Technology—1998*, edited by R. SCHROPP, H. M. BRANZ, M. HACK, I. SHIMIZU, and S. WAGNER (Materials Research Society, Warrendale, 1998), Vol. 507, p. 735.
- [108] P. STRADINS, S. SHIMIZU, M. KONDO, and A. MATUDA, in *Amorphous and Heterogeneous Silicon-Based Films—2001*, edited by J. B. JOYCE, J. D. COHEN, R. W. COLLINS, J.-I. HANNA, and M. STUTZMANN (Materials Research Society, Warrendale, 2001), Vol. 664, p. A12.6.
- [109] D. HAN and H. FRITZSCHE, J. Non-Cryst. Solids **59&60**, 397 (1983).
- [110] K. SHEPARD, Z. SMITH, S. ALJISHI, and S. WAGNER, in *Amorphous Silicon Technology*, edited by M. J. MADAN, A. THOMSON, P. C. TAYLOR, P. G. LECOMBER, and Y. HAMAKAWA (Materials Research Society, Pittsburgh, 1988), Vol. 118, p. 147.
- [111] T. KAMEI, N. HATA, A. MATSUDA, T. UCHIYAMA, S. AMANO, K. TSUKAMOTO, Y. YOSHIOKA, and T. HIRAO, Appl. Phys. Lett. **68**, 2380 (1996).
- [112] D. ADLER, Sol. Cells **9**, 133 (1983).
- [113] M. STUTZMANN, in *Amorphous and Microcrystalline Silicon Technology—1997*, edited by S. WAGNER, M. HACK, E. A. SCHIFF,

- R. SCHROPP, and I. SHIMIZU (Materials Research Society, Pittsburgh, 1997), Vol. 467, p. 37.
- [114] M. STUTZMANN, W. B. JACKSON, and C. C. TSAI, *Phys. Rev. B* **32**, 23 (1985).
- [115] M. STUTZMANN and C. NEBEL, *Encycl. of Appl. Phys. (VCH Publ.)* **18**, 151 (1997).
- [116] H. GLESKOVA, P. MORIN, and S. WAGNER, in *Amorphous Insulating Films*, edited by J. KANICKI, W. L. WARREN, R. A. B. DEVINE, and M. MATSUMURA (Materials Research Society, Warrendale, 1993), Vol. 297, p. 589.
- [117] P. STRADINS and H. FRITZSCHE, *Phil. Mag. B* **69**, 121 (1994).
- [118] P. SANTOS, N. JOHNSON, and R. STREET, *Phys. Rev. Lett.* **67**, 2686 (1991).
- [119] H. BRANZ, S. ASHER, H. GLESKOVA, and S. WAGNER, *Phys. Rev. B* **59**, 5513 (1999).
- [120] H. BRANZ, *Sol. Energy Mater. & Sol. Cells* **78**, 425 (2003).
- [121] K. PALINGINIS, J. YANG, S. GUHA, and J. COHEN, in *Amorphous and Heterogeneous Silicon Thin Films—2000*, edited by R. W. COLLINS, H. M. BRANZ, M. STUTZMANN, S. GUHA, and H. OKAMOTO (Materials Research Society, Warrendale, 2000), Vol. 609, p. A3.3.
- [122] D. REDFIELD, *Appl. Phys. Lett.* **52**, 492 (1988).
- [123] D. REDFIELD, *Appl. Phys. Lett.* **54**, 398 (1989).
- [124] J. KAKALIOS, R. A. STREET, and W. JACKSON, *Phys. Rev. B* **59**, 1037 (1987).
- [125] M. FATHALLAH, *Phil. Mag. B* **61**, 403 (1990).
- [126] S. HECK and H. BRANZ, *Appl. Phys. Lett.* **79**, 3080 (2001).
- [127] J. PEARCE, X. NIU, R. KOVAL, G. GANGULY, D. CARLSON, R. COLLINS, and C. WRONSKI, in *Amorphous and Heterogeneous Silicon-Based Films—2001*, edited by J. B. JOYCE, J. D. COHEN, R. W. COLLINS, J.-I. HANNA, and M. STUTZMANN (Materials Research Society, Warrendale, 2001), Vol. 664, p. A12.3.
- [128] H. FRITZSCHE, *Solid State Comm.* **94**, 397 (1995).
- [129] N. HATA, T. KAMEI, H. OKAMOTO, and A. MATSUDA, in *Amorphous and Microcrystalline Silicon Technology—1997*, edited by S. WAGNER, M. HACK, E. A. SCHIFF, R. SCHROPP, and I. SHIMIZU (Materials Research Society, Pittsburgh, 1997), Vol. 467, p. 61.
- [130] T. KAMEI, P. STRADINS, and A. MATSURA, *Appl. Phys. Lett.* **74**, 1707 (1999).

- [131] P. ROCA I CABARROCAS, in *Amorphous and Microcrystalline Silicon Technology—1998*, edited by R. SCHROPP, H. M. BRANZ, M. HACK, I. SHIMIZU, and S. WAGNER (Materials Research Society, Warrendale, 1998), Vol. 507, p. 855.
- [132] B. NELSON, E. IWANICZKO, A. MAHAN, Q. WANG, Y. XU, R. CRANDALL, and H. BRANZ, *Thin Solid Films* **395**, 292 (2001).
- [133] M. BARRANCO I DÍAZ, J. KLEIDER, P. ST'ACHEL, P. SLADEK, and P. ROCA I CABARROCAS, in *14th European PV. Solar Energy Conf.* (Conference Proceedings, Barcelona, 1997), p. 609.
- [134] S. SUGIYAMA, J. YANG, and S. GUHA, *Appl. Phys. Lett.* **70**, 378 (1997).
- [135] G. GANGULY, S. YAMASAKI, and A. MATSUDA, *Phil. Mag. B* **63**, 281 (1991).
- [136] D. HAN, J. BAUGH, and G. YUE, *Phys. Rev. B* **62**, 7169 (2000).
- [137] G. NAKAMURA, K. SATO, and Y. YUKIMOTO, *Sol. Cells* **9**, 75 (1983).
- [138] A. TERAKAWA, M. ISOMURA, and S. TSUDA, *Jpn. J. Appl. Phys.* **35**, 5612 (1996).
- [139] F. ZHONG, C. CHEN, and J. COHEN, *J. Non-Cryst. Solids* **198-200**, 572 (1996).
- [140] T. UNOLD, J. COHEN, and C. FORTMANN, *J. Non-Cryst. Solids* **137&138**, 809 (1991).
- [141] J. COHEN, J. HEATH, K. PALINGINIS, J. YANG, and S. GUHA, *J. Non-Cryst. Solids* **299-302**, 449 (2002).
- [142] M. STUTZMANN, W. JACKSON, and TSAI.C.C., *Appl. Phys. Lett.* **45**, 1075 (1984).
- [143] K. PALINGINIS, J. COHEN, J. YANG, and S. GUHA, *J. Non-Cryst. Solids* **266-269**, 665 (2000).
- [144] A. TERAKAWA, M. SHIMA, H. TARUI, H. NISHIWAKI, and S. TSUDA, *Jpn. J. Appl. Phys.* **34**, 1741 (1995).
- [145] J. COHEN, J. HEATH, K. PALINGINIS, J. YANG, and S. GUHA, in *Amorphous and Heterogeneous Silicon-Based Films—2001*, edited by J. B. JOYCE, J. D. COHEN, R. W. COLLINS, J.-I. HANNA, and M. STUTZMANN (Materials Research Society, Warrendale, 2001), Vol. 664, p. A12.5.
- [146] K. VASANTH, M. NAKATAKA, S. WAGNER, and M. BENNETT, in *Amorphous Insulating Films*, edited by J. KANICKI, W. L. WARREN, R. A. B. DEVINE, and M. MATSUMURA (Materials Research Society, Warrendale, 1993), Vol. 297, p. 827.
- [147] D. CARLSON, L. CHEN, G. GANGULY, G. LIN, A. MIDDYA, R. CRANDALL, and R. REEDY, in *Amorphous and Heterogeneous Silicon Thin Films: Fundamentals to Devices—1999*, edited by H. M. BRANZ, R. W.

- COLLINS, H. OKAMOTO, S. GUHA, and R. SCHROPP (Materials Research Society, Warrendale, 1999), Vol. 557, p. 395.
- [148] J. FÖLSCH, D. LUNDSZEIN, F. FINGER, H. STIEBIG, J. ZIMMER, C. BENEKING, H. WIEDER, and S. WAGNER, in *14th European PV. Solar Energy Conf.* (Conference Proceedings, Barcelona, 1997), p. 601.
- [149] M. BENNETT, A. CATALANO, K. RAJAN, and R. ARYA, 21<sup>st</sup> IEEE Photovoltaic Specialists Conference 1653 (1990).
- [150] A. MAHAN, P. RABOISSON, P. MENNA, A. MASCARENHAS, and R. TSU, *Sol. Cells* **24**, 195 (1988).
- [151] S. JONES, Y. CHEN, and D. WILLIAMSON, *Appl. Phys. Lett.* **62**, 3267 (1993).
- [152] A. TERAKAWA, M. MATSUNAMI, S. KIYAMA, and S. TSUDA, *J. Appl. Phys.* **84**, 4611 (1998).
- [153] K. SAYAMA, A. TERAKAWA, M. SHIMA, E. MARUYAMA, K. NINOMIYA, H. TARUI, S. TSUDA, and S. NAKANO, in *Amorphous Silicon Technology—1994*, edited by E. A. SCHIFF, M. HACK, A. MADAN, M. POWELL, and A. MATSUDA (Materials Research Society, Pittsburgh, 1994), Vol. 336, p. 423.
- [154] Y. LUBIANIKER, J. COHEN, H. JIN, and J. ABELSON, in *Amorphous and Microcrystalline Silicon Technology—1998*, edited by R. SCHROPP, H. M. BRANZ, M. HACK, I. SHIMIZU, and S. WAGNER (Materials Research Society, Warrendale, 1998), Vol. 507, p. 729.
- [155] J. YANG and S. GUHA, in *Amorphous and Heterogeneous Silicon Thin Films: Fundamentals to Devices—1999*, edited by H. M. BRANZ, R. W. COLLINS, H. OKAMOTO, S. GUHA, and R. SCHROPP (Materials Research Society, Warrendale, 1999), Vol. 557, p. 239.
- [156] P. MANDRACCI, M. RASTELLO, P. RAVA, F. GUILLIANI, and F. GIORGIS, *Thin Solid Films* **337**, 232 (1999).
- [157] P. ROCA I CABARROCA, P. ST'ACHEL, H. HAMMA, and Y. POISSANT, in *2nd World Conf. and Exhib. PV Solar Energ. Conversion* (Conf. Proceedings, Vienna, 1998), p. 355.
- [158] C. LONGEAUD, J. KLEIDER, M. GAUTHOER, R. KAPLAN, R. BUTTÉ, R. MEAUDRE, and P. ROCA I CABARROCA, in *2nd World Conf. and Exhib. PV Solar Energ. Conversion* (Conf. Proceedings, Vienna, 1998), p. 680.
- [159] M. BENNETT and K. RAJAN, *J. Appl. Phys.* **67**, 4161 (1990).
- [160] J. YANG and S. GUHA, *Appl. Phys. Lett.* **61**, 2917 (1992).



## Summary

---

Amorphous silicon technology for photovoltaic applications is finding a way to overcome the principal limitation: electronic metastability under illumination, known as the Staebler-Wronski effect. The major developments to avoid degradation have been the use of multijunction solar cells and the dilution of the source gasses with hydrogen during the growth of amorphous silicon. Multijunction structures are formed by stacking several solar cells on the top of each other. Each of them absorbs a broad band of the solar spectrum. A special case of multijunction is the tandem structure, consisting of two stacked solar cells. From the different possible *a*-Si:H related materials suitable for this structure (*a*-Si:H, *a*-SiC:H, *a*-SiGe:H,  $\mu c$ -Si:H,  $\mu c$ -SiGe:H ...) this research is centered on p-i-n tandem structures with *a*-Si:H and *a*-SiGe:H material, for the top and the bottom solar cell, respectively. In particular, the influence of the deposition conditions of *a*-SiGe:H deposited by plasma enhanced chemical vapour deposition (PECVD) on the electrical and optical characteristics of the solar cell as well as on the stability are studied. This includes investigation of the band gap profile of the intrinsic layer of the solar cell.

The thesis is divided into five chapters. The first two chapters give a brief introduction to the *a*-Si:H material and to the experimental techniques used during the research. Chapter 3 deals with the improvement of the material characteristics through the study of the deposition conditions. In Chapter 4, the material in a solar cell structure is described by a computer model, which is applied to develop higher efficiency solar cells. Finally, in Chapter 5 the improvements obtained in the previous two chapters are applied to solar cells devices in order to study their stability. A summary of the chapters is presented in more detail below.

Depositing at the onset of crystalline formation, the material exhibits very high stability against light exposure. To control the crystallization process, the influence of the deposition temperature ( $T_s$ ) and  $H_2$  dilution on the formation of a microcrystalline phase in *a*-SiGe:H material is studied in Chapter 3. The  $H_2$  dilution is varied along with the  $T_s$  to promote the formation of microcrystalline phase at low deposition temperature, with the aim of depositing *a*-SiGe:H at the edge of this transition. The material obtained exhibits a reduction in the amount of Ge-Ge clustering to values lower than amorphous material, promoting the growth of more ordered material. We speculate that the improvement of the medium range order (confirmed by a selected-area diffraction pattern) is generated by het-

erogeneous microstructures of Si and Ge atoms with a more ordered amorphous structure than the heterogeneous *a*-SiGe:H network in which they are immersed. At the same time, conditions for higher deposition rate are investigated. Replacing SiH<sub>4</sub> with Si<sub>2</sub>H<sub>6</sub> as a feed gas, the deposition rate is doubled. The different radical formation in the plasma leads to an amorphous material with higher H content, without the presence of crystalline formation. We conclude that the deposition of protocrystalline *a*-SiGe:H is possible at low temperatures down to a certain minimum substrate temperature (170 °C). At the same time, higher deposition rate conditions obtained with Si<sub>2</sub>H<sub>6</sub> are incompatible with the growth of protocrystalline *a*-SiGe:H at low substrate temperature (in the range studied between 170 and 220 °C).

The difference in band gap between the *a*-SiGe:H material used for the intrinsic layer (i) and the doped *a*-Si:H materials (p and n) in a solar cell structure produces recombination losses at the interfaces (p/i and i/n), which deteriorates the output of the solar cell. To reduce the offset in band gap, several layers of intermediate band gap material must be deposited at the p/i and the i/n interface. The property of the *a*-SiGe:H material by which the band gap can be modified through the Ge concentration, allows having a close control in designing the band gap profile in between the doped layers. To help designing of the band gap profile, we have made use of a computer model of the *a*-SiGe:H material in a solar cell structure (D-AMPS). In Chapter 4, the annealed state of a single junction *a*-SiGe:H p-i-n solar cell is studied by computer simulation. Two models describing the density of defect states in the band gap are compared: the uniform density of states model and the defect pool model. Both are able to simulate the output characteristics of the solar cell. In Chapter 4 was described how the uniform density of state model is not able to justify improvements experimentally observed when the band gap is modified. On the other hand, the defect pool model showed agreement with the experimental observations.

Implementing the defect pool model, the influence of the band gap profile on the final characteristics of *a*-SiGe:H solar cells is studied. As a result, a new shape profile is found which increases the efficiency and the open circuit voltage without losses in photogenerated current. Experimental results following the direction observed in computer simulation are presented.

In Chapter 5, the incorporation of *a*-SiGe:H material in single junction and tandem solar cell structures is presented. A study of the stability against light-soaking of *a*-SiGe:H as a material and in different device configurations is carried out. The degradation experiments show how fully amorphous silicon germanium material (500 nm) suffers from degradation in photo-conductivity. This fully amorphous material is obtained by using Si<sub>2</sub>H<sub>6</sub> or at amorphous depositing condi-

tion (low deposition temperature and low hydrogen dilution). On the other hand, *a*-SiGe:H material (500 nm) with a mix of phases is stable during light exposure. Thinner film has no appreciable crystalline modes in the Raman spectrum, but exhibits an improvement in the medium range order (as discussed in Chapter 3). It is this thin protocrystalline film which is used in the solar cell structure. Comparing the degradation in several solar cells with this material against solar cell with *a*-Si:H and fully amorphous silicon germanium, it is demonstrated that *a*-SiGe:H at the edge of microcrystallinity behaves stable during the 1000 hours of the experiments. Moreover, implemented in a tandem solar cell it is shown through spectral response measurements that the top cell is responsible for the degradation in the tandem solar cell, while the bottom cell remains stable. As a conclusion, the stability of *a*-SiGe:H at the onset of microcrystalline formation is demonstrated for *a*-SiGe:H materials. At the same time, the advantage of higher deposition rates obtained by replacing SiH<sub>4</sub> with Si<sub>2</sub>H<sub>6</sub> has the drawback of suffering from instability.



## Samenvatting

---

Ten behoeve van de amorf silicium (*a*-Si:H) technologie voor fotovoltaïsche toepassingen is het essentieel dat de grootste beperking wordt overwonnen: de elektronische metastabiliteit onder belichting, ook wel bekend als het Staebler-Wronski effect. De belangrijkste technologische ontwikkelingen om de degradatie van het materiaal tegen te gaan, zijn de toepassing van gestapelde zonnecellen en het gebruik van waterstof om het gasmengsel gebruikt bij de plasma depositie van amorf silicon te verdunnen. Gestapelde structuren worden gevormd door een aantal zonnecellen op elkaar te deponeren. Elke cel kan zo een brede spectrale band van het zonlicht absorberen. Een speciaal geval van een gestapelde zonnecel is de tandem structuur. Deze bestaat uit twee zonnecel-lagen. Van de verschillende *a*-Si:H gerelateerde materialen die geschikt zijn voor deze structuur, worden *a*-Si:H en *a*-SiGe:H in dit proefschrift behandeld als respectievelijk de bovenste en de onderste zonnecel van een p-i-n tandem structuur. In het bijzonder wordt de invloed van de depositie parameters voor de plasma geïnduceerde chemische damp depositie (PECVD) van *a*-SiGe:H op de elektrische en optische eigenschappen van de zonnecel bestudeerd, met speciale aandacht voor de elektronische stabiliteit onder belichting. Er is eveneens onderzoek gedaan naar de optimale gradering van de band afstand in de groeirichting van de intrinsieke laag van de zonnecel.

Het proefschrift is verdeeld in 5 hoofdstukken. De eerste twee geven een korte inleiding over het *a*-Si:H materiaal en de experimentele technieken die zijn gebruikt tijdens het onderzoek. Hoofdstuk 3 behandelt de verbetering van de materiaaleigenschappen tijdens de studie naar de depositie condities. In hoofdstuk 4 wordt het materiaal toegepast in een zonnecelstructuur beschreven met een computermodel dat is toegepast om zonnecellen met een hoger rendement te ontwikkelen. In hoofdstuk 5 worden tenslotte de verworven resultaten uit de vorige twee hoofdstukken toegepast op zonnecellen om de stabiliteit te bestuderen. Hieronder volgt een samenvatting van de hoofdstukken in meer detail.

Amorf silicium gedeponerd in een regime nabij de overgang naar  $\mu\text{c-SiH}$ , vertoont een hoge mate van stabiliteit onder belichting. Om het kristallisatieproces te beheersen is de invloed van de depositietemperatuur van het substraat ( $T_s$ ) en van de waterstof ( $\text{H}_2$ ) verdunning op het ontstaan van de microkristallijne fase in het *a*-SiGe:H materiaal bestudeerd in hoofdstuk 3. De  $\text{H}_2$  verdunning en de substraattemperatuur zijn gevarieerd om het ontstaan van de microkristallijne fase te stimuleren op lage depositietemperaturen met als doel *a*-SiGe:H depositie te

verkrijgen onder condities dicht bij de overgang naar de microkristallijne fase. Dit materiaal noemen we protocristalline silicium. Het verkregen materiaal laat een vermindering zien van het aantal Ge-Ge clusters ten opzichte van het amorf materiaal. Dit leidt tot een meer geordend materiaal. We speculeren dat de verbetering van de ordening over middenlange afstand (bevestigd door SADP) wordt bewerkstelligd door heterogene microstructuren van Si en Ge atomen met meer geordende amorphe structuren dan het heterogene *a*-SiGe:H netwerk waarin ze zijn geïncorporeerd. De condities voor een hogere depositiesnelheid zijn eveneens onderzocht. Door SiH<sub>4</sub> te vervangen door Si<sub>2</sub>H<sub>6</sub> als procesgas, werd de depositiegroeisnelheid verdubbeld. Het verschil in het ontstaan van radicalen in het plasma, resulteert in een amorf materiaal met een hoger H gehalte, zonder dat er een kristallijne fase in het materiaal ontstaat. We concluderen dat boven een minimale substraattemperatuur de depositie van protokristallijn *a*-SiGe:H mogelijk is op lage temperaturen. De condities voor een hogere depositiesnelheid met Si<sub>2</sub>H<sub>6</sub> zijn echter onverenigbaar met de groei van protocristalline *a*-SiGe:H bij een lagere substraattemperatuur.

Het verschil in band afstand voor het *a*-SiGe:H materiaal dat is gebruikt voor de intrinsieke laag (i) en de gedoteerde *a*-Si:H materialen (p en n) in een zonnecelstructuur zorgt voor verliezen in recombinatie in de grensvlakken tussen de intrinsieke en de gedoteerde lagen (p/i en i/n interface), hetgeen de output van de zonnecel verslechtert. Om het verschil in band afstand te verminderen, worden meerdere lagen materiaal met tussenliggende band afstanden geplaatst bij de p/i en de i/n raakvlakken. *a*-SiGe heeft de eigenschap dat de band afstand gewijzigd kan worden door de Ge concentratie aan te passen. Dit zorgt ervoor dat we een exacte controle hebben over het ontwerp van het profiel van de band afstand tussen de intrinsieke en gedoteerde lagen. Om het ontwerpen van dit profiel te vergemakkelijken, hebben we gebruik gemaakt van een computermodel van het *a*-SiGe:H materiaal in een zonnecelstructuur (D-AMPS). In hoofdstuk 4 wordt de afkoelende staat van een enkelvoudige *a*-SiGe:H p-i-n zonnecel bestudeerd met een computersimulatie. Er worden twee modellen vergeleken die de defect dichtheid binnen de band afstand beschrijven: het 'uniforme toestandsdichtheid model' en het zogenaamde 'defect pool model' (DBP). Met allebei de modellen is het mogelijk om de karakteristieken van de output van de zonnecellen te simuleren. In het hoofdstuk is beschreven hoe het 'uniforme toestandsdichtheid model' niet in staat is om verbeteringen die gezien zijn tijdens de experimenten te simuleren wanneer de band afstand is aangepast. Anderzijds is het 'defect pool model' in overeenstemming met de experimentele resultaten.

Toen we het DPM implementeerden, is de invloed van het band afstand-profiel op de output van de *a*-SiGe:H zonnecel bestudeerd. Als resultaat hier-

van is een profiel met een nieuwe vorm gevonden die de efficiëntie en de openklemspanning verhoogt, zonder verlies van fotogegeneerde stroom. De resultaten van de experimenten, die dezelfde trend vertonen als de computersimulaties, zijn weergegeven.

In hoofdstuk 5 wordt de toepassing van *a*-SiGe:H materiaal in enkelvoudige en tandem structuur gepresenteerd. Er is een studie gedaan naar de stabiliteit onder belichting van *a*-SiGe:H als materiaal vergeleken met *a*-SiGe:H in verschillende zonnecel configuraties. De degradatie-experimenten laten zien hoe een volledig amorf *a*-SiGe:H materiaal (500 nm) lijdt aan degradatie in fotogeleiding. Dit 100 % amorse materiaal is verkregen met Si<sub>2</sub>H<sub>6</sub> onder amorse depositiecondities (lage depositietemperaturen en lage waterstof verdunning). Anderzijds, is *a*-SiGe:H materiaal (500 nm) met een mengsel van een amorf en kristallijn fase stabiel onder blootstelling aan licht. Een dünnere film heeft geen meetbare kristallijne bijdrage in het Raman spectrum, maar laat een verbetering zien in de ordening over middenlange afstand (zoals besproken in hoofdstuk 3). Deze dunne protokristallijne film is gebruikt als intrinsieke laag in een zonnecelstructuur. Als we het gedrag onder lichtdegradatie van verschillende zonnecellen van dit materiaal vergelijken met zonnecellen van *a*-Si:H en volledig amorf *a*-SiGe:H dan blijkt dat *a*-SiGe:H op de grens van het microkristallijne depositieregime zich stabiel gedraagt gedurende 1000 uur lichtdegradatie. Bovendien is er door middel van spectrale respons metingen laten zien dat de bovenste zonnecel van een tandem structuur verantwoordelijk is voor de degradatie, terwijl de onderste zonnecel stabiel blijft. Als conclusie kunnen we zeggen dat het verband tussen de stabiliteit onder belichting van *a*-SiGe:H materialen en de overgang van het ontstaan van amorf naar microkristallijn is aangetoond. Het voordeel van hogere groeisnelheden verworven door SiH<sub>4</sub> te vervangen door Si<sub>2</sub>H<sub>6</sub> heeft echter het nadeel dat het verkregen materiaal niet stabiel is onder belichting.



## List of publications

---

### Publications related to this thesis

R. Jiménez Zambrano, F.A. Rubinelli, W.M. Arnoldbik, J.K. Rath and R.E.I. Shopp, *Computer-aided band gap engineering and experimental verification of amorphous silicon-germanium solar cells*, accepted for publication in *Solar Energy Materials and Solar Cells* (2003).

R. Jiménez Zambrano, F.A. Rubinelli, W.M. Arnoldbik, J.K. Rath and R.E.I. Schropp, *Modelling of the band gap profile in the intrinsic layer of the a-SiGe:H material: application in solar cells*, in: J.R. Abelson, J.B. Boyce, J.D. Cohen, H. Matsumura and J. Robertson (Eds.), *Amorphous and Heterogeneous Silicon-Based Films - 2002*, San Francisco, USA, April 1-5, 2002, *Materials Research Society Symposium Proceedings* **715**, p. A.6.9 (2002).

A. Gordijn, R. Jiménez Zambrano, J.K. Rath and R.E.I. Schropp, *Highly stable hydrogenated amorphous silicon germanium solar cells*, *IEEE Transactions on Electron Devices*, **49**, 949 (2002).

R. Jiménez Zambrano, F.A. Rubinelli, J.K. Rath and R.E.I. Schropp, *Improvement in the spectral response at long wavelength of a-SiGe:H solar cells by exponential band gap design of thin i-layer*, *Journal of Non-Crystalline Solids* **229-302**, 1131 (2002).

F.A. Rubinelli, R. Jiménez Zambrano, J.K. Rath and R.E.I. Schropp, *Using computer modelling analysis in single junction a-SiGe:H p-i-n solar cells*, *Journal of Applied Physics*, **91**, 2409 (2002).

### Other publications

J.K. Rath, A.C.W. Biebericher, R. Jiménez Zambrano, R.E.I. Schropp, W.F. van der Weg and W.J. Goedheer, *Hydrogenated amorphous silicon with high growth rate, gas utilisation, and homogeneous deposition by amplitude modulated VHF-PECVD for solar cell application*, in: J.R. Abelson, J.B. Boyce, J.D. Cohen, H. Matsumura and J. Robertson (Eds.), *Amorphous and Heterogeneous Silicon-Based Films - 2002*, San Francisco, USA, April 1-5, 2002, *Materials Research Society Symposium Proceedings* **715**, p. A6.6 (2002).

R.E.I. Schropp, C.H.M. van der Werf, M.K. van Veen, P.A.T.T. van Veenendaal, R. Jiménez Zambrano, Z. Hartman, J. Löffler and J.K. Rath, *Thin film a-Si/poly-Si multibandgap tandem solar cells with both absorber layers deposited by hot wire CVD*, in: M. Stutzmann, J.B. Boyce, J.D. Cohen, R.W. Collins and J. Hanna (Eds.), *Amorphous and Heterogeneous Silicon-Based Films - 2001*, San Francisco, USA, April 16-20, 2001, Materials Research Society Symposium Proceedings **664**, p. A15.6 (2001).

## Acknowledgements

---

I would not like to let this opportunity slip without publicly show my gratitude to those who have contributed in one or another way to my work during the last four years. I would like to thank Prof. Dr. Ruud E.I. Schropp for the opportunity he has offered me to join his dynamic group. His advices and discussions have been clarifying throughout this work. Dr. Jatindra K. Rath has opened me the doors to the a-SiGe:H world. I would like to thank him for the opportunity I have had of sharing his wide expertise in many productive discussions.

I would like to thank Prof. Dr. Frans Habraken, Prof. Dr. Jaap Dijkhuis and Prof. Dr. Daniël Vanmaekelbergh from the Debye Institute and Dr. Miro Zeman from the Delft University for their critical reading of the manuscript.

The first contact with the photovoltaic field came from the hand of Dr. Julio Cárabe and Dr. Javier J. Gandía from the CIEMAT. Their guide and animated talks have shown me many other ways of looking to the science. Thanks to both of you.

During this time, many people has come and gone. Two of them have left something behind. Thank you Pancho amigo, for your friendship. I have really enjoyed your talks during the Dutch summer. And of course, my gratitude to Dr. Francisco Rubinelli for the discussions at work and the help with D-AMPS. Dr. Geoffrey Munyeme. These years in Holland would not have been the same without your friendship. And the DPM would still be a mystery.

Looking back to my arrival in Holland, I would like to thank Aad Gordijn, who has introduced me to the Dutch culture in my first days and his talks at 2 o'clock were a nice alternative to the siesta. To Alberto Palmero Acebedo. He has done his best for keeping me awake when more I needed it with his gazpacho. My acknowledge to Hanno Goldbach, Alexander Germeau, Jochen Löffler, Bernd Stannowski, Marieke van Veen for their consultations. I thank Karine van der Werf for making many and different wishes come true. Wim Arnold Bik has offered me valuable RBS measurements. Ruurd Lof for having always time. Paula Bronsveld for her magic finger with the CPM. Riny de Haas for her assistance. Jense Meek and Djaja Ottenhof for their work with Si<sub>2</sub>H<sub>6</sub>.

To the friends for being there in spite of the distance. Among them I have to congratulate the juggler of the Princesa hotel on making disappear the distance; the "good economist" of the Banco de España on his endless willing words and his future destinations where we'll join him; the princess bride on taking us constantly

out, which I enjoy even from here. My parents have given me their continuous support and shared their joy. Thank you.

The page of acknowledgements is always too short. But this one would not be complete unless I thank David, Paula and Tike, and Domien and Anne for being there.

Finally I wish to express deep appreciation to Chawa Verwer, who has shared with me during this time ups and downs, here and there, and now and then. For her joy of living.

## Curriculum vitae

---

The author was born in Madrid. He attended secondary school at Velazquez Institute and completed in 1991. Thereafter, he joined the Autonoma University of Madrid where he studied theoretical physics, specializing in astrophysics. He got the Physic graduate in 1996. He was then admitted to the University of Provence (France) where he completed a D.E.A. in "Radiation And Plasmas" in 1997. The project was done at C.E.A. of Cadache with title "Study of the current decreasing measured by the dripped diagnostic". He joined a master course in nuclear energy at the Centre for Energy, Environmental and Technological Research (CIEMAT) in Madrid. While at the CIEMAT, he had carried out a postgraduate research in semiconductors devices with photovoltaic purpose. He started his Ph.D. research in October 1999 with the Interface Physics Group at the Debye Institute of the University of Utrecht.